NATIONAL ENERGY TECHNOLOGY LABORATORY

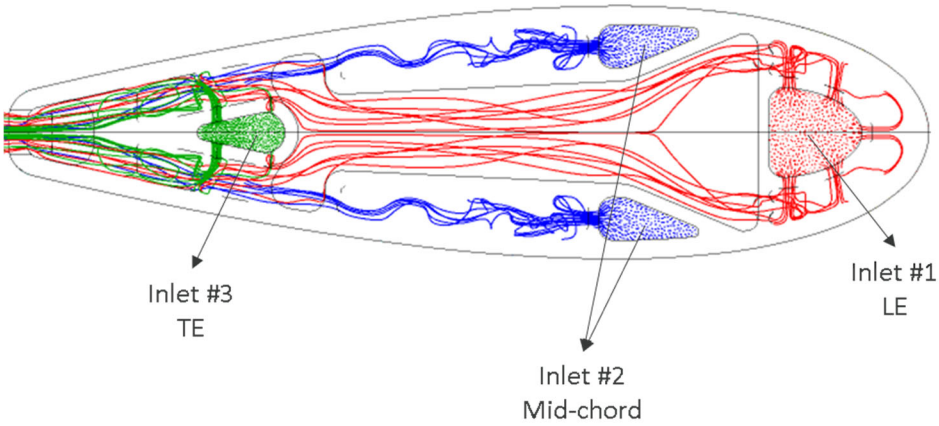

Advanced Airfoil Cooling Schemes to Increase Efficiency in Gas Turbines for Combined Heat and Power Applications

28 October 2022

U.S. DEPARTMENT OF ENERGY | NATIONAL ENERGY TECHNOLOGY LABORATORY

DOE/NETL-2023/3822

Disclaimer

This project was funded by the United States Department of Energy, National Energy Technology Laboratory, in part, through a site support contract.

Cover Illustration: A sectioned view of the NETL double-wall design (the best performing cooling scheme considered) is displayed with streamlines computed by computational fluid dynamics (CFD) shown as an overlay. The airfoil is built as a series of nine modules over the airfoil span. Flow enters through four independent plenums and is distributed to the leading edge (LE, red), mid-chord (blue), and trailing edge (TE, green). The design consumes 42% of the coolant required by the baseline blade to reach the advanced overall efficiency target, and thus enables a 100 °C increase in gas turbine firing temperature.

Suggested Citation: Straub, D.; Searle, M.; Roy, A.; Ramesh, S.; Robey, E.; Floyd, T.; Ames, F. E. *Advanced Airfoil Cooling Schemes to Increase Efficiency in Gas Turbines for Combined Heat and Power Applications*; DOE.NETL-2023/3822; NETL Technical Report Series; U.S. Department of Energy, National Energy Technology Laboratory: Morgantown, WV, 2022; pp 104.

An electronic version of this report can be found at:

https://netl.doe.gov/energy-analysis/search

Advanced Airfoil Cooling Schemes to Increase Efficiency in Gas Turbines for Combined Heat and Power Applications

Douglas Straub[1], Matthew Searle[1,2], Arnab Roy[1,2], Sridharan Ramesh[1,2], Edward Robey[1,2], Tim Floyd[1,2], Forrest E. Ames[3]

[1] National Energy Technology Laboratory, 3610 Collins Ferry Road, Morgantown, WV 26505, USA

[2] NETL Support Contractor, 3610 Collins Ferry Road, Morgantown, WV 26505, USA

[3] University of North Dakota – Mechanical Engineering Department, 243 Centennial Drive, Grand Forks, ND 58202, USA

DOE/NETL-2023/3822

28 October 2022

NETL Contacts:

Douglas Straub, Principal Investigator

Peter Strakey, Technical Portfolio Lead

Bryan Morreale, Associate Laboratory Director for Research & Innovation, Research & Innovation Center

This page intentionally left blank.

Table of Contents

This page intentionally left blank.

List of Figures

List of Figures (cont.)

List of Figures (cont.)

List of Tables

Acronyms, Abbreviations, and Symbols

Term	Description
1D	One-dimensional
2D	Two-dimensional
3D	Three-dimensional
AM	Additive manufacturing
BL	Boundary layer
CAD	Computer aided design
CAT	Conjugate Aerothermal Test rig
CHP	Combined heat and power
CHPD	Combined Heat and Power Data Base
CFD	Computational fluid dynamics
CT	Computed tomography
DOE	U.S. Department of Energy
EPA	U.S. Environmental Protection Agency
EERE	Office of Energy Efficiency and Renewable Energy
FEM	Finite element model
H/D	Height to diameter ratio
HLP	Heat load parameter
HRSG	Heat recovery steam generator
IR	Infrared
LE	Leading edge
NAICS	North American Industry Classification System
NETL	National Energy Technology Laboratory
RANS	Reynolds Averaged Navier-Stokes
SST	Shear stress transport
TC	Thermocouples
TE	Trailing edge
UTSR	University Turbine Systems Research

Acknowledgments

This work was performed by the U.S. Department of Energy's (DOE) National Energy Technology Laboratory's (NETL) Research and Innovation Center to fulfill a proposal awarded by the Office of Energy Efficiency and Renewable Energy's (EERE) Advanced Manufacturing Office (AMO). The authors wish to acknowledge Dr. Bob Gemmer for programmatic guidance, direction, and support. The authors would also like to acknowledge Dr. Geo. Richards and Dr. James Black for their vision and leadership through the early stages of this effort. Finally, the efforts and craftsmanship of Jeff Riley and Rich Eddy were critical for the success of this project.

EXECUTIVE SUMMARY

This report describes a three-year interdisciplinary effort funded by the U.S. Department of Energy's (DOE) Energy Efficiency and Renewable Energy/Advanced Manufacturing Office (EERE/AMO) to promote market penetration of combined heat and power (CHP) technologies. Prior studies have shown the technical potential for CHP in the United States is much larger than the current deployment of CHP systems. A large portion of the technical potential CHP market aligns with small (<20 MWe) gas turbines. CHP systems are an attractive alternative to reduce greenhouse gas (GHG) emissions. For example, CHP systems can reduce GHG emissions by 30–40% relative to a conventional boiler and power configuration. These GHG emission reductions are "avoided emissions" which means no CO_2 separation or sequestration is required.

This report describes an effort to use additive manufacturing (AM) technologies and advanced airfoil cooling designs to increase the turbine inlet temperature by 100 °C for small gas turbines typically used in CHP systems. At the beginning of this effort, baseline performance data for small gas turbines was not available, and the potential benefits of cooling system improvements were not quantified in the available literature.

In this study, a market and benefit analysis was completed to understand the potential impacts of increasing the gas turbine inlet temperature by 100 °C. This study estimated that the potential benefits include: 1) reduction in the pay-back period of approximately one year, and 2) reduction in the cost of electricity of approximately 7% (see Section 2.3).

A public engine model was developed to establish a detailed baseline 5–10 MW turbine, including a model for the cooling system. A sensitivity analysis was performed to investigate the factors having the largest impact on the baseline engine performance. This analysis determined that the internal convective cooling efficiency had one of the strongest effects on the overall system performance. For example, increasing the internal convective cooling efficiency, η_c, from approximately 0.50 to 0.60, could result in a 2-percentage point improvement in the gas turbine efficiency and a 5% reduction in fuel usage per kW-hr (see Section 2.4). This reduction in fuel cost was consistent with the assumptions in the market and benefits analysis. The internal cooling efficiency is a non-dimensional cooling parameter that is often mentioned in the public literature. No experimental data was available for integrated airfoil cooling architectures, particularly for small gas turbines, therefore, some assumptions were necessary in this sensitivity study.

This study also involved a significant experimental effort which included the following: 1) identify baseline airfoil designs for small (5-10 MW) gas turbines used for CHP applications; 2) develop a test protocol to evaluate and rate cooling performance for the baseline, and more advanced, AM airfoil cooling designs; 3) design and additively manufacture internally cooled airfoils for testing in an existing 650 K test facility at NETL; and 4) analyze the experimental results using non-dimensional similarity parameters to scale between laboratory and engine-like conditions. This report contains some of the first reported experimental data of overall cooling effectiveness and internal convective cooling efficiency for integrated internally cooled airfoil designs.

Tests were performed at NETL utilizing the conjugate aerothermal test (CAT) facility, an optically accessible, heated (650 K hot gas path) wind tunnel with an independent coolant plenum. Spatially resolved overall cooling effectiveness was measured using infrared (IR)

imaging. Results were presented for the baseline and advanced designs (five total) as a function of a non-dimensional heat load parameter (HLP) varying from 0.5 to 4. These results indicated that the NETL double-wall cooling architecture can achieve a 100 °C increase in turbine inlet temperature while using less than half of the coolant flow rate required by the baseline design. This result demonstrates the potential impact for AM to improve cooling performance relative to the current state-of-the-art baseline designs.

This project was one of the first fundamental studies to identify baseline engine conditions and baseline cooling designs for small (5–10 MW) gas turbines that are typically used in CHP applications. Baseline cooling designs were identified and packaged into a public airfoil geometry (NACA-0024) which can be used in other studies in the future. Experimentally derived cooling technology curves are presented with curve fit regression coefficients to describe the cooling performance of each airfoil design. Finally, the internal convective cooling efficiency curves are also presented in this report. The type of information described in this report cannot be found in the available literature, particularly for additively manufactured internally cooled airfoil architectures.

1. INTRODUCTION

Currently in the United States, small (<20MW) industrial gas turbines produce roughly 2 GW of electricity in combined heat and power (CHP) applications (DOE, 2020). CHP systems reduce fuel use and greenhouse gas (GHG) emissions by 30–40% relative to non-integrated heat and power systems. Over the next 5 years, more than three million tonnes of CO_2 emissions can be avoided in the U.S. if growth in small (<20 MW) gas turbine CHP systems is close to projections (Straub et al., 2022).

In addition to the environmental benefits, the decision to replace an existing boiler facility with a gas turbine CHP plant is often based on economic pay-back periods, and these pay-back periods are correlated with the heat rate since fuel consumption is the primary operational cost. Therefore, technology advancements to reduce fuel consumption and increase power are of interest for the U.S. Department of Energy's (DOE) Office of Energy Efficiency and Renewable Energy (EERE). This report documents the results of the Phase I study sponsored by EERE's Advanced Manufacturing Office (AMO) which seeks to enable a 100 °C increase in firing temperature for CHP turbines. Although there are several approaches that can be taken to increase the efficiency of small industrial gas turbines, the effort described in this project focused on using advanced manufacturing and advanced cooling designs to achieve these goals.

Additive manufacturing (AM) is an exciting technology for gas turbines since new concepts can be evaluated quickly and at a reasonable cost. Although hot gas path applications for AM materials are limited due to lack of suitable material properties, recent research in AM of CMSX-4 is encouraging (Körner et al., 2018). These material development issues for AM technologies are outside the scope of this report.

AM is a cost-effective means to experimentally validate cooling models. Complete airfoil cooling architectures can be designed, fabricated, and evaluated quickly. Although there have been several previous studies using public airfoil profiles, many of these studies were conducted before AM techniques were common, and thus did not address topics specific to AM, including surface roughness and design for AM. The Energy Efficient Engine (i.e., E^3) Program developed and tested airfoils with detailed internal cooling features, as well as film cooling holes (Thulin et al., 1982; Halila et al., 1982; Gardner, 1981). Other publicly available airfoil profiles, such as the C3X and Mark II vanes were also studied (Hylton et al., 1983; Hylton et al., 1988). The internal cooling channels for the C3X and Mark II vanes were simple cylindrical channels oriented in the spanwise direction of the airfoil. The C3X vane geometry has been widely used for other external film cooling studies. Similarly, the VKI rotor blade design focused on external film cooling and the internal cooling channels were primarily used to deliver coolant to the film cooling hole (Camci et al., 1990; Laskowski et al., 2007).

This project is different from previous public airfoil cooling studies in several ways. In previous public airfoil studies, internal cooling was not the primary objective and the research was focused on higher temperature gas turbine applications. This project did not consider film cooling and focused on internal cooling only. There are several industry publications that support this approach for 5–10 MW gas turbines (Appleyard, 2019; Aschenbruck et al., 2013; GM, 1983; Teraji, 2006). These publications suggest that film cooling upstream of the trailing edge is rarely used in 5–10 MW gas turbine engines. Numerous studies have addressed individual internal cooling features such as impingement cooling (Chupp et al., 1969; Martin et al., 2013; Florschuetz et al., 1981a and 1981b), pin-fin arrays (Metzger et al., 1986; Chyu et al, 1999;

Ames et al., 2007; Jaswal et al., 2009), internal ribs, and other heat transfer enhancements (Han et al., 2013; Han and Park, 1988; Wright and Han, 2014). However, few studies have considered the performance of all elements integrated in a single blade.

The turbine airfoil design methodology as outlined by Bunker (2006, 2017) has been followed in the present effort. As described by Bunker and others (Holland et al., 1980; Cunha, 2006; Downs and Landis, 2009), cooling "technology maps" have been used to compare different cooling designs on a common basis. A technology map relates the non-dimensional overall cooling effectiveness to a non-dimensional quantity called the heat load parameter (HLP) (Holland et al., 1980). The overall cooling effectiveness is a non-dimensional surface temperature (see Equation 1). The HLP represents the ratio of overall coolant heat capacity (heat load absorbed) to external heat flux imposed (see Equation 2). Using technology maps, Cunha (2006) suggests that a maximum cooling effectiveness of approximately 0.6 can be achieved without film cooling using a multi-pass serpentine passage with rib turbulators. Downs and Landis (2009) also used technology maps, or technology curves, to describe a practical limit of approximately 0.8 for overall cooling effectiveness using film cooling and ideal internal cooling.

$$\phi = \frac{T_g - T_{w,ext}}{T_g - T_{c,in}} \tag{1}$$

$$HLP = \frac{\dot{m}_c c_p}{h_{ext} A_{ext}} \tag{2}$$

Although several others have used these technology curves to conceptually compare different cooling technologies, experimentally measured technology curves for an entire airfoil are rarely reported. Bergholz (2008) used a cooling technology map in the discussion of a simplified cooling model to optimize local impingement cooling. Nakamata et al. (2007) investigated the overall cooling effectiveness of flat plate pin-fin arrays with local impingement cooling and film cooling. Both local and area-averaged cooling effectiveness were reported by Nakamata et al. (2007). Stimpson et al. (2018) used technology curves to present results from AM microchannel and film-cooled test coupons. Dyson et al. (2013) presented overall cooling effectiveness profiles for a C3X vane, however, the results were not presented in the non-dimensional form of a traditional cooling technology curve.

In this project, experimentally measured cooling technology curves are described for five different internally cooled airfoils, a baseline blade and vane and three advanced designs. Section 2 of this report outlines the approach of this project including the definition of a baseline engine, an assessment of the market for advanced CHP turbines, performance modeling of baseline and advanced designs, and an overview of the test approach. Section 3 of the report introduces the five internally cooled airfoils considered in the present study. For each design, a design overview is presented including a discussion of manufacturing issues/concerns. Several airfoils were modeled with analytical and/or numerical techniques to predict performance and the results of these efforts are also reported in Section 3. Section 4 reports the experimental methodology. Subsections are devoted to the experimental approach, test facility details, and infrared (IR) camera calibration and image analysis. Section 5 reports the cooling technology curves (i.e.,

overall cooling effectiveness vs. HLP) for the five airfoils considered in the project. Section 5 also includes some of the first reports of internal cooling efficiency measurements for integrated airfoil cooling architectures.

2. APPROACH

2.1 BASELINE DEFINITION

Since one-third of the potential CHP market in the U.S. is concentrated in the 1–20 MWe size range (Hampson et al., 2016), the existing CHP database (DOE, 2020) was queried for gas turbines in the 1–20 MWe size range. The distribution of the existing capacity relative to the gas turbine size showed a peak for gas turbines in the 5–10 MWe size range. This information provided the basis for studying gas turbine engines in the 5–10 MWe range. An annual review of commercial gas turbine generators was published by Gas Turbine World (GTW, 2019) and information from this publication was also analyzed. Figure 1 shows the published efficiencies of engine-generator packages as a function of size. A further justification for selecting the 5–10 MWe range was the number of commercial options in this size bin relative to other sizes. A focus on the more densely populated sizes was expected to increase the impact of this research.

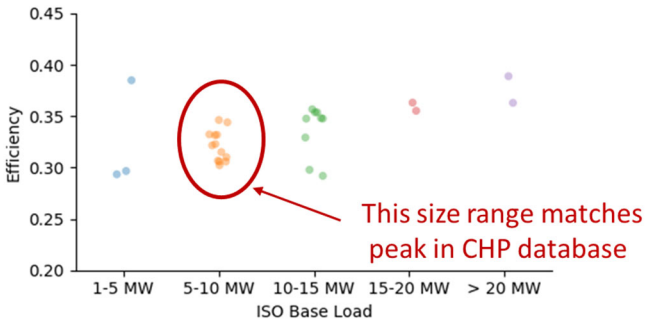

Figure 1: Published gas turbine efficiencies by engine size (1–20 MW) (GTW, 2019).

In addition to reviewing the public literature, feedback from industry helped to verify inputs for an NETL gas turbine performance model (Uysal et al., 2021). The gas turbine model was validated by matching published engine performance parameters for three different commercial engines. Performance parameters such as efficiency, power, and exhaust temperatures were predicted within 3% of the published values.

A new virtual engine was developed to establish a public baseline engine cycle for this research effort. This baseline engine was representative of the engines in the target 5–10 MW size range and the approach allowed the assumptions regarding the engine conditions to be shared and presented. The baseline engine conditions are listed in Table 1. The thermal efficiency, heat rate, power output, and exhaust temperature for the baseline engine were comparable to the specifications for other commercial engines in the size range.

Table 1: Engine Parameters for NETL Baseline CHP Gas Turbine Engine

Parameter	Value
Ambient Temperature	288 K (60 °F)
Ambient Pressure	1.01 bar (14.7 psia)
Inlet Mass Flowrate	21.7 kg/s (47.9 lbm/s)
Compressor Pressure Ratio	14.7
Compressor Polytropic Efficiency	88%
Fuel	Natural Gas
Turbine Inlet Temperature	1,366 K (2,000 °F)
Turbine Polytropic Efficiency	89%
Shaft Rotational Speed	14,700 rpm
Power Output	6,100 kW
Thermal Efficiency	33.1%
Heat Rate	10,209 Btu/kWh (10,771 kJ/kWh)
Exhaust Temperature	793 K (968 °F)

2.2 MARKET ASSESSMENT

A market study was conducted by NETL as part of this project (Theis et al., 2020). The study showed that market forces and barriers significantly limit the current growth of CHP turbine installations relative to the estimated technical potential.

At the time of this assessment, there were 7.1 GW of CHP capacity for units less than 20 MW installed in the U.S. About 33% (2.3 GW) of this capacity was exclusively CHP turbines, less than 20 MW. While small CHP turbines were in use across many sectors, there was a high concentration of small turbines in the petrochemicals, education, and hospital sectors.

Figure 2 shows the CHP capacity and unit counts in the U.S. of CHP turbines less than 20 MW, binned in 5 MW increments. Predictions from two databases, ABB Velocity (ABB, 2020) and Combined Heat and Power Database (CHPD) (DOE, 2020), are shown. The ABB Velocity database estimated more large and small units, but fewer midsize units than the CHPD. Both datasets estimated a similar total capacity of 2,300 MW, and showed a much larger number of very small units (less than 5 MW) than of mid-size units up to 20 MW.

Figure 3 shows the CHP turbine installations less than 20 MW in 5 MW bins for specific North American Industry Classification System (NAICS) codes, reported by the CHPD. Industries with the largest CHP capacity included the petrochemical industry and the education sector, followed by many small units less than 5 MW in the hospital sector.

A market research report on the near future U.S. CHP market predicted that CHP turbines less than 20 MW would grow by 0.6–0.7 GW between 2020 and 2025 (Market Research Future, 2019). This growth was projected to be concentrated in the commercial sector.

Figure 4 shows the growth in market size projected from 2017 to 2025 by end use sector (commercial, residential, industrial, others) for the CHP turbines less than 20 MW. The commercial sector was projected to grow the most, growing by 60% by 2025. The industrial sector was projected to grow by 17%, while the residential sector and others sector were projected to grow by 8% and 4%, respectively.

In 2016, the U.S. DOE conducted a study evaluating the technical potential of CHP in the U.S. (Hampson et al., 2016). Technical potential was defined as the theoretical and technically possible maximum CHP capacity, without consideration of economics or market forces. The study found that in 2016, the U.S. had a technical potential of 240 GW of CHP capacity. The technical potential for CHP units less than 20 MW (turbines and non-turbines) was estimated to be 128 GW. Assuming a potential market share of 33% for small (1–20 MW) gas turbines, 42 GW of technical potential existed. If all the potential growth estimated by the market report (i.e., 0.6–0.7 GW) was seen by 2025, this growth would only represent 6% of the technical potential available in the U.S. Market forces, such as economics, policies, and preferences, as well as market barriers explained the difference between the actual capacity and the technical potential.

The market study included interviews with the operators of CHP turbine facilities at four different universities. These interviews helped identify barriers for CHP turbine installation. Market barriers included low-market electricity prices and high-standby/backup power costs. Regulatory policies that inhibited market entry included permitting and environmental regulations as well as limitations on reselling electricity back to the grid. Economic barriers included high capital cost and long pay-back periods. Finally, technical barriers that need to be overcome included the total system cost and interconnection standards for connecting back to the grid.

Potential small turbine improvements were identified by the NETL and performance gains were estimated. Efficiency and emission improvements were calculated based on technology developments providing an increased electrical output by 17%, a 6% decrease in heat rate, and a 30 °F increase in exhaust temperature. These improvements yielded an efficiency improvement of greater than 5.7 percentage points and a decrease in CO_2 emissions of 7.3–7.7% for 2021–2030 vintage CHP plants. (It is noted that the 5.7 percentage point gain in efficiency reported by Theis et al, (2020) was based on a simplified model and detailed modeling by Uysal et al. (2021), reported in Section 2.3 reduced the estimated improvement to three percentage points.) To determine the impact of the potential advancements on CHP costs, three technology improvements cases were developed to compare to the baseline costs reported in a California cost of electricity report (ICF International, 2012). The best case included an electrical output increase of 24.4%, a 6% decrease in heat rate, and a 30 °F increase in exhaust temperature. This case resulted in a decrease of the total cost of electricity by 7.2% and reduced the pay-back period by over one year.

The total specific CO_2 emissions per total output (electric and thermal) was calculated for the baseline technology, improved technology, and conventional (separate electrical generation and gas-fired thermal generation) cases and are presented in Figure 5. The technology improvements decreased CO_2 emissions by 7.3–7.7%. The figure also illustrated the significant (36%) CO_2

emissions improvement of CHP over conventional (separate) heat and power generation for a 10 MW class system.

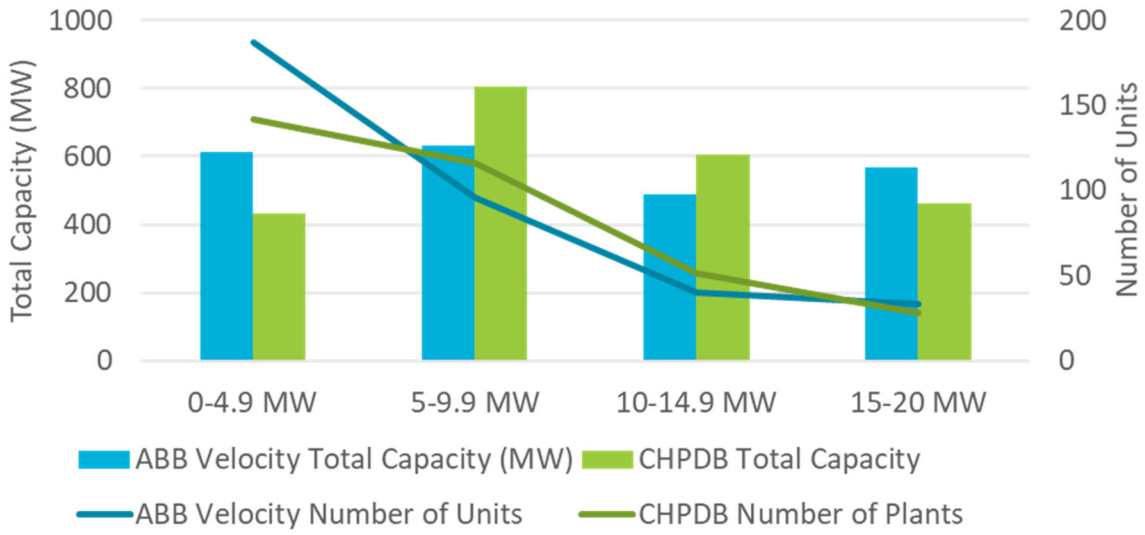

Figure 2: Turbine CHP installations less than 20 MW. Adapted from Theis et al. (2020).

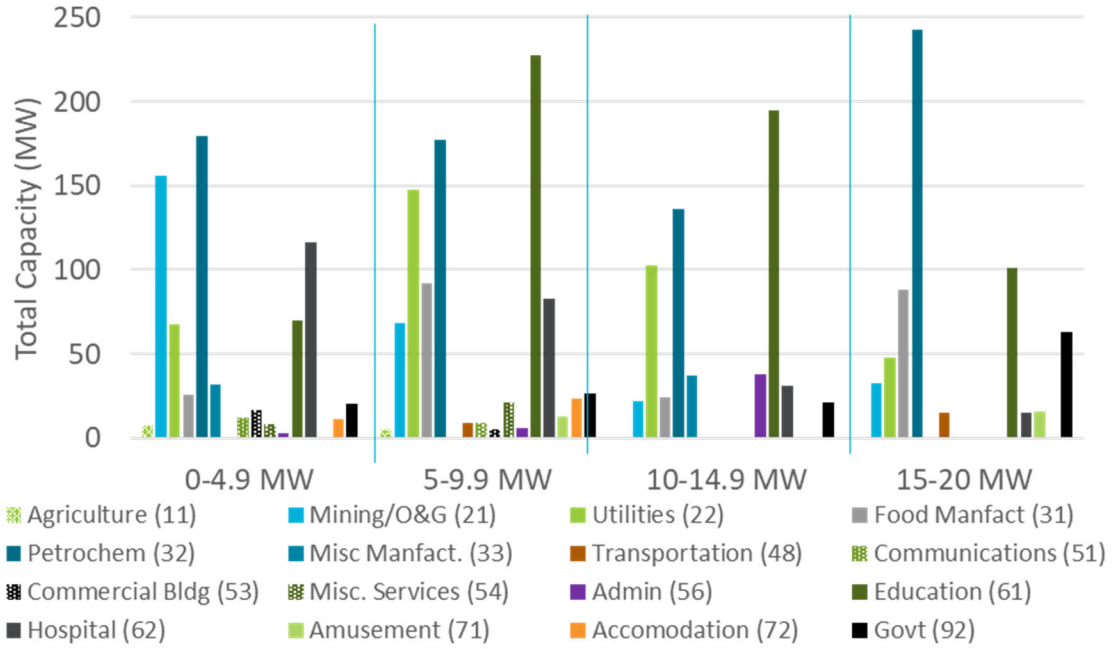

Figure 3: CHP turbine installations less than 20 MW by NAICS code. Adapted from Adapted from Theis et al. (2020).

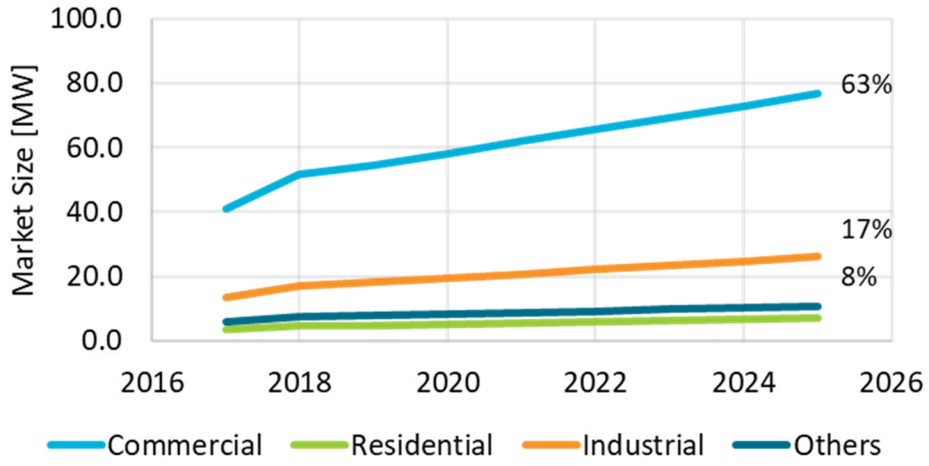

Figure 4: Potential CHP installations turbines less than 20 MW by end use sector. Adapted from Theis et al. (2020).

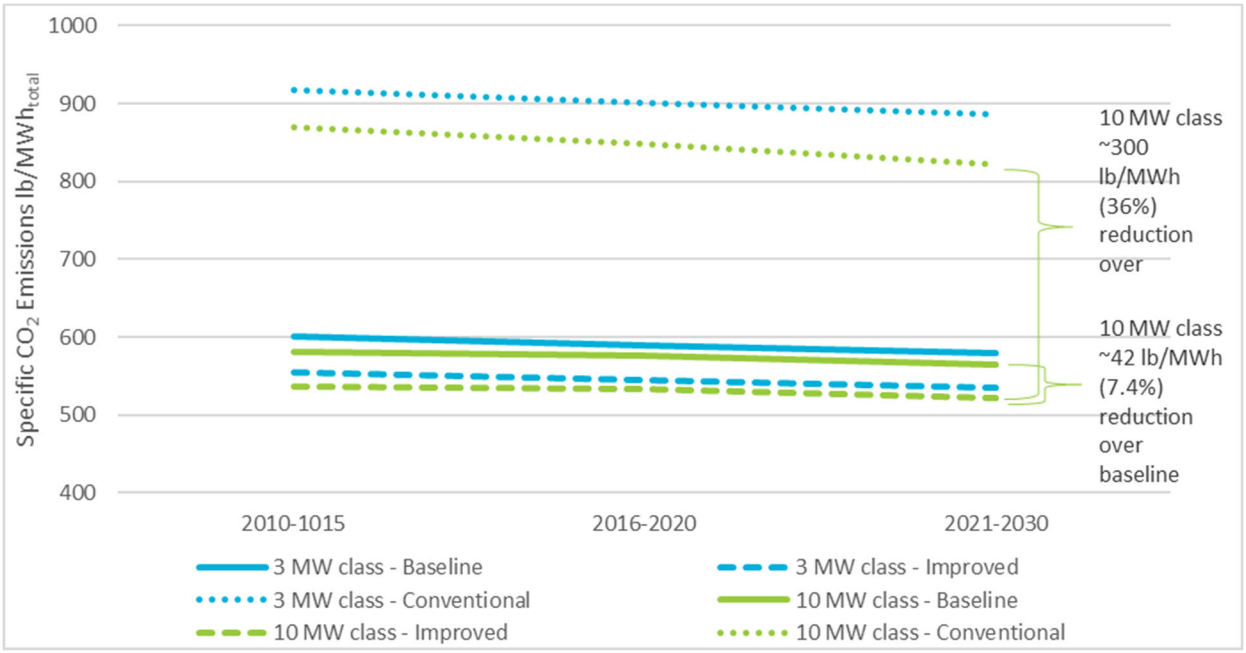

Figure 5: 3 MW and 10 MW specific CO_2 emissions based on total (electric and thermal) output. Adapted from Theis et al. (2020).

2.3 PERFORMANCE MODELING

The impact on CHP cycle performance from increasing the turbine firing temperature by 180 °F (100 °C) and from improving the turbine blade cooling for a 6-MW scale gas turbine was determined using an analytical-cooled gas turbine model and a steam cycle model. The model was benchmarked against publicly available data for three gas turbines of similar scale as

mentioned in Section 2.1. The final baseline engine model was a virtual public engine, which was representative but not identical to any commercially available engine.

A review of current CHP facilities (<25 MW) showed two primary gas turbine categories: lower power range (3–12 MW) and higher power range (12–25 MW). The lower power range engines had higher shaft speeds, single shaft configurations, and efficiencies ranging 27–35%. For the higher power range, the shaft speeds were lower and efficiencies were higher than 35%. These engines were aero-derivatives and featured dual-shaft designs. Based on historical and projected CHP market data, the study assessed gas turbines in the lower power range—specifically, 5–10 MW.

To realize the full benefit of increasing the firing temperature, the gas turbine pressure ratio should also increase. The present study intended to minimally change the aerodynamic design of the gas turbine, and thus, the shaft speed was not changed for the upgraded design. For a fixed shaft speed, when the turbine inlet temperature increases, the gas turbine pressure ratio increased following the compressor curve. Further efficiency improvement was achieved by increasing the cooling effectiveness.

A sensitivity analysis was performed to understand the impact of increasing the internal cooling effectiveness, thermal barrier coating performance, and blade material upgrades on gas turbine and CHP cycle efficiency. The impacts of turbine blade cooling improvements were studied for a common CHP cycle configuration identified from the literature.

Various CHP plant configurations can be realized depending on plant size, and electricity and steam end-use. A gas turbine with a heat recovery steam generator (HRSG) may be configured with or without low-capacity or conventional steam turbines to increase electric power output and allow efficient extraction of high- and low-pressure steam. The configuration considered in this particular study included a conventional steam turbine.

The HRSG may be fired to increase steam output (i.e., a burner can be installed in the HRSG to heat the gas turbine flue gas to higher temperatures). Both fired and non-fired HRSG configurations were considered in the study.

Four definitions for CHP cycle efficiency from the literature were used in the comparisons: 1) total efficiency, 2) effective electrical efficiency, 3) combined efficiency, and 4) true efficiency. The first two (total and effective electrical) follow U.S. Environmental Protection Agency (EPA) calculation recommendations. The first (total) adds the useable heat to the electric work term, but violates the second law of thermodynamics. The second (effective electrical efficiency) modifies the cycle heat input to account for useful heat extracted from the process. These metrics are simple to calculate with overall plant performance data. The third and fourth (combined and true) require a more detailed system model. Combined efficiency includes the exergy at the gas turbine exhaust flow, the steam cycle efficiency, gas turbine exhaust temperature, and the HRSG inlet and exit temperature. True efficiency was calculated by including the exergy generated by all CHP cycle components.

The results showed that a 180 °F (100 °C) increase in firing temperature increased the gas turbine efficiency by 1 percentage point without advanced cooling technology and 2 additional percentage points in efficiency could be achieved by using advanced turbine blades with higher internal cooling efficiency.

Gas turbine power and efficiency were displayed as a function of compressor pressure ratio in Figure 6 for internal cooling efficiency varying from 0.62 (baseline) to 0.7. Data labels show turbine exhaust temperature in °F. As expected, both gas turbine power and efficiency increase with increasing internal cooling efficiency. Maxima for both efficiency and power as a function of pressure ratio may be identified. Beyond these maxima, the efficiency and power begin to decrease as the compressor performs less efficiently at off-design conditions.

The engine upgrades showed potential for increasing the CHP cycle efficiency by 3 percentage points, while increasing the steam generation rate by 8%.

CHP cycle efficiency with and without internal cooling improvements are displayed in Figure 7 for four efficiency metrics. The impact of the higher firing temperature and advanced blades with internal cooling efficiency 13% higher than the baseline blade was an increase of 1.42 percentage points for the true efficiency, 3.43 percentage points for the combined efficiency, 2.58 percentage points for the effective electrical efficiency, and 1.89 percentage points for the total efficiency when compared to the baseline engine.

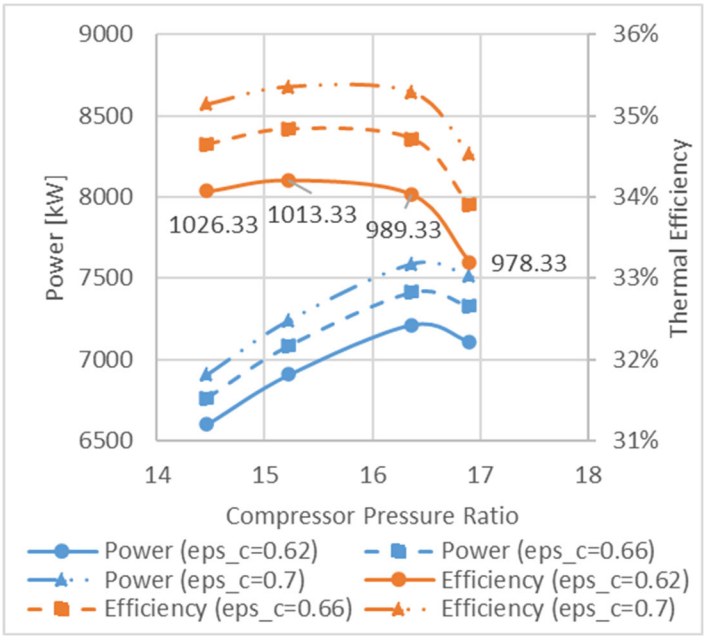

Figure 6: Upgraded CHP gas turbine performance for various pressure ratio and blade internal cooling effectiveness value; data labels show gas turbine exhaust temperature in °F. Adapted from Uysal et al. (2021).

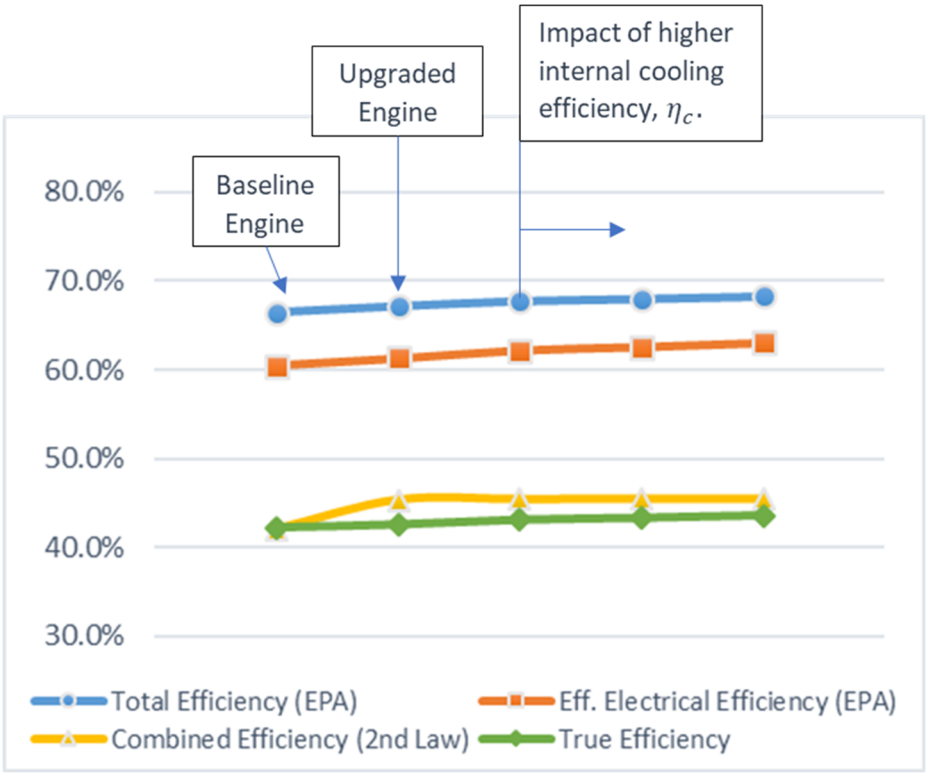

Figure 7: Impact of advanced turbine blades on CHP cycle efficiency (non-fired HRSG) compared with four different efficiency definitions. Adapted from Uysal et al. (2021).

2.4 OVERVIEW OF TEST APPROACH

To achieve the project goal, baseline and advanced airfoil designs were fabricated using metal three-dimensional (3D) printing and tested in an existing test facility at NETL. The objective was to develop advanced cooling designs which have sufficiently high internal cooling efficiency and where the turbine firing temperature can be increased by 100 °C.

The overall cooling effectiveness, ϕ, (Equation 1) and internal cooling efficiency, η_{th}, were measured for each airfoil design as a function of the HLP.

$$\phi = \frac{T_g - T_{w,ext}}{T_g - T_{c,in}} \quad (1)$$

where T_g is the gas temperature, $T_{w,ext}$ is the external wall metal temperature, and $T_{c,in}$ is the coolant inlet temperature.

The HLP is defined in Equation 2.

$$HLP = \frac{\dot{m}_c c_p}{h_{ext} A_{ext}} \quad (2)$$

where $\dot{m}_c$ is the total coolant mass flow, c_p is the specific heat of the coolant, h_{ext} is the area averaged external heat transfer coefficient, and $A_{ext}$is the external heat transfer area.

The internal cooling efficiency was a parameter often referenced in the gas turbine cooling literature, however, experimentally measured values have not been previously reported. The internal cooling efficiency is defined as the amount of heat transferred to the coolant before it leaves the airfoil (see Equation 3). For example, as the coolant outlet temperature approaches the metal wall temperature, the internal cooling efficiency increases.

$$\eta_c = \frac{T_{c,out} - T_{c,in}}{T_{w,ext} - T_{c,in}} \quad (3)$$

The performance modeling results described in the previous section of this report showed the efficiency for the gas turbine could be increased by approximately 1.4 percentage points in “true efficiency”, if the internal cooling efficiency (Equation 3) could be increased from 0.62 to 0.70. The differences in internal cooling efficiency that were observed in the testing phase were much larger than anticipated in the performance model. In other words, the baseline values measured in this study were lower than the assumptions in the model. Figure 8 shows the potential benefits in gas turbine efficiency that can be achieved as the internal cooling efficiency is increased.

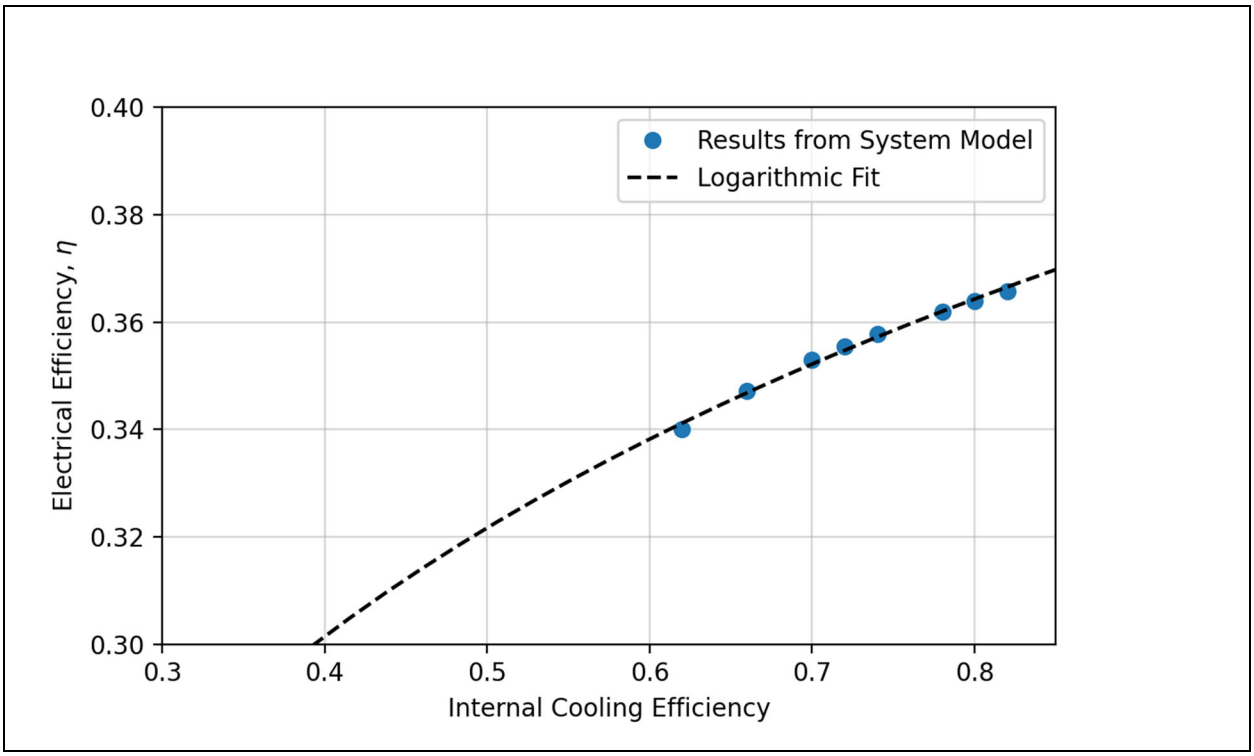

Figure 8: CHP electrical efficiency as a function of internal cooling efficiency parameter, η_c.

Figure 9 shows similar improvements in heat rate that can be realized for small 5–10 MW gas turbine CHP systems as the internal cooling efficiency is increased. For example, increasing the internal cooling efficiency from 0.50 to 0.60 would reduce the normalized fuel consumption by approximately 500 BTU/hr for each kilowatt (kW) of power produced. This would be comparable to a 5% reduction in fuel usage, which could translate to a 5% reduction in fuel cost on a per kW-hour basis.

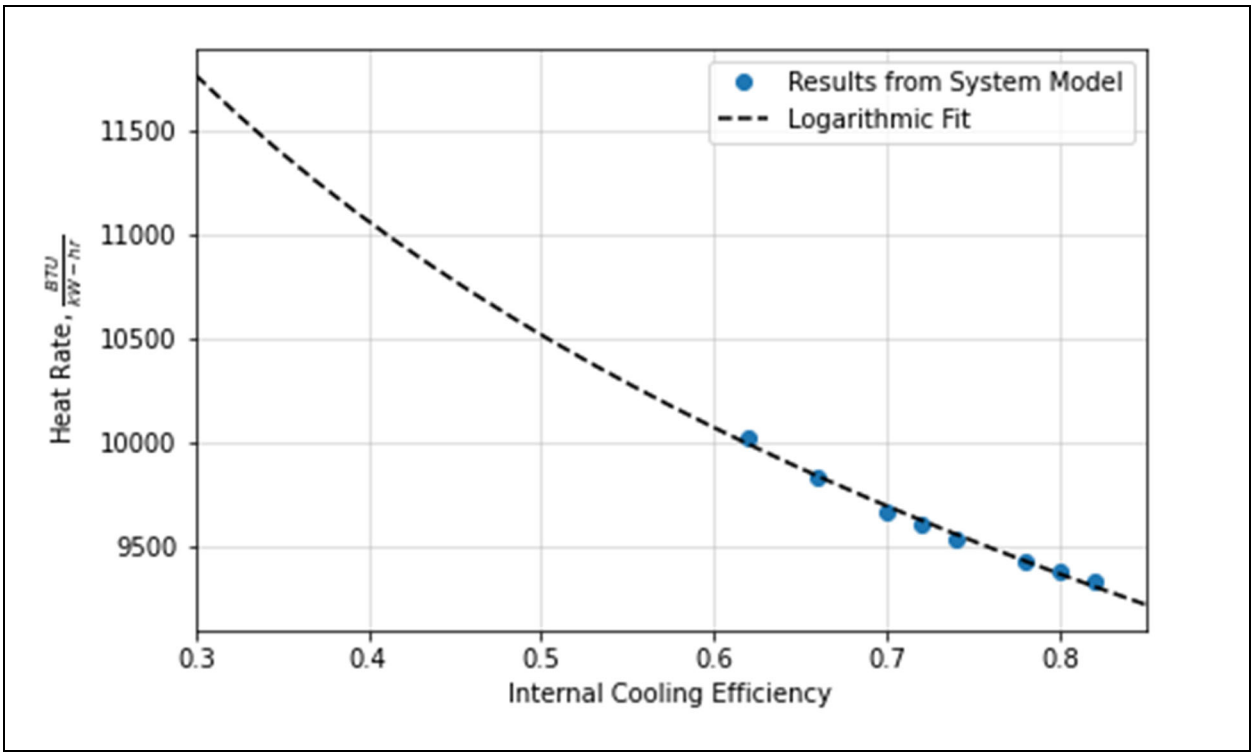

Figure 9: CHP heat rate as a function of internal cooling efficiency parameter, η_{int}.

A conjugate heat transfer test facility at NETL was used to compare the different cooling designs at steady-state conditions (this test facility was described previously in Ramesh et al. (2021)). In this experimental rig, the external flow conditions were kept the same for all cooling designs. The free-stream conditions included: 1) hot gas temperature of 650 K, 2) rig pressure of 110 kPa, and 3) free-stream velocity of 120 m/s. The inlet cooling temperature was also kept constant at 325 K. This provided a hot gas-to-coolant temperature ratio of 2:1. The coolant mass flow rate was varied for each test article.

An IR camera and an optical measurement technique (Ramesh et al., 2021) were used to measure the airfoil surface temperature. These surface temperatures were converted to overall cooling effectiveness and internal cooling efficiency. These results are described in more detail in Section 4.

3. AIRFOIL COOLING DESIGNS

In this section, the different airfoil cooling designs are described. The airfoil external profile is introduced in Section 3.1. This profile and the experimental flow conditions determined the external heat load, which is discussed in Section 3.2. Cooling scheme design objectives are also introduced in Section 3.3. In Sections, 3.4–3.9 each of the airfoil cooling designs considered in this project are described.

All the airfoils discussed were additively manufactured using a laser powder bed fusion process. Maraging Steel M300 powder was used, and the build directions were from the base plate to the tip of the airfoil (i.e., a span-wise build direction). The span-wise build direction and the Maraging steel were selected by the additive manufacturer to provide a more uniform, smooth surface finish for the external airfoil surface.

3.1 EXTERNAL AIRFOIL PROFILE

To make comparisons between different cooling designs, a standardized external airfoil profile was selected and used. A symmetric airfoil shape was described previously by Straub et al. (2021, 2022). There were several reasons for choosing this airfoil profile. First, this was a simple approach and many of the same external heat load features were present (i.e., flow separation and boundary layer transitions). Secondly, a symmetric airfoil can be evaluated in an available test facility with no major modifications.

The NACA-0024 symmetric airfoil shape was used for all the cooling designs (Selig, 2021). The theoretical chord length was 50.8 mm (2.0 in.) and the maximum thickness (24% of theoretical chord) occurred at 30% of the chord. The actual chord length of the airfoil was truncated at 43.7 mm (1.72 in.) to maintain enough trailing edge thickness for ejecting coolant into the trailing edge wake. The airfoil span was 53 mm (2.1 in.). Based on the chord length, the Reynold's Number on the external surface was approximately 90,000.

3.2 EXTERNAL HEAT LOAD

Since the external flow conditions and the airfoil profile were kept constant, the external heat load profile was also constant for all internal cooling designs. Previously, a computational fluid dynamics (CFD) model was used to estimate the heat load profile (Straub et al., 2021). In a second approach (reported in Straub et al. 2022), the airfoil pressure distribution predicted by the CFD model was used to estimate of the local isentropic Mach number and the associated free-stream velocity distribution over the surface. The free-stream velocity distribution was used to drive a boundary layer (BL) code, STAN7 (Kays, 1987). The properties were evaluated at the test rig conditions. Plots of both predicted external heat load distributions are shown in **Error! Reference source not found.**. Transition at a surface distance of approximately 25 mm was predicted due to a separation bubble. For the BL code prediction, the dip in heat transfer at a surface distance of ~35 mm was due to a strong adverse pressure gradient predicted by the CFD simulation. For over 60% of the airfoil, these two approaches agreed. The primary differences were associated with the transition region, and this resulted in a difference in the average heat transfer coefficient. The average heat transfer coefficient for the BL code was approximately 280 W/m^2-K compared to 234 W/m^2-K for the CFD model. The average heat transfer coefficient calculated from the BL code will be used in this paper to define the HLP (see Equation. 2).

These external heat load predictions were based on some assumptions, including smooth and isothermal surfaces with negligible radiative heat loads. Although deviations from these idealized conditions can affect the external heat load, the primary objective was to produce a consistent heat load profile for all the internal cooling designs. If the external thermal resistance was constant, then the effect of varying the internal cooling flow allowed independent control of the HLP and the internal thermal resistance.

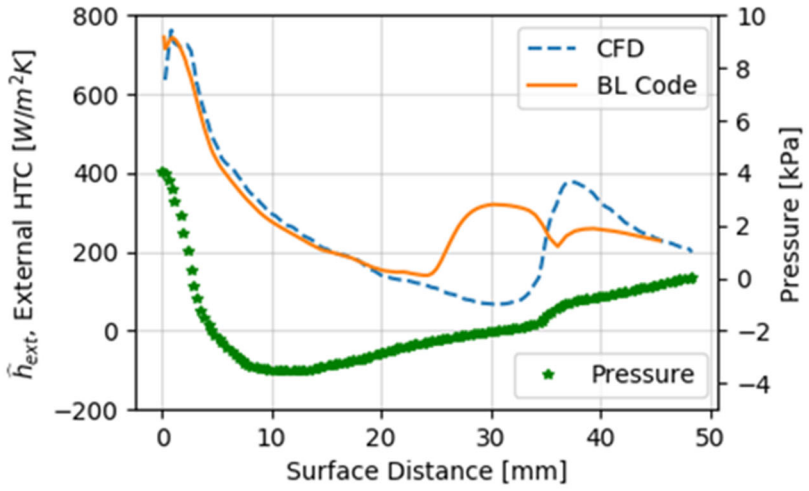

Figure 10: External airfoil heat transfer coefficient and pressure profiles. Adapted from Straub et al. (2022).

3.3 INTERNAL COOLING DESIGN OBJECTIVES

The cooled gas turbine model described in Section 2 was used as a basis for the hot gas path and cooling air conditions. The model assumed a maximum metal temperature for the first stage vanes and blades of 1,178 K (Uysal et al., 2021). The gas temperature was 1,366 K. The coolant temperature for the first stage components was 685 K and was supplied from the last compressor stage. Not accounting for the temperature drop across the thermal barrier coating, the overall cooling effectiveness for the baseline engine design was $\phi_{base} = 0.28$.

If the turbine firing temperature was increased by 100 °C and the coolant temperature remained constant, then the required cooling effectiveness for the advanced engine design would be $\phi_{adv} = 0.37$. These design objectives and the pressure drop constraint have been summarized in Table 2. This pressure drop constraint was related to the test rig.

At this point, it is important to introduce two additional definitions for overall cooling effectiveness, average and 99th percentile, which are different than the overall cooling effectiveness targets discussed here and were measured directly from the experiments as described in Section 4. Average overall cooling effectiveness, ϕ_{avg}, was calculated with the average wall external temperature, $T_{w,ext}$, using Equation 1; ϕ_{99}, was calculated with the 99th percentile of $T_{w,ext}$. For the advanced design goal, ϕ_{99} should exceed ϕ_{adv} such that 99% of the external wall temperature is less than the maximum allowable material temperature.

Table 2: Cooling Design Performance Targets

Design Variable	Design Goal
Overall cooling effectiveness (Equation 2)	$\phi_{99} > 0.37$
Heat load parameter (Equation 3)	$minimize\ HLP$
Coolant pressure drop	$\Delta p_c < 35\ kPa\ (5\ psi)$

3.4 BASELINE VANE

3.4.1 Overview of Design

For the baseline vane internal cooling design (Straub et al., 2021, 2022), cooling air was supplied by a single plenum and distributed to the internal airfoil surface using an impingement shield as shown in Figure 11a. All the impingement coolant combined to flow through the four rows of staggered pins in the trailing edge. The coolant exited the airfoil through racetrack holes as shown in Figure 11c. There were two instrumentation ports for internal pressure probes as shown in Figure 11b.

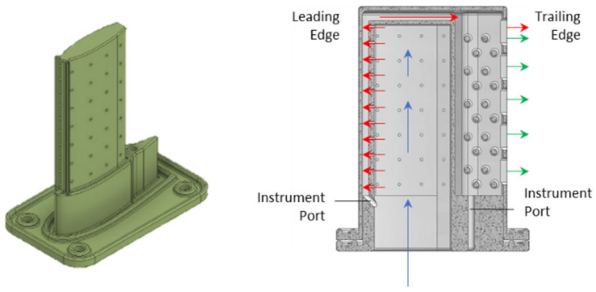

(a) (b)

(c)

Figure 11: Baseline vane – a) impingement shield; b) section view of vane shell; and c) photos of the as-built parts. Adapted from Straub et al. (2022).

Impingement cooling was used for both the leading edge and the mid-chord region of the vane using a single coolant supply plenum. Impingement cooling is a very effective internal cooling technique and has a long history in the gas turbine industry. In impingement cooling, an array of high-velocity jets hits a target plate at a specified distance from the holes creating a high heat transfer region around the stagnation region. Traditionally impingement cooling is employed in high heat transfer regions like the leading edge and combustor liners. The first stage vane was exposed to hot gases exiting from the combustor directly; therefore, the baseline design for the first stage vane incorporated an impingement shield to direct coolant jets against the internal wall of the vane. In the trailing edge, fully-bridged pin-fins were used as heat transfer enhancements, and the coolant was ejected from the trailing edge.

Film cooling, including showerhead film cooling, was not included in the baseline design. Although cooling design details were limited in the public literature, there was some evidence to support these types of heat transfer enhancements for gas turbines in the 5–10 MW size range (Aschenbruck et al., 2013; GM, 1983). A parameter table summarizing the baseline vane design is shown in Table 3 below.

Table 3: Summary of Conceptual Design for Baseline Vane

Geometry	Variable	Symbol	Value (SI)	Value (English)
Leading Edge Impingement	Hole diameter	d	0.9 mm	0.034 in.
	Target diameter	D_{LE}	4.3 mm	0.169 in.
	Hole-target spacing	ℓ	1.8 mm	0.070 in.
	Spacing (span-wise)	s	4.6 mm	0.180 in.
	Number of jets per row	N_j	11	
	Number of rows	$N_{j,rows}$	1	
Mid-Chord Impingement	Hole diameter	d	0.8 mm	0.031 in.
	Hole-target distance	ℓ	1.6 mm	0.061 in.
	Spanwise spacing	s	7.1 mm	0.278 in.
	Chordwise spacing	x	6.4 mm	0.250 in.
	Number of jets per row	N_j	7	
	Number of rows	$N_{j,rows}$	4	
Trailing Edge Pin-Fin Array	Pin diameter	D_p	1.6 mm	0.063 in.
	Spacing (spanwise)	s_p	8.3 mm	0.328 in.
	Spacing (chordwise) [1]	x_p	2.5 mm	0.100 in.
	Number of pins per row	N_p	5	
	Number of rows	$N_{p,rows}$	4	

3.4.2 Manufacturing Issues/Concerns

There were some manufacturability concerns with the downward-facing surfaces on the pins in the trailing edge. To address these manufacturability issues, a 0.5-mm fillet radius was included between the pin and the outer shell of the airfoil. To transition from the sides of the airfoil to the tip of the airfoil, a 1 mm chamfer was used with a 1.3 mm fillet to the tip and a 1 mm fillet to the side walls.

3.4.3 Internal Cooling Correlations

The average Nusselt Number and heat transfer coefficient along the leading edge was approximated using the Chupp correlation (Chupp et al., 1969; Martin et al., 2013) as shown in Equation 4. According to Martin et al. (2013), some of the applicable ranges for this correlation were revised. These revisions included the jet Reynolds Number range (3,000 < Rej < 20,000) and the ratio of the target distance to the jet diameter (4 < ℓ/d < 10). The hole diameters and the number of holes for both the leading edge and the mid-chord region were a balance of minimum feature size limitations and the desired coolant mass flow ranges that achieve the cooling effectiveness target.

$$Nu = 0.44 Re_j^{0.7} \left(\frac{d}{s}\right)^{0.8} \exp\left\{-0.85 \left(\frac{\ell}{d}\right)\left(\frac{d}{s}\right)\left(\frac{d}{D_{LE}}\right)^{0.4}\right\} \quad (4)$$

For the mid-chord region, the flat-plate impingement cooling correlations provided an estimation for the internal Nusselt Number. However, crossflow effects significantly reduce the heat transfer effectiveness of the impingement jets. The approach outlined by Florschuetz et al. (1981) was used to account for these crossflow effects. The average Nusselt Number for the first row of holes was estimated by Equation 5.

$$Nu_1 = 0.363 \left(\frac{x}{d}\right)^{-0.554} \left(\frac{s}{d}\right)^{-0.422} \left(\frac{\ell}{d}\right)^{0.068} Re_j^{0.727} Pr^{0.3} \quad (5)$$

An in-line array of impingement jets was selected for the baseline, since according to the data from Florshuetz et al. (1981a and 1981b), the differences between the inline and staggered impingement jet arrays were small. Using the constants for an in-line impingement jet array, the reduction in Nusselt Number due to crossflow effects was estimated by Equation 6. In these expressions, "x" and "s" were the chordwise and spanwise jet spacings, respectively. The Nusselt Number was based on the impingement hole diameter, denoted as "d", and the spacing between the impingement shield and the target surface, denoted as "ℓ". This nomenclature is consistent with Equation 4.

$$\frac{Nu}{Nu_1} = 1 - 0.596 \left(\frac{x}{d}\right)^{-0.103} \left(\frac{s}{d}\right)^{-0.38} \left(\frac{\ell}{d}\right)^{0.803} \left(\frac{G_{cf}}{G_j}\right)^{0.561} \quad (6)$$

For the trailing edge, a staggered pin-fin array was used. This configuration was studied extensively in literature (Metzger et al., 1986; Chyu et al., 1999; Jaswal et al., 2009). For the thermal resistance analysis presented in this paper, the heat transfer areas for the pins and the wall were considered separately, and the approach described by Cunha (2006) was followed. The Nusselt number and Reynolds number were based on the pin diameter and the reference velocity in the Reynolds number was based on the maximum velocity at the minimum cross-sectional area between adjacent pins. The pin Reynolds numbers were less than 2 x 10^5, therefore, Equation 7 should be used if s/x > 2, and Equation 8 should be used if s/x < 2.

$$Nu_p = 0.40\, Re_p{}^{0.60}\, Pr^{0.36} \tag{7}$$

$$Nu_p = 0.35\left(\frac{s_p}{x_p}\right)^{0.2} Re_p^{0.6} Pr^{0.36} \tag{8}$$

The heat transfer to the endwalls was also included in the analysis. Equation 9 was used to estimate the wall heat transfer coefficient (Cunha, 2006).

$$Nu_w = 0.077 Re^{0.70} \tag{9}$$

3.4.4 Simplified Cooling Model

This section describes the baseline vane cooling performance. The purpose of this analysis was to develop predicted technology curves for the baseline vane. The baseline cooling performance curve was used to evaluate more advanced cooling concepts.

For the simplified model, a thermal resistance network was used to model the heat flux through 1) the hot gas interface, 2) the airfoil wall, and 3) the coolant gas interface. An area-weighted equivalent resistance was calculated at each row of impingement jets and pins along the chord of the airfoil (see Figure 12). This model was used to predict a cooling performance curve for a range of coolant flow rates.

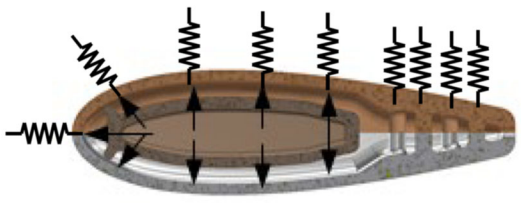

Figure 12: Equivalent thermal resistance model for the baseline vane.

For this analysis, the cooling air flow split to the leading edge and the mid-chord region was controlled by the size of the impingement jets and the number of holes in the impingement shield. All the cooling air that entered the leading edge was directed in the span-wise direction toward the tip and then flowed over the impingement shield to exit through the trailing edge. The cooling air flow through the trailing edge was the sum of the mid-chord coolant (both sides) and the leading-edge coolant flows. For this analysis, the overall HLP for the vane varied from 0.6–5.4.

The thermal conductivity of the wall was roughly 20 W/m-K and the wall thicknesses were nominally 1-mm thick. The thermal wall resistances were 50–100 times smaller than the internal and external resistances. Although the wall resistances were included in the analysis, they could have been neglected without significantly impacting the results. The wall resistances will not be discussed further.

The internal surface areas were measured from a computer aided design (CAD) model, and the external surface areas were calculated by integrating the formula describing the airfoil profile (Straub et al., 2021). Generally, the calculated external surface area agreed to within 0.5% with the CAD model, except for the leading edge, where the difference was on the order of 3–4%. These surface areas were necessary to calculate the external resistances along the airfoil profile.

The external heat transfer coefficients for different regions of the airfoil were calculated from the CFD predictions shown in Straub et al. (2021). Area averaged values for the external heat transfer coefficient were combined with the external surface areas to calculate the external thermal resistance at key points along the airfoil.

The internal heat transfer coefficients and internal resistances for each region were calculated using the design parameters and correlations described in the previous section.

Figure 13 shows the results of this cooling performance analysis for the overall airfoil design. The cooling effectiveness, ϕ, and the internal cooling efficiency, η_{th}, meets, or exceeds, the overall cooling performance objectives based on the baseline engine conditions.

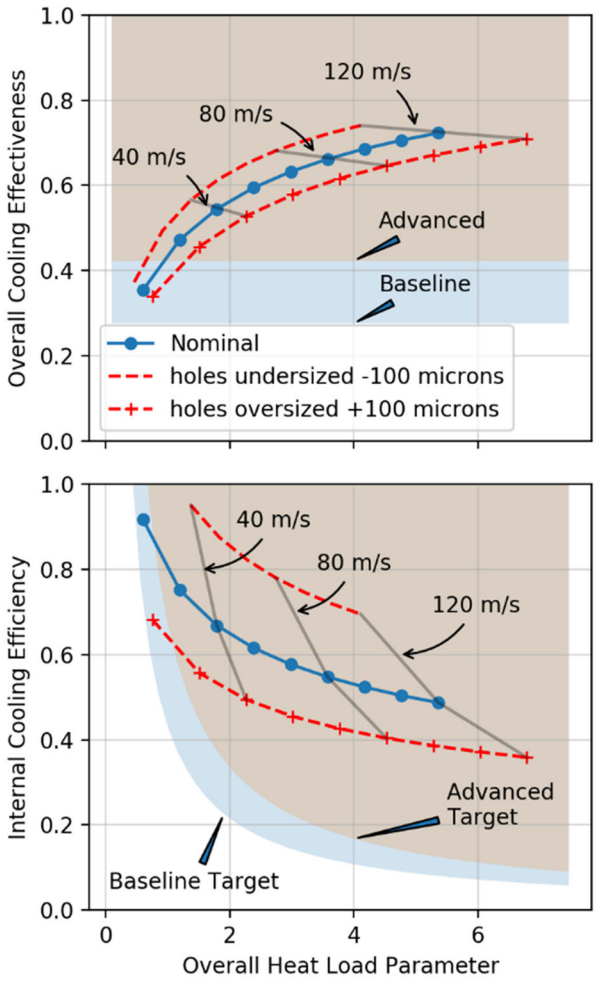

Figure 13: Baseline vane cooling performance curves (overall). Adapted from Straub et al. (2021).

Although this baseline design meets the minimum cooling performance target, Figure 13 can provide additional insight into the potential effects of AM tolerances. The impingement jet diameters have been selected to be larger than the minimum feature size for a direct metal laser sintering process; however, hole tolerances can be affected by build direction, powder particle size, etc. This model was used to estimate the potential impacts from slight variations in impingement jet hole diameters. For this analysis, the jet velocity was kept constant and the hole diameters were varied 0.1 mm (100 microns). The results are shown in Figure 13 with a dashed line indicating 0.1 mm undersized and a dashed line with plus markers indicating 0.1 mm oversized. This analysis assumes every hole will vary the same amount and the constant velocity assumption approximates a constant pressure drop. Lines of constant velocity are also shown for some operating points to illustrate these effects. If the impingement hole diameters were decreased, the coolant mass flow would be reduced, and the overall cooling effectiveness increases slightly. For the internal cooling efficiency, the variations in hole diameter have a much larger effect because both the cooling mass flow rate and the internal thermal resistance

decrease. These results show that the cooling hole diameters and variations from the design were important to quantify for the AM airfoil testing.

Figure 13 provides an area-averaged perspective of the cooling performance for the baseline vane, but the local regions of the airfoil were also of interest. The local cooling effectiveness was shown in Figure 14. The cooling air flows for these cases corresponded to overall HLP of 0.6, 3.0, and 5.4. Potential problem areas were apparent. The leading edge and the trailing edge regions had a low cooling effectiveness (high relative wall temperature) at the lowest cooling air flow; however, the performance improved as the cooling air flow was increased. The leading edge and the region downstream of the boundary layer transition required more advanced cooling strategies; however, the baseline concepts met the minimum performance criteria and provided an adequate baseline for this study.

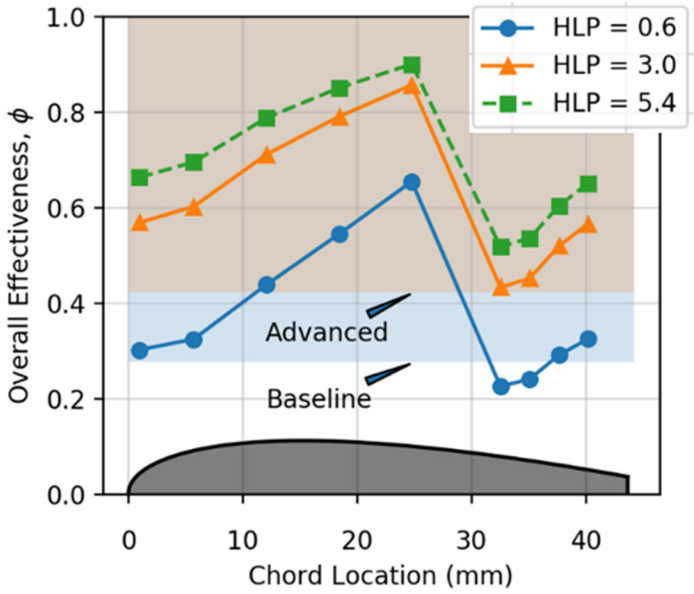

Figure 14: Local cooling effectiveness predictions for baseline vane. Adapted from Straub et al. (2021)

3.5 BASELINE BLADE

3.5.1 Overview of Design

For the baseline blade (Straub et al., 2021, 2022), two inlets supplied cooling air to the internal cooling channels. The first inlet plenum supplied coolant to the fore serpentine pass which subsequently provided impingement coolant for the leading edge through a series of cross-over holes (see Figure 15(b)). The coolant impinged on the leading-edge wall and flowed toward the tip and through a dedicated duct near the tip. Rib-turbulated serpentine cooling was utilized in the mid-chord region. The second inlet plenum supplied fresh coolant to the second serpentine pass and the trailing edge. The aft-wall of the second serpentine passage had cross-over holes to distribute coolant to the trailing edge pin-fin array. Pin-fin cooling was utilized in the trailing

edge and all the coolant was exhausted through trailing edge racetrack holes (see Figure 15(c)). The dimensional details of the individual cooling features are summarized in Table 4.

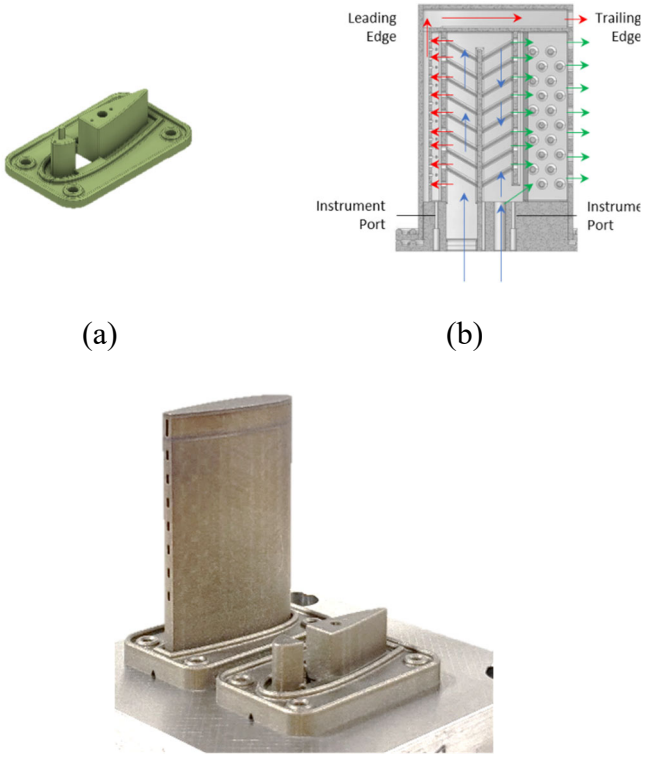

Figure 15: Baseline blade – a) blade insert and inlet flow orifice; b) section view of blade shell, and c) photos of the as-built parts. Adapted from Straub et al. (2022).

Table 4: Summary of Conceptual Design for Baseline Blade

Geometry	Variable	Symbol	Value (SI)	Value (English)
Leading Edge Impingement	Hole diameter	d	0.8 mm	0.032 in.
	Target diameter	D_{LE}	4.2 mm	0.166 in.
	Hole-target spacing	ℓ	1.7 mm	0.065 in.
	Spacing (span-wise)	s	4.5 mm	0.178 in.
	Number of jets per row	N_j	10	
	Number of rows	$N_{j,rows}$	1	
Mid-Chord Serpentine with ribs	Channel height,	H	8.6 mm	0.338 in.
	Hydraulic diameter,	D_h	8.7 mm	0.343 in.
	Trip strip height,	e	0.6 mm	0.025 in.
	Trip strip pitch spacing,	p	5.1 mm	0.200 in.
	Trip strip angle,	α	60°	
Trailing Edge Pin-Fin Array	Pin diameter	D_p	1.6 mm	0.063 in.
	Spacing (spanwise)	s_p	8.3 mm	0.328 in.
	Spacing (chordwise)[1]	x_p	2.5 mm	0.100 in.
	Number of pins per row	N_p	5	
	Number of rows	$N_{p,rows}$	4	

The mid-chord region of the baseline blade consisted of a serpentine cooling channel with trip strip heat transfer enhancements. These trip strips had a relative rib height of 7% of the channel hydraulic diameter, and a pitch spacing to rib height of 8. The ribs were oriented 60° relative to the coolant flow direction. These internal heat transfer enhancements have been thoroughly studied by others (Han and Wright, 2007; Han and Park, 1988; Han et al., 1989, 2013) and this prior work was the basis for these geometric details.

3.5.2 Manufacturing Issues/Concerns

Like the baseline vane design, there were some manufacturability concerns with the downward facing surfaces. Radii (0.8 mm) were included on the pin-to-endwall interfaces, and 0.5 mm radius was included along the downward-facing tip-to-internal airfoil wall interfaces. The ribs in the serpentine coolant path were also given fillet radii of 0.4 mm along all interfaces.

There were also issues with sealing the internal flow passages at the interface between the blade insert and the internal channel walls (i.e., the wall separating the serpentine passages). Since the AM build direction was from the base of the airfoil toward the tip, the sealing wall was a downward facing surface and this surface required some hand finishing to mate the two parts

into the final assembly. In future work, alternative designs for AM should be considered in this region.

3.6 LATTICE DESIGN

3.6.1 Overview of Design

The lattice internal cooling concept has also been called matrix cooling, latticework, and vortex cooling (Bunker, 2004a; Bunker et al., 2004b). This cooling technology has reportedly been used in gas turbines manufactured in the former Soviet Union (Bunker, 2004a; Du et al., 2021). Over the last 20 years, there have been numerous studies on the lattice cooling approach. This approach had some benefits relative to the baseline designs. First, similar to the microchannel design and other double-wall cooling concepts, the coolant was forced closer to the external wall. Second, the heat transfer enhancements were greater than 2, which is comparable to turbulated serpentine channels (Bunker, 2004a; Saha et al., 2013). Finally, the matrix substructure had the potential to provide greater structural rigidity for an airfoil (Carcasci et al., 2014).

Du et al. (2021) provided a thorough review of latticework heat transfer for trailing edge cooling. Saha et al. (2013) showed that the local heat transfer coefficients in the turning regions of the lattice structure can be 5–10 times higher than the smooth wall heat transfer coefficients. This was advantageous when these turning regions were aligned with regions where large external heat transfer coefficients existed. A subchannel inclination angle of 45° was optimal (Du et al., 2021; Prajapati and Tariq, 2019). Carcasci et al. (2014) also showed that the heat transfer coefficients for most of the subchannels were uniform, excluding the turning regions. Temperature gradients were reduced by the uniform heat transfer coefficients. Additionally, the channel walls conducted heat away from the external surface like fins (Bunker, 2004a; Carcasci et al. 2014; Luan et al., 2018).

The internal cooling design chosen for this study was different from previous studies. To illustrate in the following paragraphs, the design of the traditional lattice structure will be discussed and then the variations from the traditional structure will be identified.

Lattice subchannels were formed by filling a volume within an airfoil with angled diagonal metal ribs in two layers. In the present design, the volume consisted of the entire interior of the airfoil; although, in general, this was not always the case. For example, prior studies of matrix cooling in trailing edge regions (Du et al., 2021; Saha et al. 2013) involved the bounding walls, where flow turning occurs, being placed at the airfoil tip and end-wall. The present study located the turning regions at the leading edge and the trailing edge (i.e., the regions where the external heat transfer coefficients were the highest).

A typical lattice design would have a lower layer which would extend from the airfoil lower, inner wall to the airfoil midplane. The upper layer would extend from the airfoil midplane to the upper, inner wall. Metal would not form a wall at the midplane where flow paths exist between the subchannels, rather, coolant from one channel could interact with coolant in another channel as air in the lower layer flows perpendicular to air in the upper layer. In **Error! Reference source not found.**6, an illustration is shown of a conventional lattice design considered in a prior study (Carcasci et al. 2014). For the design considered by Carcasi et al. (2014), the lattice structure spanned from the leading edge to a plane some distance from the leading edge.

It was identified at the design stage that utilizing the lattice structure across the entire airfoil led to a large variation in the subchannel passage area as each subchannel was traversed from the leading edge to the trailing edge. Since flow passages exist between the upper and lower layer, flow would preferentially short circuit the narrower flow passages in the leading and trailing edge, overcooling the mid-chord region. To resolve this design issue, an airfoil-shaped shell (scaled from the airfoil external profile) was inserted within the airfoil to generate lattice flow paths of uniform area. The lattice ribs extending into this shell were removed. Although the flow can interact with adjacent subchannels at the leading edge and trailing edge, it cannot interact with flow in non-adjacent subchannels (there is no subchannel network). Thus, the issue of flow short-circuiting the leading and trailing edge was eliminated and a lattice network was used over the entire airfoil.

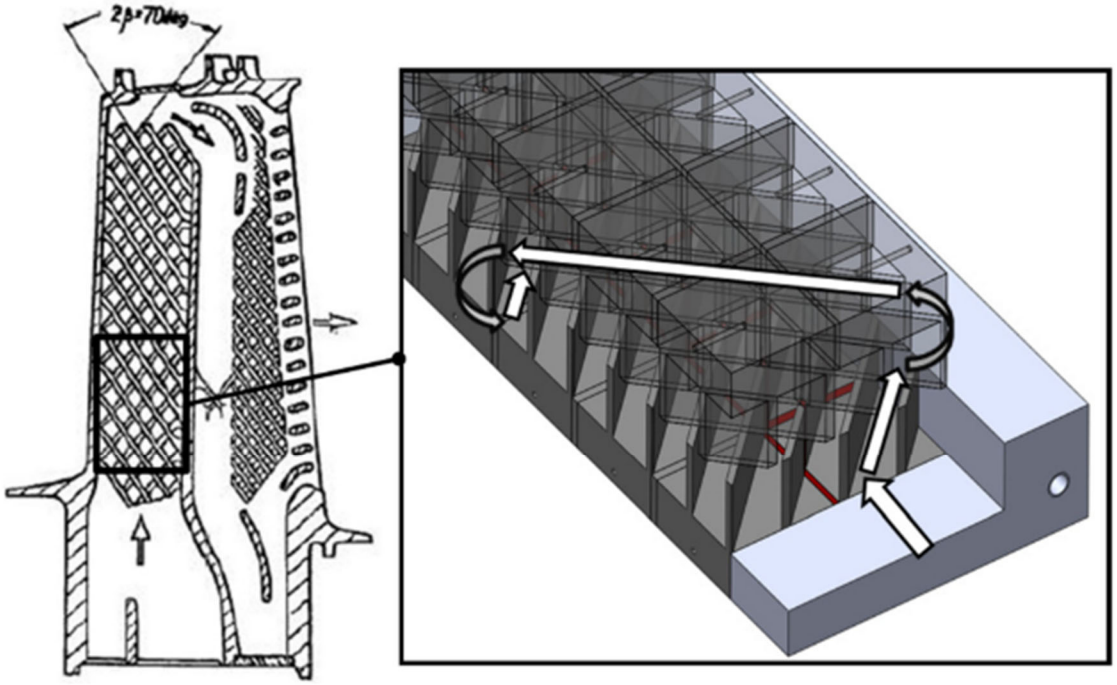

Figure 16: Conventional lattice design utilized by Carcasi et al. (2014). Adapted from prior work.

The addition of the inner airfoil shell allowed the present lattice/matrix design to achieve the design objectives: 1) keep the coolant near the exterior wall, and 2) concentrate the regions of highest internal heat transfer in the leading and trailing edge regions.

Several different CAD model views of the lattice internal cooling design are shown in Figure 17. The cooling flow entered the airfoil through 24 rectangular inlets (1.35 mm width x 1.4 mm height) as shown in Figure 17c). One-half of the cooling air flow entered the base of the air foil (i.e., top row of holes in Figure 17(c)) turned 45° and flowed toward the trailing edge. The other half of the cooling air turned 45° and flowed toward the leading edge. At the leading and trailing edge, the coolant flow impinged on the airfoil inner wall and switched from one side to the other

side of the airfoil. All the coolant exited through the tip region of the airfoil (see Figure 17b). Design parameters for this airfoil have been listed in Table 5 and the nomenclature is consistent with Carcasci et al. (2014).

Table 5: Design Parameters for Lattice Cooling Design

Design Parameter	Lattice Cooling Design
Number of flow paths	24
Flow path angle, $\boldsymbol{\beta}$	45°
Height of channel or rib, $\boldsymbol{h_{rib}}$	1.2–1.9 mm
Width of channel, $\boldsymbol{W_i}$	1.4 mm
Rib thickness, $\boldsymbol{t_{rib}}$	1 mm
External wall thickness	1.3 mm

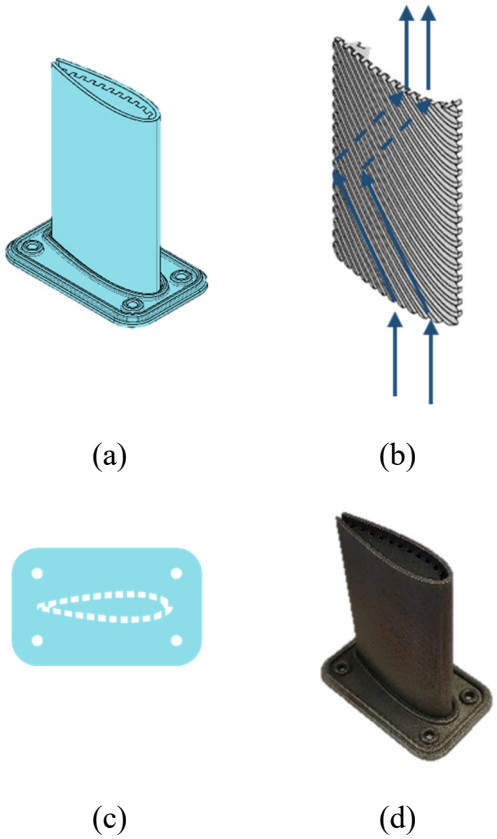

Figure 17: Lattice airfoil cooling design. a) Isometric CAD model, b) Isometric view of internal flow channels, c) Cross-section at cooling flow inlet; d) Photo of the as-built part.

3.6.2 Manufacturing Issues/Concerns

The manufacturability issues of the lattice airfoil design were minimal since the internal channel walls were oriented 45° relative to the build direction (spanwise). The channel sizes were also large which facilitated powder removal following the build.

3.6.3 Internal Cooling Correlations

The Dittus-Boelter correlation, Equation 10, was employed to calculate internal heat transfer coefficients, assuming hydrodynamically smooth channels.

$$Nu = 0.023 Re^{0.8} Pr^{0.4} \tag{10}$$

3.6.4 Simplified Cooling Model

A simplified cooling model was utilized to develop this design. The surface roughness effects were ignored and fully-developed turbulent flow was assumed through the channels. For the ribs that intersected the airfoil wall, the fin efficiencies were calculated to be greater than 90%. Estimating the cooling performance with the lattice geometry using a one-dimensional (1D) model was challenging because each cooling channel experienced a different external heat load history. One approach was to use an average external heat transfer coefficient for all channels. This simplified approach estimated that the overall effectiveness for the lattice design to be 0.43 at a HLP of 1.

3.6.5 Finite Element Model Predictions

In a second approach, a finite element model (FEM) was utilized to estimate the cooling performance. The external heat transfer coefficient profile was applied as a boundary condition on the external surface of the airfoil. The internal heat transfer coefficient was estimated using smooth channel correlations and applied as a boundary condition along the internal flow channels. It is important to note that this analysis was performed on an earlier design of the lattice blade in which coolant flow exited through the trailing edge. Thus, the results presented here were expected to be representative of the final design, although the modeling conditions were not identical.

The overall cooling effectiveness results from the FEM are shown in Figure 18. The overall cooling effectiveness ranges from 0.23 to 0.74 across the airfoil surface at a HLP of 1 (see Table 6). Higher values occurred in the mid-chord region and lower values occurred at the leading edge, trailing edge, and tip.

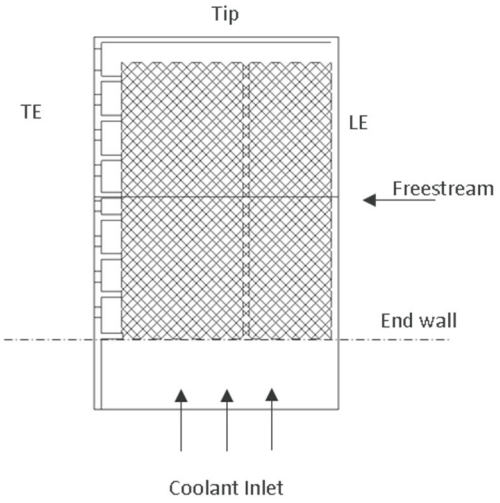

a)

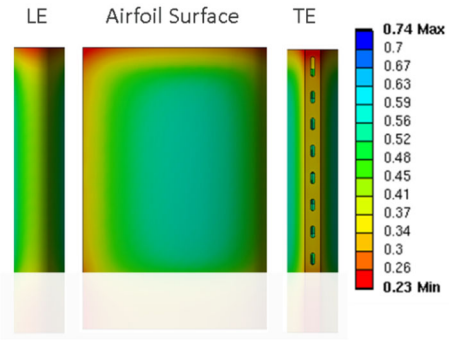

b)

Figure 18: Lattice-cooled airfoil concept 1: a) geometry and b) FEM results (overall effectiveness, ϕ).

Table 6: Predicted Cooling Performance for Lattice Cooling Design

Design Variable	Lattice Design
Overall cooling effectiveness, ϕ	0.23 min–0.74 max
Heat load parameter	1.0

3.7 MICRO-CHANNEL DESIGN

3.7.1 Overview of Design

The primary benefit of microchannel cooling was the flexibility to judiciously distribute coolant closer to the hot surface and provide more uniform cooling. Bunker (2013) concluded that microchannel cooling could reduce cooling flows by roughly 25%, while simultaneously reducing thermal stresses associated with temperature non-uniformities by 50%.

The specific design for this effort is shown in Figure 19. The cooling flow entered the microchannels at the airfoil base and flowed span-wise. A three-pass serpentine was formed as the coolant flowed from the fore to the aft sections of the airfoil. The coolant exited from the airfoil tip.

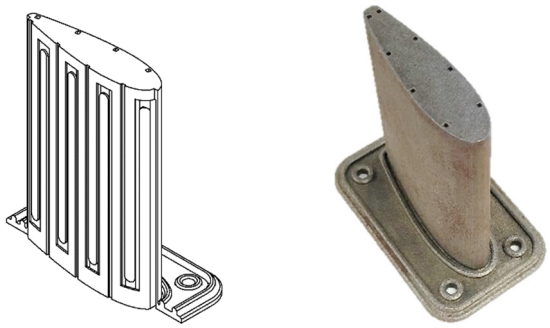

Figure 19: Microchannel design.

3.7.2 Manufacturing Issues/Concerns

The primary AM concern with the microchannel design was powder removal from the small diameter channels. Powder removal concerns were reduced by increasing the channel size. Computed tomography (CT) scans of the as-fabricated airfoils indicated that the powder was completely removed.

Other AM concerns with this design included the downward-facing surfaces in the microchannel serpentine. To address the downward-facing surfaces in the turning regions of the serpentine microchannels, 2-mm radii were incorporated into the serpentine channel design as shown in Figure 19. These radii also facilitated powder removal.

3.7.3 Internal Cooling Correlations

Although the effects of AM surface roughness are significant, the heat transfer and pressure drop correlations used in this study were based on fully-developed turbulent flow in smooth channels.

3.7.4 Performance Predictions

One design concept that was evaluated had single pass microchannels that covered the full airfoil surface. The overall cooling effectiveness and coolant temperature were calculated along the span-wise and chord-wise airfoil directions using a two-dimensional (2D) heat transfer and flow network model to generate a coarse contour of wall temperatures. In the design space, the

number of near-surface microchannels was varied from 20 to 40, and the aspect ratio for the channel was varied from 1 to 3. The channel height dimension (i.e., the dimension in the wall thickness direction) was varied from 0.5 mm to 1.3 mm. It was found that the largest channel heights required too much cooling flow to meet the performance goals and the smallest channel heights exceeded the pressure drop constraint. Increasing the number of channels reduced the pressure drop, but many of the microchannel designs were disqualified because they would not physically fit into the airfoil profile. Two single pass microchannel designs that met the design targets have been summarized in Table 7.

Table 7: Microchannel (Single-Pass) Designs that Meet Cooling Design Targets Channel

Channel Height	Aspect Ratio	No. of Channels	Δp_c	ϕ_{min}	HLP
1.0 mm	1	20	35 kPa	0.577	3.24
0.8 mm	2	20	35 kPa	0.582	3.64

As an alternative to the single-pass micro-channels, a serpentine microchannel concept was investigated to increase the internal cooling efficiency. The three-pass serpentine microchannel concept (see Figure 19) reduced the number of coolant inlets (20) and number of coolant outlets (20) to 7 inlets and 8 outlets. The total number of microchannels for the airfoil increased from 20 to 24 and the cooling flow requirement was significantly reduced. For a 35 kPa pressure drop, the single-pass microchannel concepts required 2.8 times more coolant flow and the minimum cooling effectiveness was lower. These key results have been summarized in Table 8.

Table 8: Comparison of Microchannel Single Pass to Serpentine Cooling Performance Predictions

Design Variable	Single Pass Microchannel	Serpentine Microchannel
Overall cooling effectiveness, ϕ	0.45 min–0.84 max	0.51 min–0.88 max
Heat load parameter	2.6	0.9
Internal cooling efficiency, $\eta_{c,int}$	0.15	0.50

3.8 NETL DOUBLE-WALL DESIGN

3.8.1 Overview of Design

This internally cooled airfoil design was derived from an attempt to incorporate added flexibility from a design and an analysis perspective (Straub et al., 2022). This concept divided the span into different layers that were stacked to achieve the full span height of the airfoil (see Figure 20).

The potential benefits of this design included: 1) the ability to customize internal cooling features in each section; 2) internal wall structures to provide stiffness from a structural perspective and

heat conduction paths to reduce temperature gradients in the exterior surface; and 3) a smaller modular geometry that enables other analytical tools, such as conjugate CFD modeling for each level. The design objectives for this concept were to move the cooling air close to the exterior wall and to provide separate cooling air plenums for the leading edge, the mid-chord, and the trailing edge regions of the air foil.

The coolant flow paths have been shown schematically in Figure 20d. The leading edge (LE, below) was cooled using five impingement jets, but the holes were large relative to the baseline designs. Rib turbulators in the leading edge alternated from the "ceiling", or from the "floor", of the flow channel, and partially shielded each impingement jet from crossflow effects. The spent leading-edge coolant flowed toward the core of the airfoil. Fresh mid-chord coolant was supplied through two small tear-drop shaped plenums. This coolant flowed through a short serpentine path before being injected toward the trailing edge (TE, below). The spent leading-edge and the spent mid-chord coolant streams were mixed with fresh trailing-edge coolant and exited through racetrack holes in the trailing edge.

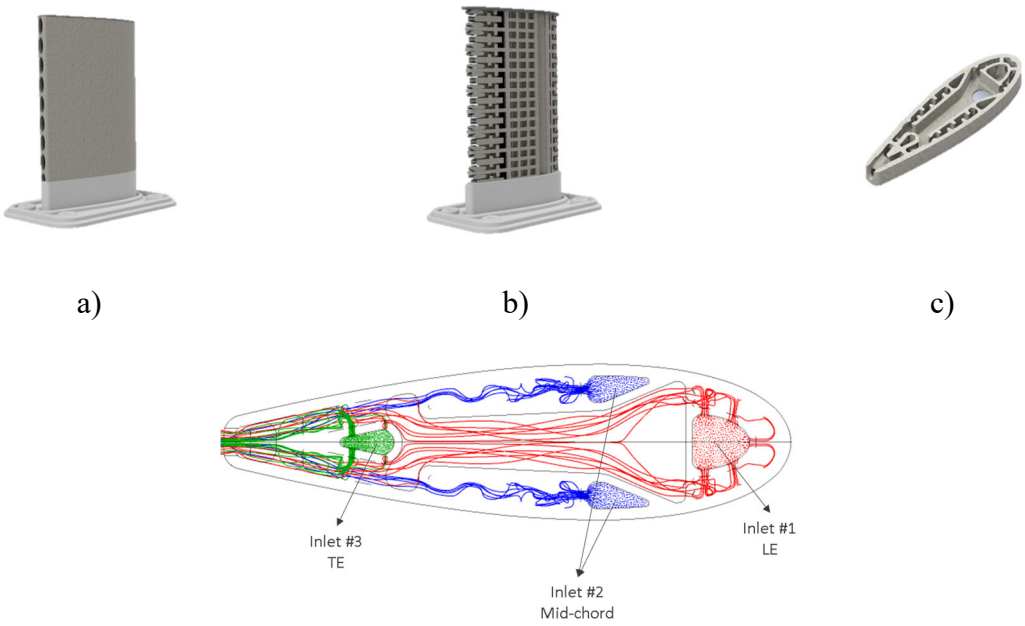

Figure 20: NETL stacked double-wall internal cooling design concept: a) trailing edge exit slots; b) CAD model with external surface removed; c) single span-wise section with internal cooling features; d) cooling air flow diagram. Adapted from Straub et al. (2022).

3.8.2 Manufacturing Issues/Concerns

This cooling concept had numerous downward-facing surfaces and powder removal issues had to be addressed. All the cooling holes in this design were elliptical and radii were incorporated into all the horizontal interfaces. A 3.8-mm hole was incorporated into the design to remove the

powder from these interior channels. This powder removal hole was located in a stagnant region between the leading-edge and mid-chord regions. After fabrication, this powder removal hole was plugged to prevent cooling air flow through this internal passage during testing.

3.8.3 Cooling Model Used to Predict Performance

A conjugate 3D CFD modeling approach was used to estimate the cooling performance for this stacked double-wall concept. The numerical model for the initial screening consisted of one half of a single span-wise section with internal features as shown in Figure 20c. The coolant mass flow rates were determined by assuming a uniform pressure drop across various segments of the design. The boundary conditions for the steady-state Reynolds Averaged Navier-Stokes (RANS) simulations were obtained from the test rig operating conditions.

Initial screening of the designs provided additional insight into the coolant flow patterns. Design recommendations such as reducing the leading edge and trailing edge impingement hole diameters to reduce recirculation zones and adding ribs to the mid-chord passage were incorporated into the design. The final design, prior to addressing manufacturing constraints, was simulated using a transitional shear stress transport (SST) k-ω model, and those results have been summarized in Table 9.

Table 9: Predicted Cooling Performance

Cooling Design	Overall Cooling Effectiveness (Average/Range)	Heat Load Parameter
Baseline vane	$\bar{\bar{\phi}}$ = 0.43 [0.35,0.64]	1.0
Microchannel	$\bar{\bar{\phi}}$ = 0.73 [0.51,0.84]	0.9
NETL double-wall	$\bar{\bar{\phi}}$ = 0.61 [0.50,0.64]	1.0

3.8.4 Rotational Stress Model and Analysis

A comparative stress analysis was completed to address some mechanical stresses concerns associated with the surfaces parallel to the airfoil tip. A radial G-force loading of 80,000 times the gravitational force equivalent was applied to the mass of the NETL double-wall design and the baseline blade. The double-wall design was 5–10% lighter than the baseline blade. As expected, the Von Mises stresses were highest in the lower regions of both airfoils. The round holes in the baseline blade design were generating higher stress concentrations than the oval shaped holes in the double-wall design. The stresses in the "floor" regions of the double-wall design were in the 10–15 ksi range, which was significantly less than other regions. Several options were identified to reduce the stresses in these lower regions of the airfoil, but these options were not further investigated after this comparative analysis. In summary, compared to the baseline blade, the stress levels due to a radial loading of 80,000 times the gravitational equivalent were slightly lower for the double-wall design (see Figure 21).

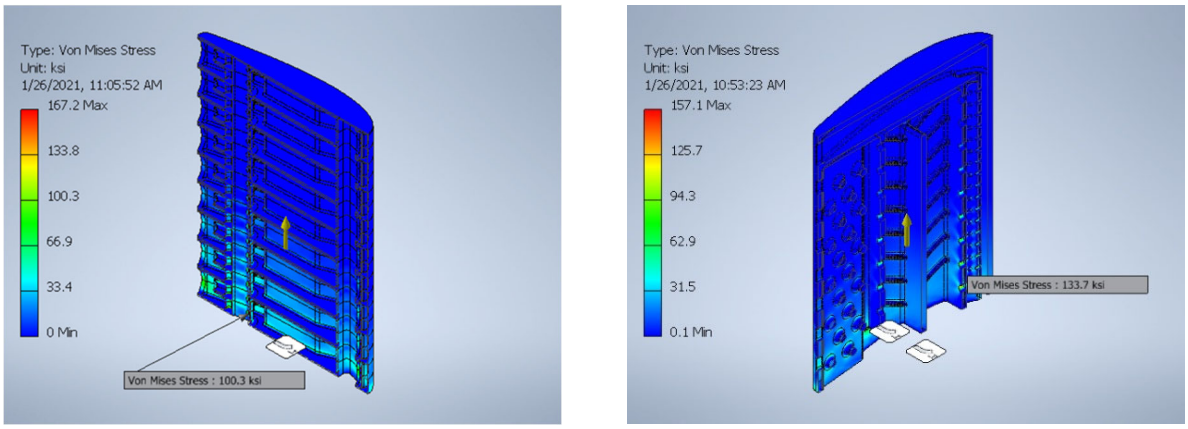

(a) (b)

Figure 21: Comparative stress analysis of the NETL stacked double-wall and the baseline blade. Adapted from Straub et al. (2022).

3.9 INCREMENTAL IMPINGEMENT DESIGN

3.9.1 Overview of Design

Incremental impingement cooling design is a high-solidity, double-wall internal cooling method which was developed under the U.S. DOE's University Turbine Systems Research (UTSR) program. This concept was designed to cool regions around an airfoil leading edge and pressure surface. This approach was designed to avoid the use of leading edge film cooling which had the potential to clog when subjected to environments with particulates. This method maintained a high-level of internal cooling by extending surfaces with the double-wall, high-solidity pedestal arrays, while maintaining a reasonable coolant to surface temperature difference. In this cooling method, cooling air was introduced into the array through impingement holes that were integrated into the downstream portion of the pedestals. By injecting coolant into the wake region downstream of the pedestals, the impingement jets were able to impinge on the inside surface of the external wall without being adversely impacted by the high crossflow velocities through the cooling passage. Additionally, the incremental addition of cooling air helped manage the surface to coolant temperature difference, and the pressure drop was significantly reduced relative to a pin array since only a fraction of the coolant flows through all the entire pin array. The overall internal heat transfer coefficient was similar to a high-solidity pin-fin array, but the surface to coolant temperature difference was more controllable. The high-solidity pedestals also provided a conduction path to minimize local temperature gradients from impingement cooling that were observed in other designs such as the baseline vane.

Since the incremental impingement concept was never designed to cool an entire turbine airfoil surface, the method was applied in two sequential but independently sourced segments. In the fore section of the airfoil, the spent coolant was collected after passing through eight rows of pedestals. This fore coolant was discharged through the airfoil tip in the form of a slot. The high-solidity pedestals and double-wall configuration provided the structural integrity required for a

discharge slot. The aft section of the airfoil had a separate coolant inlet plenum and the coolant from this section was collected near the trailing edge and ejected through the trailing edge using elliptical “racetrack” shaped exit holes. Figure 22 shows a 3D printed cut-away section of the incremental impingement airfoil design. This partial model was printed to better understand the difficulties in generated this complicated geometry using AM.

Figure 22: Partial AM print of the incremental impingement geometry showing base, pedestals, cold-side impingement holes, and central plenum.

3.9.2 Manufacturing Issues/Concerns

In the development of the incremental impingement airfoil design, the pedestals were oriented 90 degrees to the build direction; therefore, even though the channel height dimensions were small (1 mm and 0.75 mm), these pins needed some chamfers to increase the probability of a successful build. Although these chamfers could be small, due to the small channel size, the potential blockage was a concern from a pressure drop and heat transfer perspective. To address the trade-off between manufacturability and thermal performance, some test coupons were developed to investigate the quality of the pedestal-chamfer combinations prior to printing the final airfoil.

The thin test coupons were designed for analysis. Two different channel heights (0.75 mm and 1.0 mm) were designed. The pedestals were arranged in pairs. The two pedestals in the far right

of Figure 23 was the original design with no chamfer. The pin diameters and the chamfer dimensions were varied to maintain the same overall area blockage as the original design. Figure 23 also shows photographs of the as-printed parts. For the 1arger channel height, more variation was observed in the original pedestal design (far-right pair of pedestals). The design team ultimately decided to proceed with the middle design which was only 0.25 mm (0.010 in.) smaller than the original pedestal diameter.

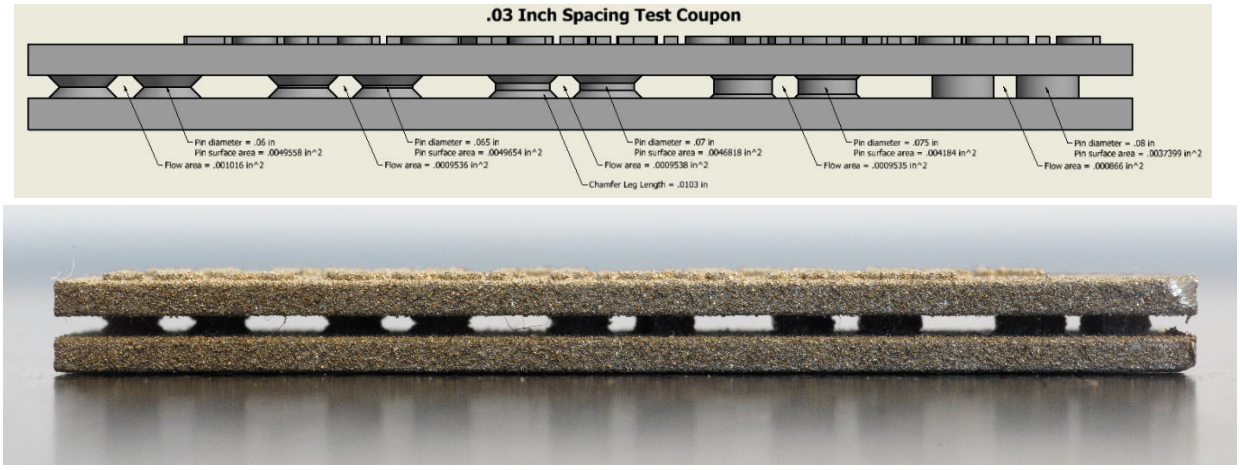

(a)

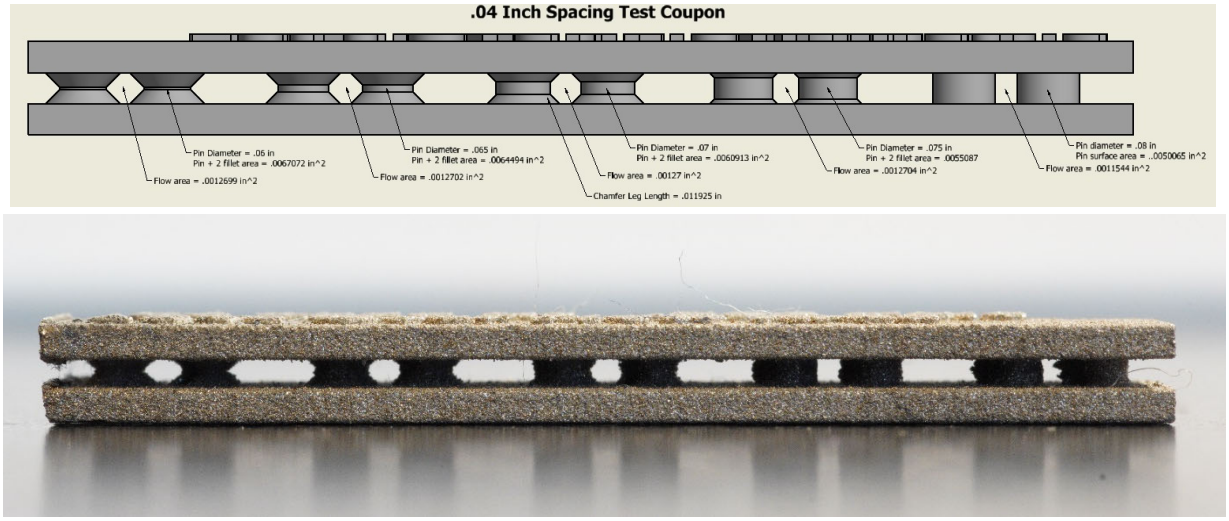

(b)

Figure 23: Coolant passage test coupon with pedestal and chamfer combinations that maintain same flow blockage (a) 0.75 mm coolant channel height, and (b) 1.0 mm channel height.

No modifications were made to the shape of the cooling jet holes that lead from the plenum to the outer cooling channels. Modifications to these holes were inhibited by their location which was partially embedded inside the pedestals. Due to this placement, extensive rework of the design would have been needed to substitute elliptical holes for the originally designed round holes. A confocal microscope image of the 0.9 mm (0.035 in.) diameter hole is presented in

Figure 24. The build direction in this figure was right-to-left, so the flattened region of the hole was a downward-facing surface. The printed test coupon also showed some very abrupt (high surface angle) roughness elements inside the internal passages.

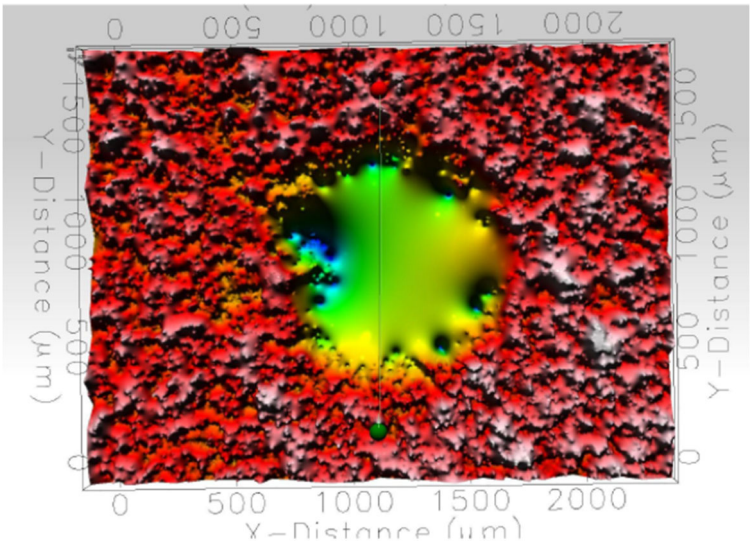

Figure 24: Confocal microscope image of 0.035-in. hole for AM incremental impingement coupon.

3.9.3 Internal Cooling Correlations

The incremental impingement technique can provide a high level of internal cooling without film cooling holes. As part of previous DOE/UTSR project, heat transfer and pressure drop correlations for incremental impingement were developed for models with standard configurations and models with variable hole sizes. In the current NETL airfoil heat transfer study, Configuration 1 from Busche et al. (2013) was applied to: 1) the leading edge and mid-chord section, and 2) the trailing edge section of the airfoil.

The original high-solidity pin-fin research (Jaswal and Ames, 2009) had a pin height to diameter ratio (H/D) of 0.95, while the incremental impingement pedestals used in subsequent studies, including this study, had an H/D of 0.5. A comparison was made in Figure 25 showing the previous correlation for high-solidity pin arrays with H/D of 0.95 (solid line) compared to the lower profile high-solidity array (diamond symbols) and the first row of impingement data (round symbols). The lower profile impingement array increased the average Nusselt Number and had a higher Reynolds number dependence than the higher profile array. This dependence was consistent with higher percentage of endwall surface area (55%) in the low profile array compared with the higher profile array (39%). Generally, endwall surfaces have a higher Reynolds number dependence compared with pins.

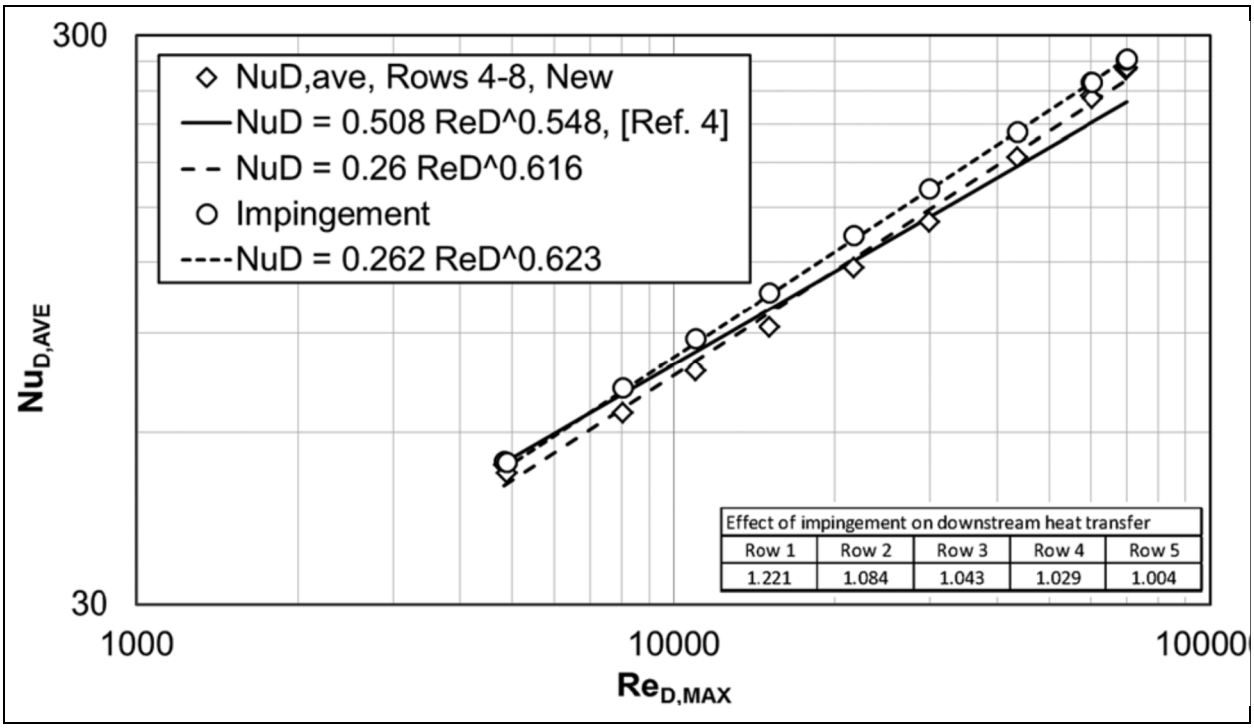

Figure 25: Baseline array averaged Nusselt number vs. diameter Reynolds number based on V_{MAX}, includes impingement row and Busche et al. (2013) data for comparison (Jaswal and Ames, 2009).

Figure 26 shows a heat transfer comparison (Nusselt number vs. Reynolds number) between Configurations 1 and 2 of the incremental impingement and the low-profile high-solidity pedestal array. Clearly, the heat transfer levels of the three arrays were very similar. In these previous studies, the Reynolds number based on V_{MAX} ranged from around 5,000 to 75,000. V_{MAX} was the velocity resulting from the entire flow going through the minimum area of adjacent pedestals in a row.

The previous DOE/UTSR study documented the local Nusselt number enhancement (Nu_D/Nu_0) for each row of pedestals. These local heat transfer data were used in the heat transfer model for the current effort. Additionally, this NETL airfoil design used one additional pedestal row compared with the UTSR study. This extra row was accounted for using the baseline array correlation, $Nu_D = 0.26\ Re_D^{0.616}$. This correlation was based on measurements with air as the coolant and should be consistent with the NETL-cooled airfoil testing.

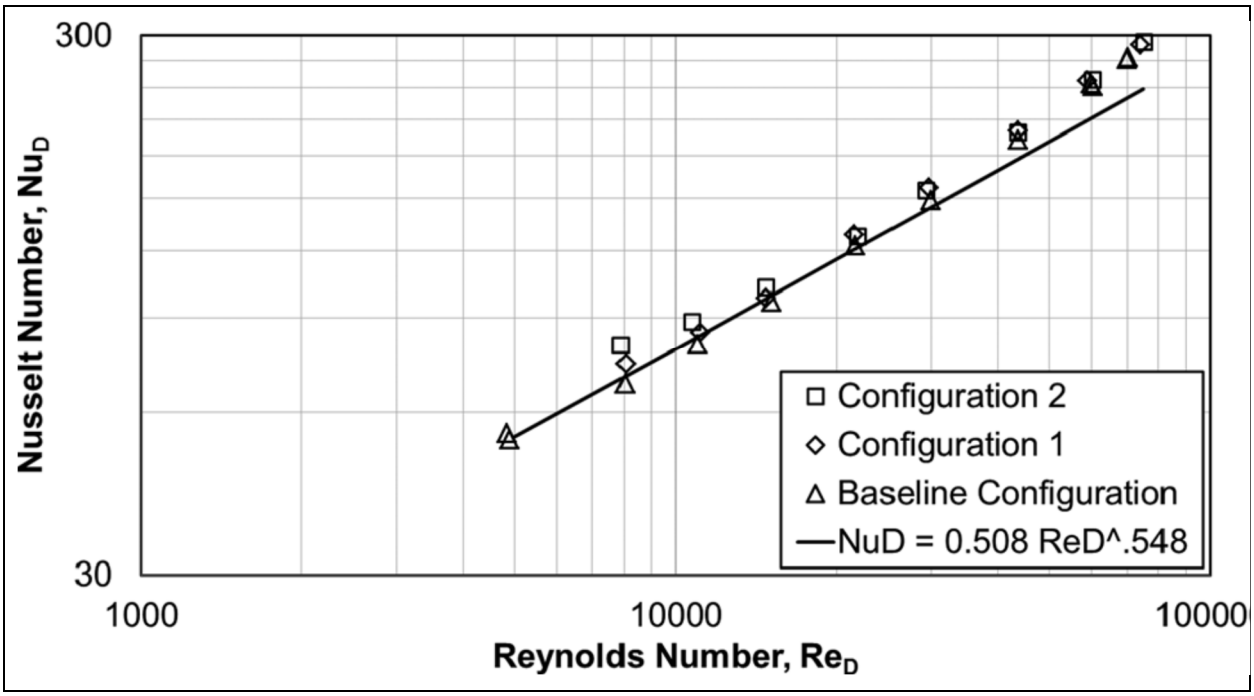

Figure 26: Comparison of area-averaged Nusselt number as a function of Reynolds number comparing the high-solidity pin-fin array with Configurations 1 and 2 (from Jaswal and Ames, 2009).

The pressure drop across an internal cooling array was critical information to the overall heat transfer design. Figure 27 presents the low-profile, high-solidity pin-fin array in comparison with the flow friction factor correlation from reference (Jaswal and Ames, 2009). This comparison indicated that the present high-solidity pin-fin array pressure drop was consistent with previous results. This flow friction factor, f, was defined as:

$$f = \frac{\Delta P}{2N_{row}\rho V_{MAX}^2}$$

The pressure drop across the incremental impingement array was more difficult to define compared with a standard pin-fin array. The incremental impingement array included an initial row of impingement holes which required a pressure drop to feed coolant into the array. Figure 28 compares the dimensionless pressure drop of the two incremental impingement arrays (low aspect ratio) with the high-solidity pin-fin array (high aspect ratio). This pressure drop included the pressure drop across the impingement array, which added to the overall pressure drop of each array. The incremental impingement arrays show a reduced pressure drop compared to the pin-fin array, which could allow up to a 24% increase in flow with the same pressure drop. The previous DOE/UTSR project documented this pressure drop data which was used in this project to estimate the pressure drop for the incremental impingement geometry assuming a smooth channel over a range of normal engine cooling flow conditions.

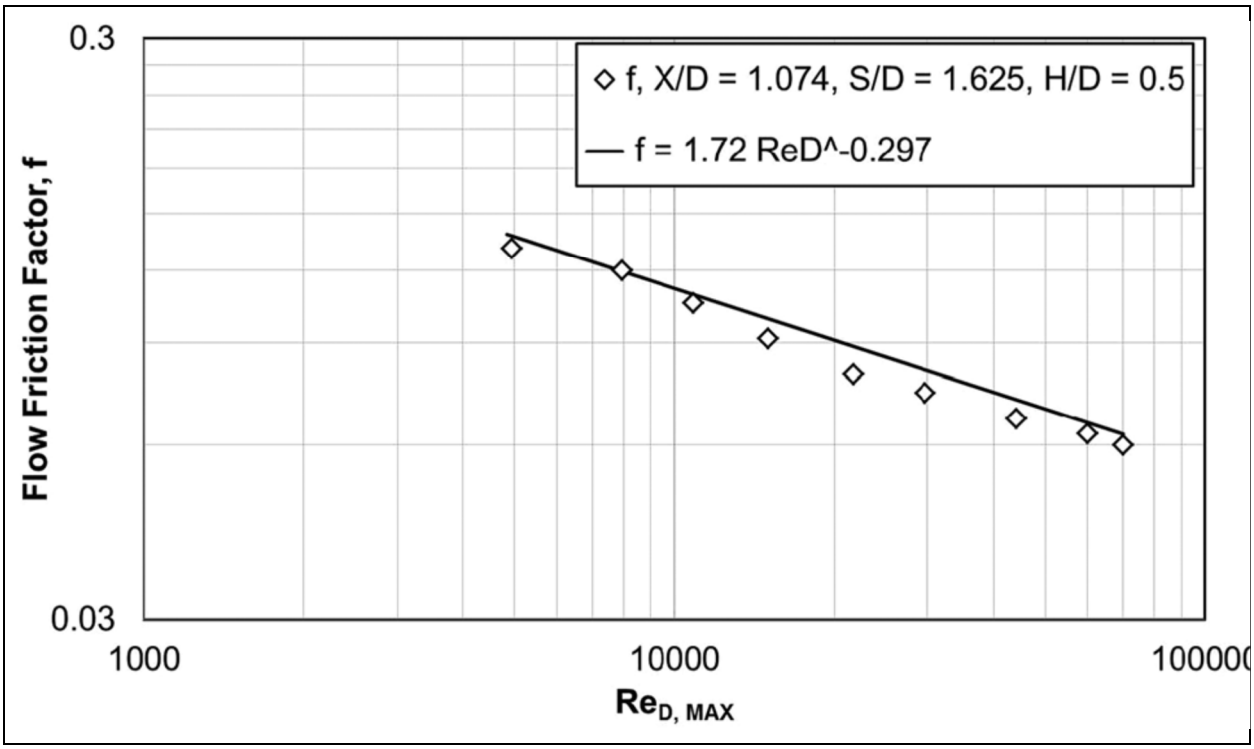

Figure 27: Flow friction factor comparing correlation from Busche et al. (2013) with present baseline configuration data (from Jaswal and Ames, 2009).

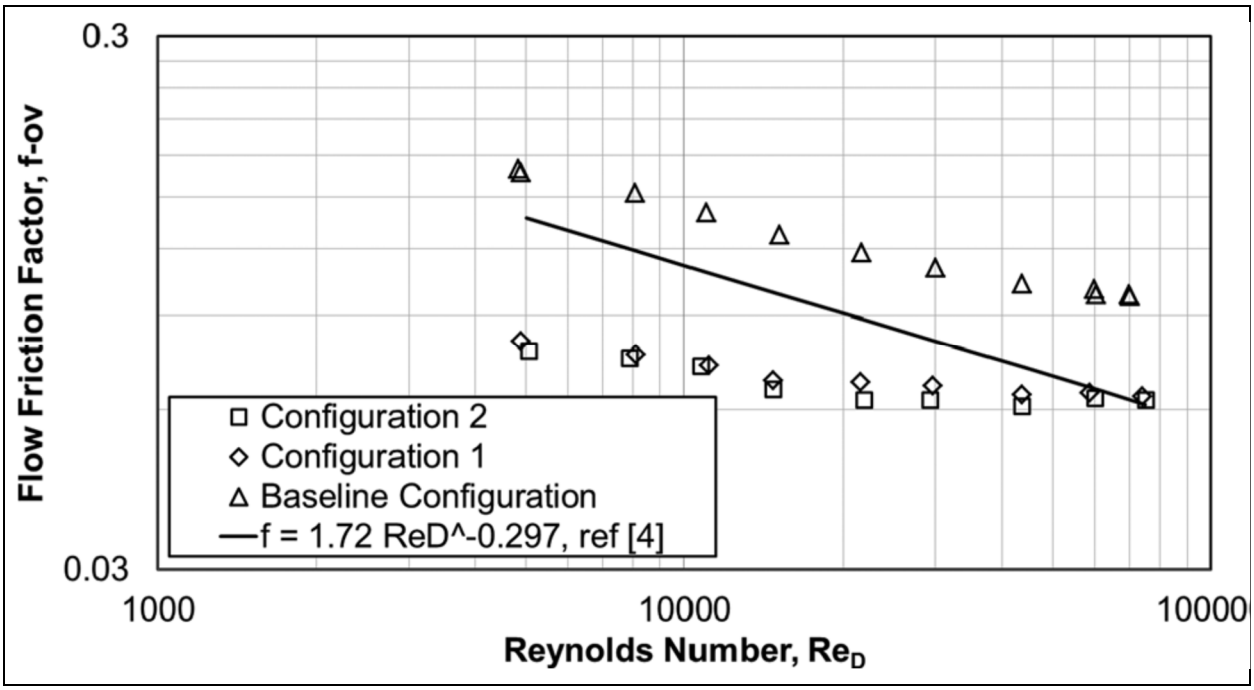

Figure 28: Overall pressure drop parameter for baseline and two leading edge cooling configurations as a function of Reynolds number (from Jaswal and Ames, 2009).

3.9.4 Cooling Model Used to Predict Performance

A 2D finite difference model of the incremental impingement-cooled airfoil was generated to support the testing of this airfoil and guide the solid model of the cooling configuration. This model helped support ideas to improve the geometry of the model for printing. A high heat load was predicted in the leading edge region, while a lower heat load was predicted over the laminar region of the airfoil prior to transition past mid-chord (see Section 3.2). Downstream of the transition, turbulent flow with moderate and relatively uniform heat load was predicted over the trailing edge region of the model.

A 2D mathematical representation of the incremental impingement airfoil is shown in Figure 28. The leading-edge region has a row of closely spaced impingement holes between lobes aligned with the external stagnation line. In Figure 29, the locations of the impingement jets are shown with the arrows. These jets were located on the downstream side of the pins in every other row. This configuration had nine rows of pedestals and four of the rows had impingement jets behind every other pin. Downstream from the last row of pins, the flow discharged into a plenum region in the center of the airfoil. The spent coolant from the discharge plenum was redirected toward a discharge slot at the tip of the airfoil. The upstream cooling passage had a passage height of 0.040 in.

The incremental cooling array in the aft-region began just downstream of the discharge plenum for the fore-region. The downstream array was very similar to the upstream, but the passage height was smaller (i.e., 0.030 in. passage height). This height was judged adequate, due to the reduced and more uniform cooling load in the aft-region of the airfoil.

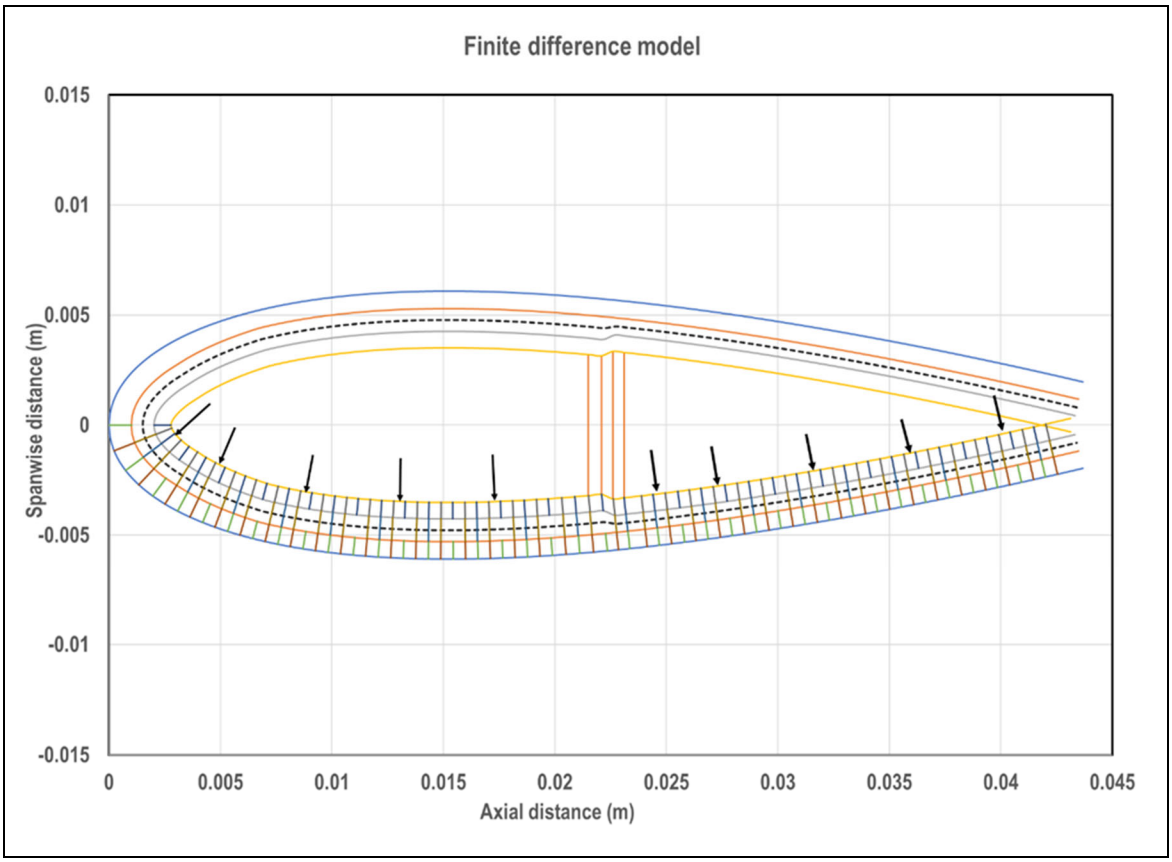

Figure 29: Schematic of finite difference representation of proposed incremental impingement model.

The analytical results of the complete finite difference analysis are shown in Figure 30. The dark blue line at the top of the figure represents the hot gas temperature of 650 K. The light blue line at the bottom of the figure represents the coolant inlet temperature of 332 K. The red and orange lines in the middle of the figure represent the outer and inner wall temperatures for the double-wall design, respectively. The blue symbols represent the cooling air temperatures within the cooling passage. Generally, the wall temperatures were highest near the leading edge of the airfoil where the external heat transfer coefficients were the highest. The wall temperatures were the lowest in the middle of the airfoil before transition. The temperatures in the aft-region of the airfoil were relatively uniform and showed a good level of cooling.

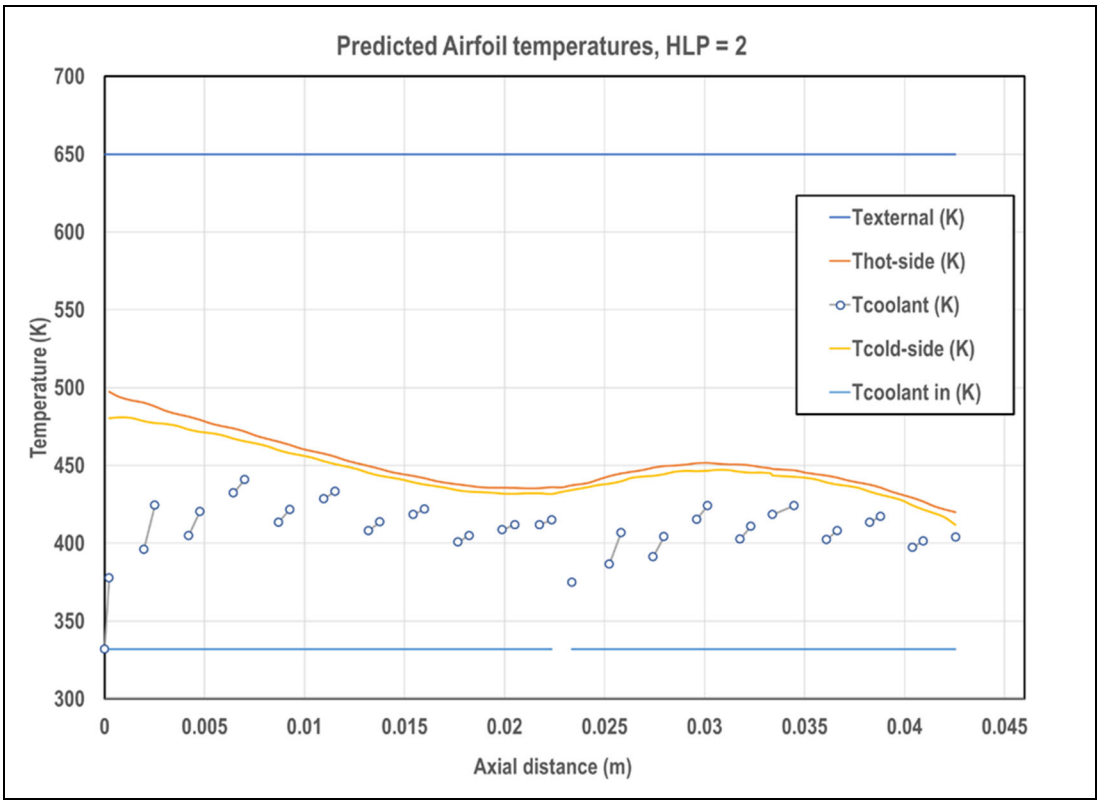

Figure 30: Plot of external gas, airfoil wall, cold-side wall, internal coolant, and inlet coolant temperatures along the airfoil cooling model for incremental impingement, HLP = 2.

Figure 31 shows the predicted overall effectiveness distributions for this design at an HLP of 2. The effectiveness level around the leading edge was lowest at a level of 0.48. At mid-chord the effectiveness levels reached a peak of nearly 0.72, while in the back portion of the airfoil the predicted effectiveness ranged from 0.62 to 0.72.

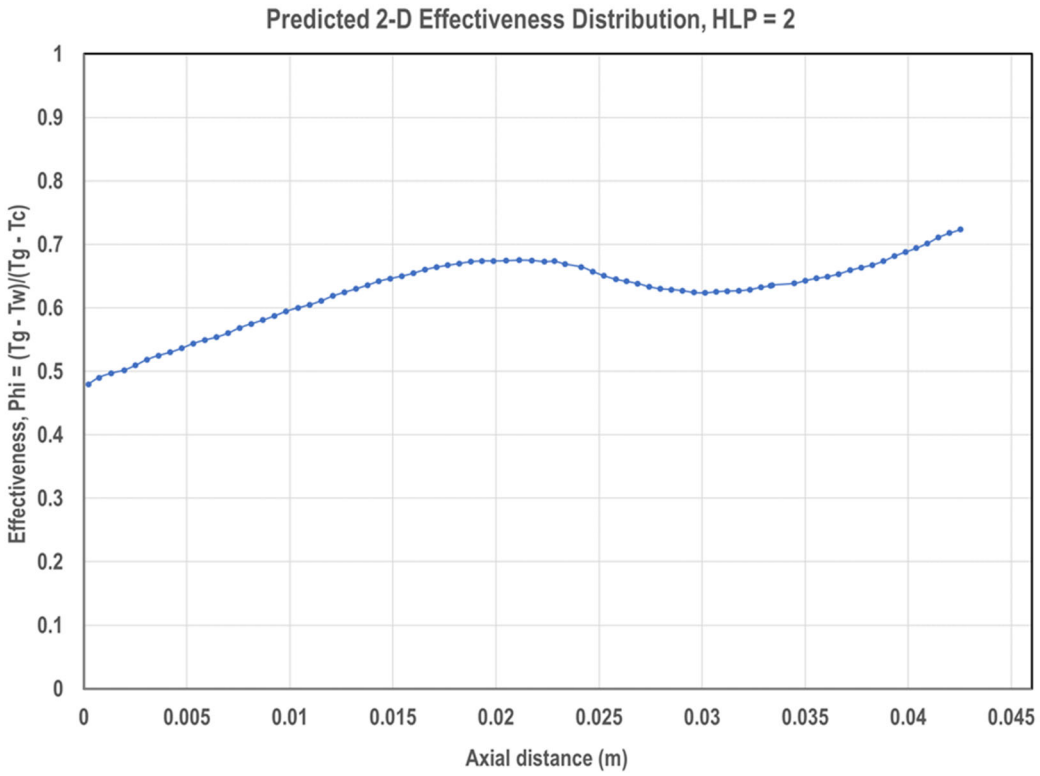

Figure 31: Predicted overall effectiveness distribution for incrementally cooled airfoil for HLP = 2.0.

Figure 32 presents the predicted average effectiveness for the incremental impingement-cooled airfoil with the HLP ranging from 2 to 4. Over this range the average predicted effectiveness levels ranges from 0.62 to 0.72. These data and similar data for predicted pressure drop will be compared to experimental results. These comparisons will provide confidence in the ability to apply the internal cooling correlations for incremental impingement for the purpose of internally cooling turbine airfoils.

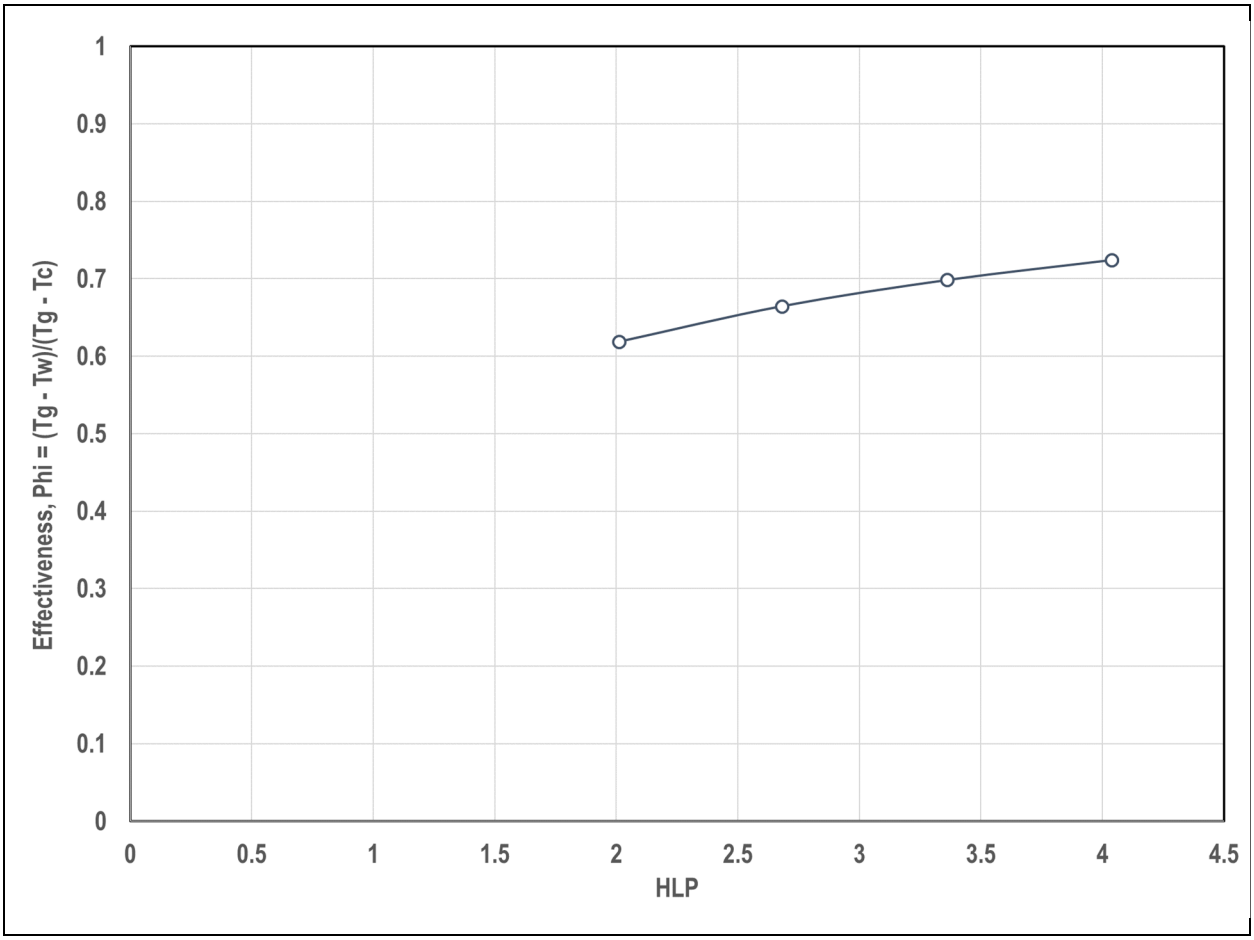

Figure 32: Predicted airfoil average effectiveness as a function of HLP.

4. EXPERIMENTAL AIRFOIL COOLING PERFORMANCE

Internal convective cooling has played an important role in cooling turbine airfoils and has progressed from simple radial cooling channels to complex geometrical patterns with heat transfer enhancement features. Rib turbulators, pin-fins, and impingement jets have been among the most widely used internal cooling mechanisms that provide higher heat transfer augmentation. The major objective of this study was to increase the internal cooling efficiency which could have a significant impact on gas turbine and CHP system performance. These potential benefits have been described in Section 2.4 (Figure 8 and Figure 9).

4.1 EXPERIMENTAL APPROACH

The approach to measure the cooling performance for the different airfoil cooling designs was based on a concept called cooling technology maps. Cooling technology maps are a graphical representation of the relationship between a non-dimensional cooling parameter (i.e., HLP) and a non-dimensional surface temperature (i.e., overall cooling effectiveness). The overall cooling effectiveness is a non-dimensional ratio of the temperature difference between mainstream hot gas temperature and the external wall temperature to the coolant temperature difference (Equation 11). The HLP represents the ratio of overall coolant heat capacity (heat load absorbed) to external heat flux imposed as shown in Equation 12. As previously described, the internal cooling efficiency (Equation 13) is a parameter often referenced in the gas turbine cooling literature, but experimentally measured values have not been previously reported. In this project, the internal cooling efficiency curves have been measured, in addition to the overall cooling effectiveness.

$$\phi = \frac{T_g - T_{w,ext}}{T_g - T_{c,in}} \tag{11}$$

$$HLP = \frac{\dot{m}_c c_p}{h_{ext} A_{ext}} \tag{12}$$

$$\eta_c = \frac{T_{c,out} - T_{c,in}}{T_w - T_{c,in}} \tag{13}$$

$$\eta_c = \frac{\phi_{avg}}{HLP(1 - \phi_{avg})} \tag{14}$$

4.1.1 Cooling Technology Maps

The turbine airfoil design methodology as outlined by Bunker (2006, 2017) was followed in the present effort. As described by Bunker and others (Holland and Thake, 1980; Cunha, 2006; Downs and Landis, 2009), cooling "technology maps" were used to compare different cooling designs on a common basis.

Using technology maps, Cunha (2006) suggested that a maximum cooling effectiveness of approximately 0.6 can be achieved without film cooling using multi-pass serpentine passage with rib turbulators. Downs and Landis (2009) also used technology maps, or technology curves, to

describe a practical limit of approximately 0.8 for overall cooling effectiveness using film cooling and ideal internal cooling at an HLP of 6.0. The technology curves for an integrated cooling approach consisting of impingement, pin-fin, and film cooling was first illustrated by Nakamata et al. (2007). In this experimental study, the overall cooling effectivenss reached a maximum of 0.8 at an HLP around 10. This result was consistent with the claims of Downs and Landis (2009). Bergholz (2008) published a modeling study on a preliminary impingement-cooled airfoil design showing an overall effectiveness up to 0.7 at an HLP of 4.0. None of these prior efforts presented both overall cooling effectiveness and internal cooling efficiency curves for an integrated (entire airfoil) cooling architecture.

4.2 DESCRIPTION OF TEST FACILITY

To assess the cooling performance for each of the AM airfoils described in this project, an existing conjugate heat transfer test facility at NETL was used (Ramesh et al., 2021). A schematic of the test facility is shown in Figure 33. The test facility was connected to a compressor capable of delivering a maximum of 1 kg/s of mass flow rate on the free stream side and a gas heater that increased the mainstream temperature to 650 K at atmospheric pressure conditions. The hot gas flow was conditioned to provide a uniform velocity and temperature profile to the 100 mm x 100 mm test section. The test section was equipped with potential optical access on three walls. The fourth wall supported the internally cooled airfoil. Cooling air was supplied to an inlet plenum (roughly 145-mm diameter) prior to entering the base of the airfoil. The spent coolant mixed with the hot gas stream downstream of the airfoil.

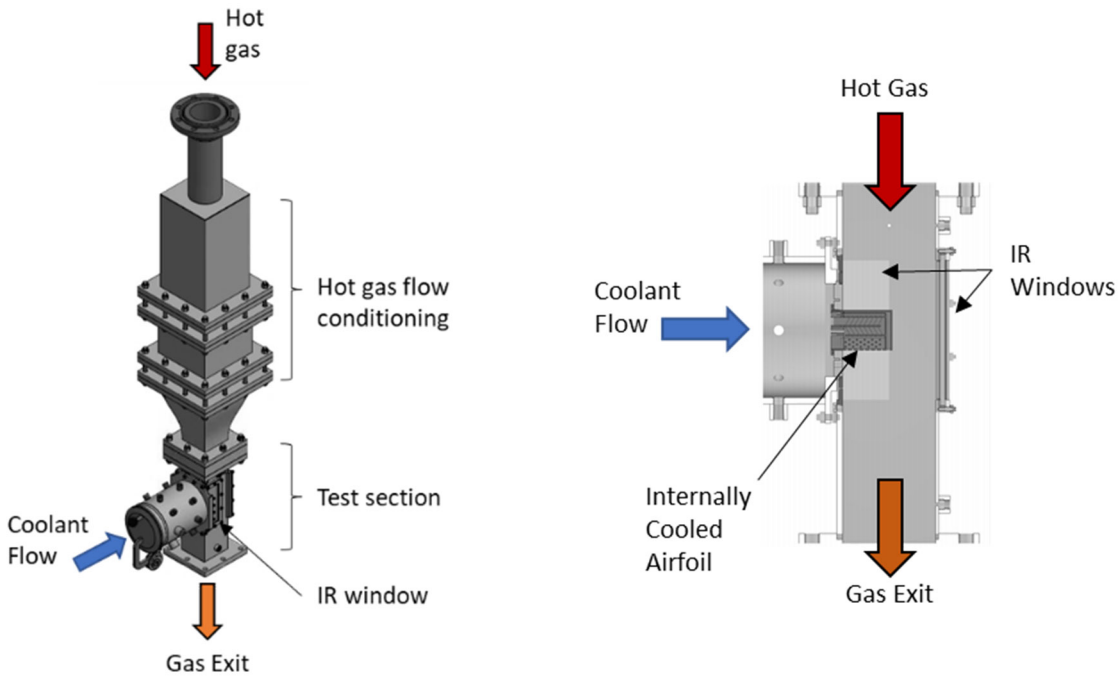

Figure 33: Schematic of conjugate heat transfer test facility: a) CAD model of test rig, b) cross-section of the test section comprised of plenum, airfoil, and hot gas path channel.

4.2.1 Dependent and Independent Variables

The dependent variable in this test included the external airfoil surface temperature and the overall cooling effectiveness, ϕ, as defined in Equation 11. The external wall temperature of the airfoil was measured using an infrared camera (FLIR Model A8300sc). Four coats of Krylon HighHeat Max paint were applied to the external airfoil surfaces. The FLIR camera was bench calibrated using a blackbody source and more details on the IR temperature measurements can be found in Section 4.3.

In some cases, the coolant outlet temperature was also measured to characterize the internal cooling efficiency. This outlet temperature was measured using a thermocouple rake and a translation stage to measure the temperature profile of the coolant leaving the trailing edge of the airfoil. These measurements will also be described in Section 4.5.

The independent variable in this experiment was the coolant flow rate. The coolant flow was controlled by a mass flow controller. As described previously, the non-dimensional parameter for the coolant flow rate was called the HLP (Equation 12). The minimum HLP that could be achieved at these test conditions was approximately 0.5 and the maximum coolant flow rate was limited by the pressure drop across the airfoil cooling passages. The maximum coolant flow rate varied depending on the airfoil cooling design and the inherent friction losses of the design. The second independent variable in this experimental test was the airfoil cooling design. These designs have been described in Section 3.

The variables that were controlled as constants included the hot air flow rate (0.64 kg/s), the hot air temperature (650 K), and the coolant inlet temperature (325 K). The hot gas flow rate was controlled using a high-temperature flow valve and an orifice meter. The coolant temperature was controlled using a small electric heater. Data were taken during steady-state intervals of 10–20 min for each test condition. The temperatures, pressures, and flow rate data were stored every second.

4.3 IR CAMERA DETAILS

The airfoil surface temperatures were estimated via IR thermography. A FLIR A8300sc IF camera was used to record images of the airfoils during tests in the NETL Conjugate Aerothermal Test (CAT) Rig. The CAT lab possesses two FLIR A8300sc cameras: S/N 00036 and S/N 00073. Both cameras operate in the 3–5 micron wavelength band. Camera S/N 00036 was employed in these tests. Raw intensity signals from the camera were acquired with FLIR Research IR software and were post-processed to estimate surface temperatures.

The rig into which the airfoils were mounted contains several openings for potential visual and/or optical access (Figure 34). These openings can be fitted with blank steel plates, quartz windows, or sapphire windows. For these tests, the 6-in. by 2-in. opening indicated in Figure 34 as “airfoil view” was fitted with a sapphire window, which has much higher transmission of IR radiation compared to quartz. The 6-in. by 4-in. opening “above” the airfoil was fitted with a sapphire window, unless the experiments included pitot tube and thermocouple traverses. For cases with traverses, it was fitted with a metal blank. The 6-in. by 2-in. opening “behind” the airfoil was covered with a metal blank. The outer surfaces of the airfoils and all the interior metal surfaces within the CAT test section were coated with multiple layers of a high-emissivity high-temperature paint (Krylon High Heat Max) to provide a consistent environment with respect to infrared emission and reflection.

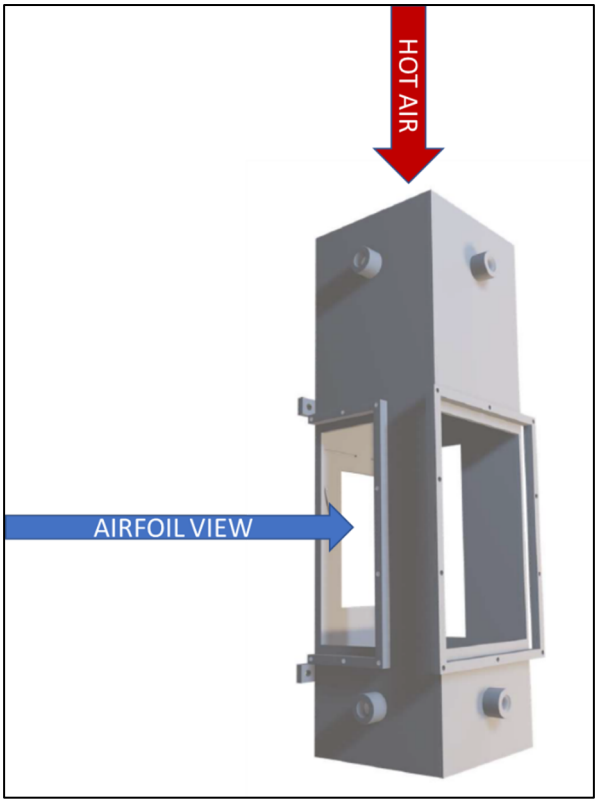

Figure 34: Schematic of CAT test section.

4.3.1 Calibration of IR Camera

The procedure used to calculate the temperature for each pixel in the airfoil images required calibration. This calibration was performed in two stages: 1) a "blackbody" calibration which established the basic temperature-intensity relationship for an unobstructed line-of-sight between the camera and an "ideal" blackbody; and 2) an in-situ calibration which compensated for factors like emissivity, reflected emissions, transmissivity, and ambient IR levels.

The wavelength-specific intensity of IR radiation emitted from an ideal blackbody is a function of temperature and is described by Planck's Equation (Equation 15):

$$I_{bb}(T_{body}) = \frac{C_1}{\lambda^5 \left[exp\left(\frac{C_2}{\lambda T_{body}}\right) - 1 \right]} \tag{15}$$

where:

$I_{bb}(T_{body})$ is the intensity (W/steradian micron),

λ is the wavelength (micron),

T_{body} is the temperature of the blackbody (K),

$C_1 = 3.742 \times 10^8 W \cdot \mu m^4/m^2$, and

$C_2 = 1.438 \times 10^4 \mu m \cdot K$.

The raw output from the IR camera, as an instrument to measure infrared intensity over a narrow band of 3–5 micron, was a function of temperature and was assumed to be linear with respect to the Planck's Equation, i.e.,

$$K_{out}(T_{body}) = aI_{bb}(T_{body}) + b = \frac{aC_1}{{\lambda_{cam}}^5\left[exp\left(\frac{C_2}{\lambda_{cam}T_{body}}\right) - 1\right]} + b = \frac{K_1}{\left[exp\left(\frac{K_2}{T_{body}}\right) - 1\right]} + K_0 \quad (16)$$

where:

$K_{out}(T_{body})$ is the camera output (digital counts),

a is the slope (counts/ W/steradian micron),

b is an offset or "intercept" (counts),

λ_{cam} is an "effective" or average wavelength for the camera response (microns)

$K_1 = {a \cdot C_1}/{\lambda_{cam}^5}$,

$K_2 = \frac{C_2}{\lambda_{cam}}$, and

$K_0 = b$.

The IR camera output was modeled in terms of K_0, K_1, and K_2, which were unknowns. These quantities were estimated through a blackbody calibration process. It was important to address some issues with K_0, such as with the camera used in these tests K_0 seemed to change throughout the test duration and K_0 was akin to "dark current". It was a non-zero output that would be present even if the camera were focused on an object with a temperature of absolute zero. When the camera was focused on a steady, well-characterized source at a constant temperature, there was "significant" variation in K_{out} over the course of a day. This drift was attributed to changes in K_0. K_0 may be relatively low when the camera was first powered on, increased over the next hour or two, and perhaps leveled off or even decreased in the afternoon. To help overcome this issue, two sets of images were taken. The first image in a set was the object of interest, and the second image was taken with the lens cap installed. The intensity from this second image was called "K_{cap}" and defined as:

$$K_{cam} = K_{out} - K_{cap} \approx \left[\frac{K_1}{\left[exp\left(\frac{K_2}{T_{body}}\right) - 1\right]} + K_0\right] - \left[\frac{K_1}{\left[exp\left(\frac{K_2}{T_{cap}}\right) - 1\right]} + K_0\right] = \frac{K_1}{\left[exp\left(\frac{K_2}{T_{body}}\right) - 1\right]} + K_0' \quad (17)$$

where:

T_{cap} is the "effective" lens cap temperature, and

$K_0' = \frac{-K_1}{\left[exp\left(\frac{K_2}{T_{cap}}\right) - 1\right]}$.

Because K_{out} and K_{cap} were recorded at nearly the same time, their respective values for K_0 were similar and, hence, cancel out. The quantity K_0' was much smaller and more stable than K_0.

The calibration constants K_0', K_1, and K_2 (for a specific camera, integration time, atmosphere, and distance from camera to target) were estimated via analysis of camera measurements made on a calibrated blackbody source (a model IR-564/301 blackbody system from Infrared Systems Development Corporation). The IR camera was setup and focused on the aperture of the blackbody source. A series of K_{cam} measurements were made over a range of blackbody temperatures, T_1, T_2, T_3, …, T_n. The resulting set of data was modeled as:

$$K_{cam_i} = \varepsilon_{bb} \frac{K_1}{exp\left(K_2/T_i\right) - 1} + (1 - \varepsilon_{bb}) \frac{K_1}{exp\left(K_2/T_{amb}\right) - 1} + K_0' \quad (18)$$

where:

K_{cam_i} is the i^{th} camera measurement at a blackbody temperature of T_i,

i=1, 2, 3, …, n, and

ε_{bb} is the nominal emissivity of the blackbody (0.995 as per specifications).

The first term on the right-hand side arises from the ideal blackbody emission multiplied by the nominal emissivity of the specific blackbody source. Since the blackbody source is not "ideal", the emissivity will be near, but less than 1.0. There can also be a small amount of "ambient" IR reflected toward the camera, hence the second term. The magnitude of the second term should be relatively insignificant at the higher blackbody temperatures of interest.

If the estimates of the unknown parameters are represented by the same symbols with "carets", and let

$$\widehat{K_{cam_i}} = \varepsilon_{bb}\frac{\widehat{K_1}}{exp\left(\widehat{K_2}/T_i\right)-1} + (1-\varepsilon_{bb})\frac{\widehat{K_1}}{exp\left(\widehat{K_2}/T_{amb}\right)-1} + \widehat{K_0'} \tag{19}$$

then these parameters can be estimated iteratively via non-linear regression or other procedures to minimize the sum of squared errors,

$$SSE = \sum_{i=1}^{n}\left(K_{cam_i} - \widehat{K_{cam_i}}\right)^2 \tag{20}$$

Examples of black-body calibration data and the resulting curve-fits are shown in Figure 35. The parameter estimates resulting from analysis of several sets of blackbody calibration data have been listed in Table 10, in which "old camera" refers to FLIR Camera S/N 00036 while "new" camera refers to FLIR Camera S/N 00073. Column "BB" refers to the blackbody source: Old meaning the Infrared Systems Development Model 564/301, S/N 3096K. Note that column "rMSE" refers to the square root of the mean squared error, or $rMSE = \sqrt{SSE/n}$.

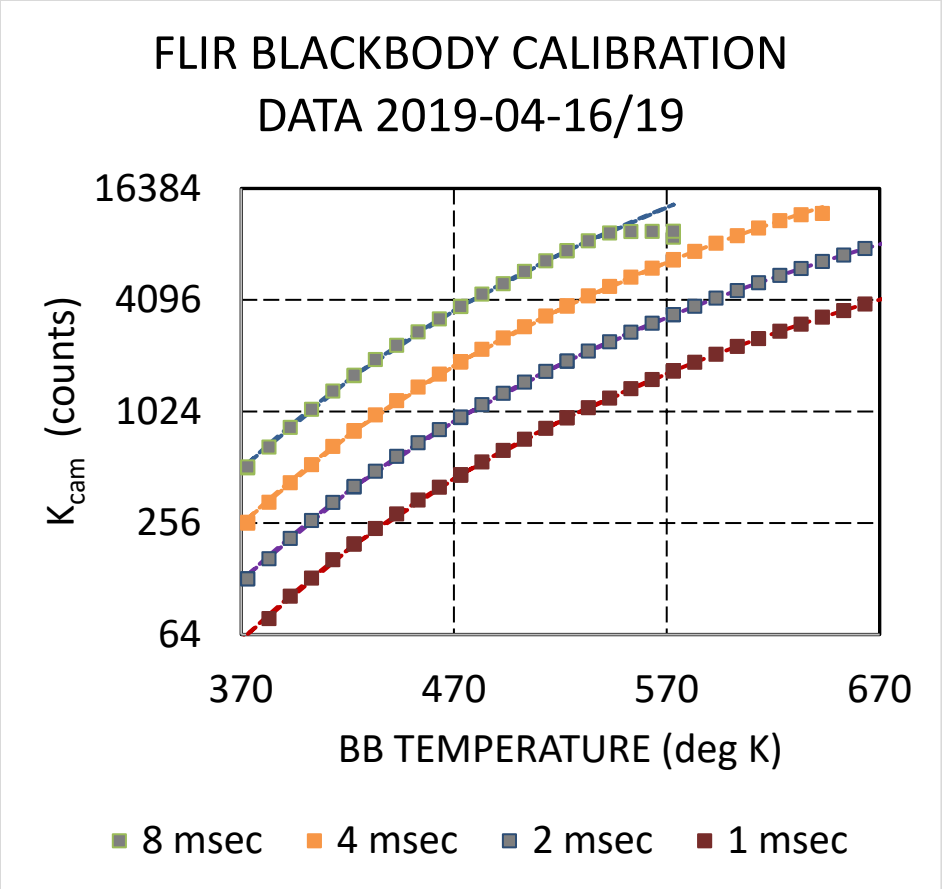

Figure 35: Example of blackbody calibration data and resultant curve fits.

Table 10: Summary of Blackbody Calibration Analysis

Camera	BB	Start	End	Integration Time (msec)	min T (K)	max T (K)	K0 (counts)	K_1 (counts)	K_2 (K)	rMSE (counts)
"New"	"Old"	4/16/2019	4/19/2019	8 msec	323	533	-50	4,902,305	3,383	17.2
"New"	"Old"	4/16/2019	4/19/2019	4 msec	323	583	-11	2,680,679	3,427	8.3
"New"	"Old"	4/16/2019	4/19/2019	2 msec	323	673	-4	1,411,007	3,451	4.5
"New"	"Old"	4/16/2019	4/19/2019	1 msec	323	673	-1	754,050	3,493	2.5
"Old"	"Old"	2/13/2019	2/15/2019	8 msec	373	543	-41	4,150,860	3,354	7.4
"Old"	"Old"	2/7/2019	2/15/2019	4 msec	373	633	-1	2,379,637	3,424	16.4
"Old"	"Old"	2/7/2019	2/7/2019	3 msec	473	673	-79	1,693,596	3,383	12.2
"Old"	"Old"	2/7/2019	2/15/2019	2 msec	373	683	5	1,254,650	3,454	10.6
"Old"	"Old"	2/7/2019	2/15/2019	1 msec	373	683	4	656,414	3,483	6.8
"Old"	"Old"	3/15/2019	3/15/2019	0.5 msec	573	873	28	379,064	3,589	1.8

Before discussing the remaining calibration details, a "model" of the IR measurement process needs to be discussed. The concept of a model was previously introduced above in Equation 18. (The IR signal being measured by the camera was the sum of that which would be emitted by a perfect blackbody, multiplied by the emissivity of the surface, plus a fraction of the ambient IR levels that were reflected from that surface.) For a target object that is enclosed or is part of an enclosure, the reflection component is compounded. The total radiosity of a grey-body surface at temperature T (surface #1), in an enclosure or system of *n* such surfaces is:

$$I_1 = \varepsilon_1 I_{bb}(T) + (1-\varepsilon_1)\sum_{i=1}^{n} I_i F_{i\to 1}\, {A_i}/{A_1} \tag{21}$$

where:

I_i is the total radiosity of the i[th] surface at the wavelength of interest,

ε_i is the emissivity of the i[th] surface,

$F_{i\to j}$ is the view factor of radiation emanating from the i[th] surface and intercepted by the j[th] surface, and

A_i is the area of the i[th] surface.

If the other surfaces are at temperatures similar to or larger than that of surface 1, the reflected component ($(1-e_1)\sum_{i=1}^{n} I_i F_{i\to 1}\, {A_i}/{A_1}$) can be a large proportion of I_1. The incoming IR intensity is often simplified using the concept of "effective" ambient temperature. The effective ambient temperature (T_{amb}) is the temperature at which a blackbody would emit the same level of intensity, i.e.,

$$I_{bb}(T_{amb}) = \sum_{i=1}^{n} I_i F_{i\to 1}\, {A_i}/{A_1} \tag{22}$$

Using the effective ambient temperature notation, the total radiosity of the surface of interest becomes $I_1 = \varepsilon_1 I_{bb}(T) + (1-e_1) I_{bb}(T_{amb})$.

The next level of complexity is introduced by the need for a window. If the object of interest (the airfoil) is enclosed and the camera is located outside the enclosure, then there must be a window through which the camera can "see" the object. No window is 100% transparent. Some portion of I_1 will be absorbed by the window and another portion will be reflected from the inner surface of the window. The portion that remains (τ_w) will be "transmitted" through the window toward the camera. So, at the outer surface of the window, the radiosity becomes

$$\tau_w I_1 = \tau_w \varepsilon_1 I_{bb}(T) + \tau_w (1 - e_1) I_{bb}(T_{amb}) \tag{23}$$

After being transmitted through the window, this radiosity is joined by the ambient IR from outside the enclosure being reflected off the exterior of the window and toward the camera. This new total radiosity is represented by

$$\tau_w I_1 + \rho_w I_{bb}(T_{amb2}) = \tau_w \varepsilon_1 I_{bb}(T) + \tau_w (1 - e_1) I_{bb}(T_{amb}) + \rho_w I_{bb}(T_{amb2}) \tag{24}$$

Note: Equation 24 ignores any possible contribution by IR emitted by the hot window, which is minimal and which if it exists will be lumped into a common intercept term as it is assumed to be constant and independent of the airfoil temperature.

Given the previous assumption that the camera output is a linear function of the input radiosity, then a camera reading can be approximated using Equation 25:

$$\begin{aligned} K_{out}(T) &= a\{\tau_w \varepsilon_1 I_{bb}(T) + \tau_w (1 - e_1) I_{bb}(T_{amb}) + \rho_w I_{bb}(T_{amb2})\} + b \\ &= \tau_w \varepsilon_1 [a I_{bb}(T)] + a\{\tau_w (1 - e_1) I_{bb}(T_{amb}) + \rho_w I_{bb}(T_{amb2})\} + b \end{aligned} \tag{25}$$

$$K_{out}(T) = \tau_w \varepsilon_1 \frac{K_1}{\left[exp\left(\frac{K_2}{T}\right) - 1\right]} + \left\{ \tau_w (1 - e_1) \frac{K_1}{\left[exp\left(\frac{K_2}{T_{amb}}\right) - 1\right]} + \rho_w \frac{K_1}{\left[exp\left(\frac{K_2}{T_{amb}}\right) - 1\right]} \right\} + K_0 \tag{26}$$

$$K_{out}(T) = \tau_w \varepsilon_1 K_{bb}(T) + \{\tau_w (1 - e_1) K_{bb}(T_{amb}) + \rho_w K_{bb}(T_{amb2})\} + K_0 \tag{27}$$

where $K_{bb}(T) = \frac{K_1}{\left[exp\left(\frac{K_2}{T}\right) - 1\right]}$. With the lens-cap correction, the lens cap image is subtracted from the image of the target airfoil surface, so the K_0 terms will cancel (see Equation 28 and 29).

$$\begin{aligned} K_{cam}(T) = [\tau_w \varepsilon_1 K_{bb}(T) + \{\tau_w (1 - e_1) K_{bb}(T_{amb}) + \rho_w K_{bb}(T_{amb2})\} + K_0] \\ - \left[K_{bb}\left(T_{cap}\right) + K_0\right] \end{aligned} \tag{28}$$

$$K_{cam}(T) = \tau_w \varepsilon_1 K_{bb}(T) + \left[\tau_w (1 - e_1) K_{bb}(T_{amb}) + \rho_w K_{bb}(T_{amb2}) - K_{bb}\left(T_{cap}\right)\right] \tag{29}$$

$$K_{cam}(T) = \beta_1 K_{bb}(T) + \beta_0 \tag{30}$$

where

$\beta_1 = \tau_w \varepsilon_1$, and

$\beta_0 = \tau_w(1-\varepsilon_1)K_{bb}(T_{amb}) + \rho_w K_{bb}(T_{amb2}) - K_{bb}\left(T_{cap}\right)$.

If the values of β_0 and β_1 were known, then inverting Equation 30 to calculate the surface temperature would be straight forward. Let

$$K^*_{bb}(T) = \frac{K_1}{e^{K_2/T} - 1} = \frac{K_{cam}(T) - \beta_0}{\beta_1} \tag{31}$$

and

$$T^* = \frac{K_2}{\ln\left(\frac{K_1}{K^*_{bb}} + 1\right)} \tag{32}$$

The estimation of K_1 and K_2 was addressed through the blackbody calibration process; however, the estimation of τ_w, ε_1, T_{amb}, ρ_w, T_{amb2}, and T_{cap} was not addressed. Some of these parameters can be estimated though various experimental measurements, but T_{amb} is nearly intractable. Instead of estimating these components separately, the values of β_0 and β_1 are estimated as "lumped" constants through analysis of in-situ calibration data. It is assumed that β_1 is not dependent on the surface temperature, and for some surfaces, it is likely to not be location-specific (i.e., it is constant for all locations on the surface of interest). This assumption may be good for flat surfaces orthogonal to the camera's line-of-sight, however, emissivity is known to be a function of viewing angle and since the airfoils tested in these experiments were comprised of curved surfaces the viewing angle was a function of the relative position along the chord of the airfoil. The angular deviation between the camera line-of-site and the normal to the airfoil surface can be readily calculated and experiments have been performed to measure emissivity as a function of this angle. To take advantage of this emissivity information, the notation was modified as follows:

$$K_{cam}(T, x/c) = \beta_1 \varepsilon_1\left(\theta(x/c)\right) K_{bb}(T) + \beta_0 \tag{33}$$

where

$\beta_1 = \tau_w$,

$\beta_0 = \tau_w(1-\varepsilon_1)K_{bb}(T_{amb}) + \rho_w K_{bb}(T_{amb2}) - K_{bb}(T_{cap})$, and

$\theta(x/c)$ is the deviation from normal viewing angle as a function of relative chordal location

$$K^*_{bb}(T, x/c) = \frac{K_{cam}(T, x/c) - \beta_0}{\beta_1 \varepsilon_1(\theta(x/c))} \tag{34}$$

Determining β_0 is a little more complicated. Its value is highly specific to the temperatures of each surface of the enclosure, and therefore, is dominated by T_{amb}. β_0 includes a component that is dependent on T, but largely because $F_{1\to1} = 0$, the dependence on T is assumed to be small and is ignored in this analysis. β_0 has potential to be geometry- and location-specific. If data could be generated where K_{cam} was measured over a wide-range of airfoil locations with known temperatures, while all other surface temperatures and other factors that may affect β_0 are held constant at the same conditions that apply during actual airfoil tests, then this data could be analyzed via regression techniques to estimate both β_0 and β_1. β_0 can be "fit" to the data either as a single constant, or as a function of position on the airfoil surface. The process of generating and analyzing such data is referred to as "in-situ" calibration.

By varying the coolant flow rate and/or coolant temperature, it was possible to vary the airfoil surface temperature while maintaining all other conditions constant in the hot-test section. A thermal-break in the airfoil mounting surface restricted heat flux between the airfoil and the surrounding surfaces. The coolant flow rate, relative to the hot gas flow, was small so that changes to the coolant flow rate had little impact on the hot gas downstream of the airfoil. A calibration airfoil of the same size, shape, material, and high-emissivity coating was fabricated for in-situ calibration. This airfoil was fitted with a number of thermocouples whose leads were spot-welded to airfoil surface to form "intrinsic junctions" (Figures 36 and 37). The intrinsic thermocouple output signal corresponds to the average temperature across the intrinsic junction. Figure 36 shows an IR image of this calibration airfoil in use and thermocouple assignments are shown. The "red" circles show the locations for which the K_{cam} signals were averaged to represent the IR intensity.

To analyze the in-situ results and estimate the slope ($\widehat{\beta_1}$) and a single common intercept ($\widehat{\beta_0}$), let K_{cam} be the dependent or "Y" variable in a standard regression, and let $\hat{\varepsilon}\widehat{K_{bb}}(T)$ represent the independent or "X" variable, where:

- T represents the measured thermocouple temperature (K),
- $\widehat{K_{bb}}(T) = \frac{\widehat{K_1}}{e^{\widehat{K_2}/T} - 1}$,
- $\widehat{K_1}$ and $\widehat{K_2}$ represent estimated values of K_1 and K_2 from the blackbody calibration, and
- $\hat{\varepsilon}$ represents the estimated emissivity (a function of x/c).

An example set of in situ calibration data is shown in Figure 38. Note that there was more noise in this data compared to the blackbody calibration data. This was attributable to less control over the experimental environment and lower repeatability in these large-scale experiments, plus small deviations from assumptions, etc. The trend line shows the simple regression fit with an R^2 of 98% and slope and intercept of 0.9694 and 2412.1, respectively. These slope and intercept estimates were combined with the measured IR intensities to estimate the temperatures for each data point by applying Equation 34 and 32 above (and substituting estimated values of K_1, K_2, and ε). The results of this calculation are shown plotted against the measured temperatures in Figure 38. A measure of the "fit" was constructed by computing the $rMSE = \sqrt{\frac{1}{n}\sum(T - T^*)^2}$, which equals 6.34 K in this example.

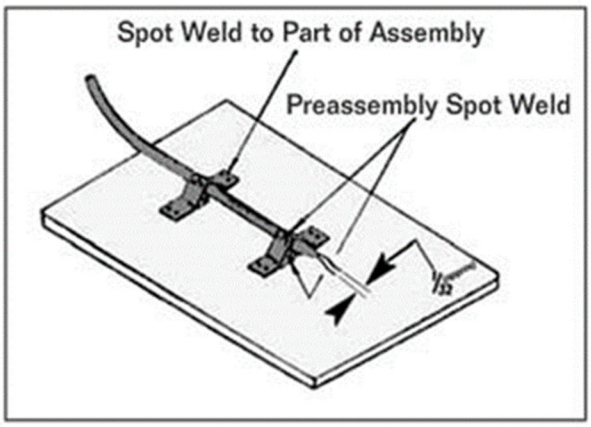

Figure 36: Schematic of an "intrinsic" thermocouple junction.

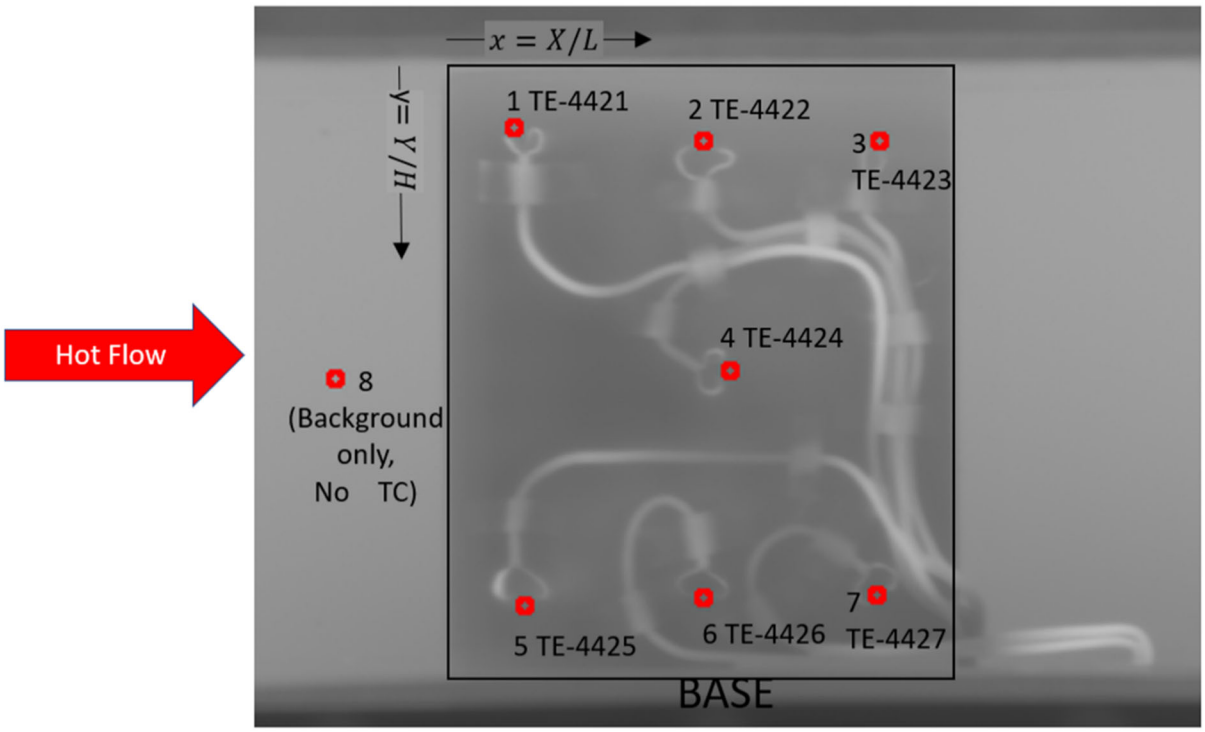

Figure 37: IR image of an in-situ calibration airfoil in use. Thermocouple channel assignments and IR intensity sampling locations are shown by red circles.

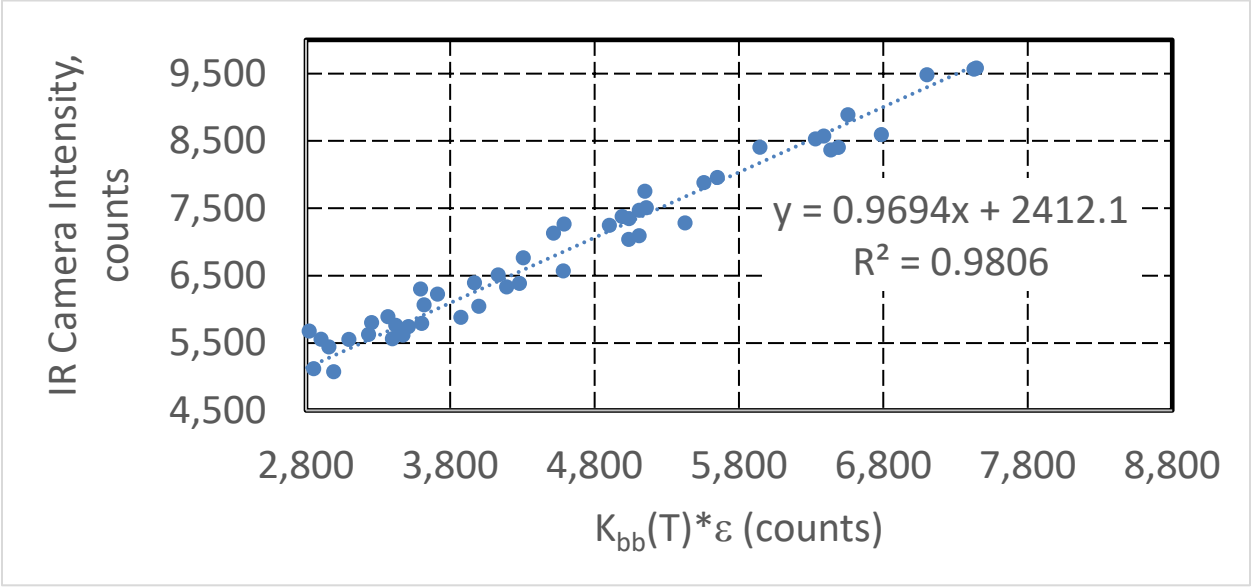

Figure 38: In-situ calibration data and regression "fit". In-situ calibration data from 3/14/2022.

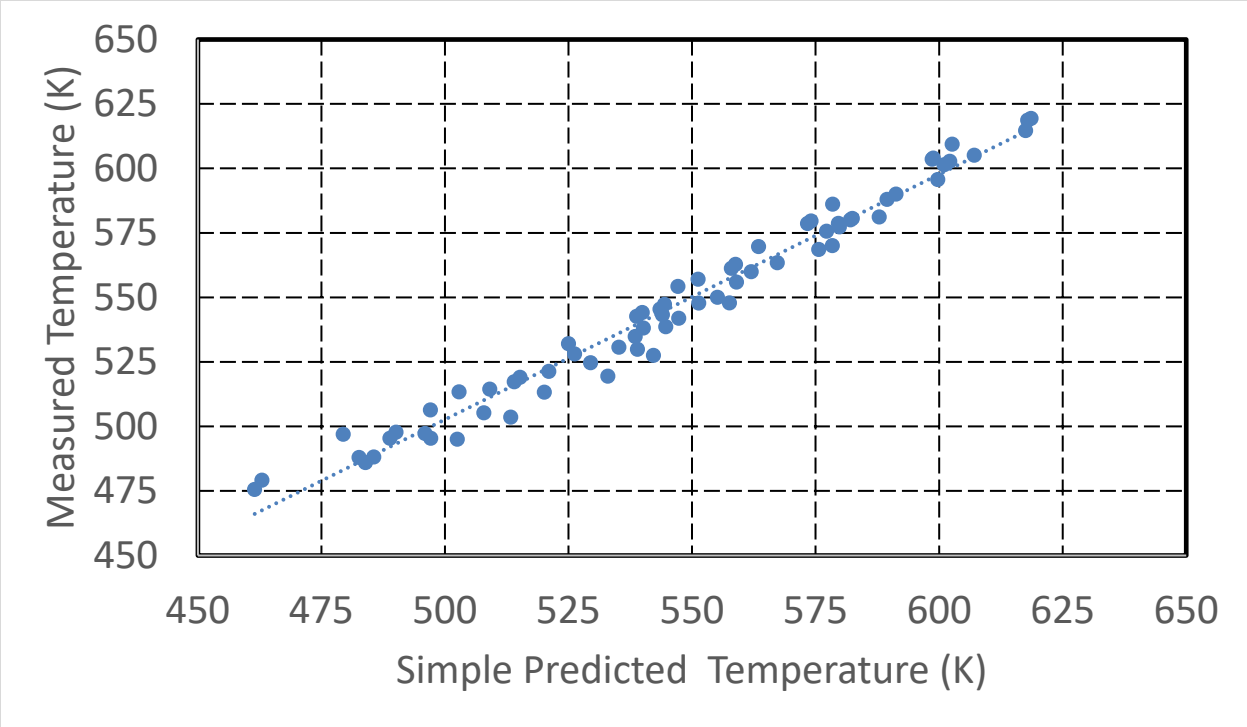

Figure 39: Plot of measured airfoil surface temperature vs. IR temperature from regression analysis of in-situ calibration data. In-situ calibration data from 3/14/2022.

Part of the lack-of-fit in Figure 39 is due to the assumption that β_0 is constant across the surface of the airfoil. This assumption can be relaxed by letting β_0 be a function of location on the airfoil. The simplest method to achieve this was to apply multiple linear regression (as opposed to the simple linear regression applied previously) and let K_{cam} be modeled as:

$$K_{cam_i} = \beta_{00} + \beta_x\left({}^{x_i}/_{c}\right) + \beta_y\left({}^{y_i}/_{h}\right) + \beta_{x^2}\left({}^{x_i}/_{c}\right)^2 + \beta_{y^2}\left({}^{y_i}/_{h}\right)^2 + \beta_{xy}\left({}^{x_i}/_{c}\right)\left({}^{y_i}/_{h}\right) + \beta_1\left(\varepsilon_i K_{bb}(T_i)\right) \tag{35}$$

Multiple regression of the in-situ calibration data is applied to estimate the individual β's. Note that:

$$\beta_0(x/c, y/h) = \beta_{00} + \beta_x({}^{x}/_{c}) + \beta_y\left({}^{y}/_{h}\right) + \beta_{x^2}({}^{x}/_{c})^2 + \beta_{y^2}\left({}^{y}/_{h}\right)^2 + \beta_{xy}({}^{x}/_{c})\left({}^{y}/_{h}\right)$$

This process was applied to the example data and the temperature estimates were revised using the location-specific β_0's. The results are shown in Figure 40. Note the agreement between

measured and estimated temperature was improved greatly. The rMSE for these results was reduced from 6.3 K to 3.1 K.

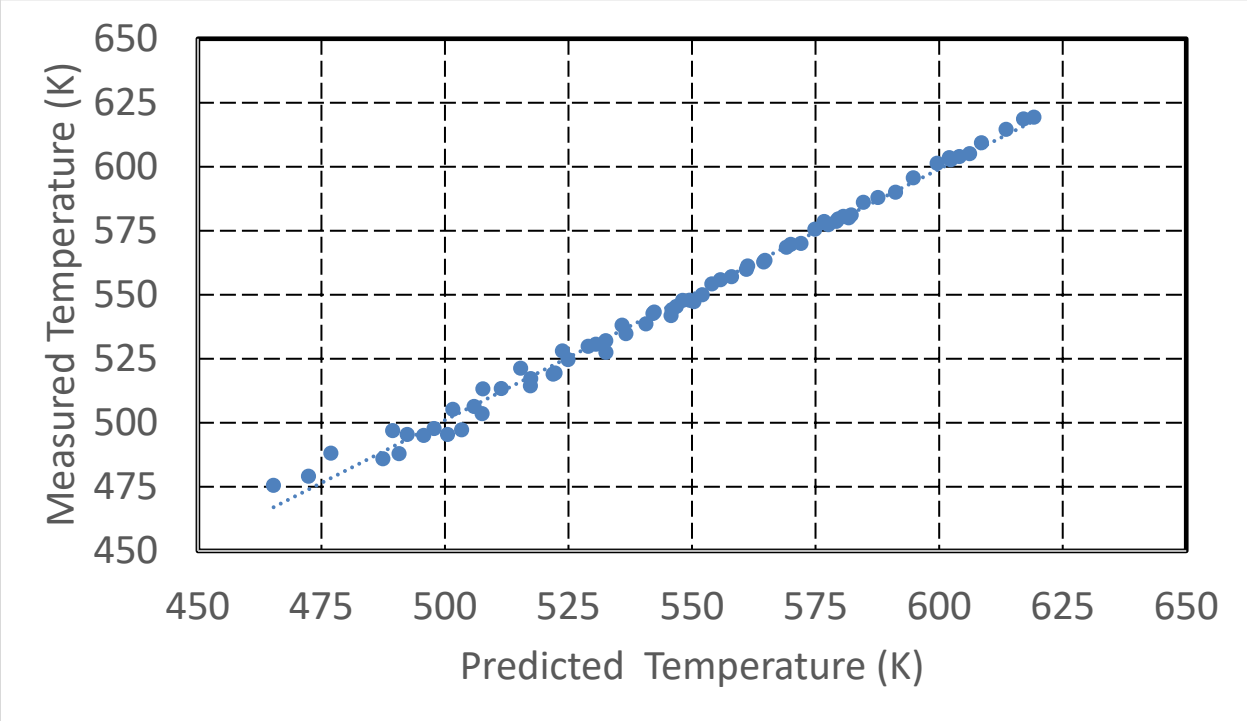

Figure 40: Measured vs. predicted temperature from analysis of in-situ calibration data with b_0 as a function of location. In-situ calibration data from 3/14/2022.

In-situ calibration data were measured on four occasions: 4/27/2021, 3/14/2022, 3/21/2022, and 3/22/2022. The regression analyses of the data set have been summarized in Table 11.

Table 11: Regression Coefficients Resulting from CHP In-situ Calibration Tests

Test Date	Camera	Int Time	Simple β_0	Simple β_1	Simple R^2	Simple RMSE	β_{00}	β_x	β_y	β_{x2}	β_{y2}	β_{xy}	β_1	R^2	RMSE
4/27/2021	00036	4 msec	2,775	0.890	99.00	2.9	2,724	-301	#N/A	674	#N/A	#N/A	0.898	99.12	2.7
3/14/2022	00036	4 msec	2,412	0.969	98.06	6.3	2,920	-834	357	363	-1,288	740	0.944	99.71	3.1
3/21/2022	00036	4 msec	2,696	0.925	96.98	7.9	3,355	-1,213	125	596	-1,150	882	0.897	99.22	4.6
3/22/2022	00036	4 msec	2,250	0.963	98.03	6.5	2,790	-977	293	575	-1,219	685	0.933	99.81	2.5

Analysis of these in-situ calibration data was dependent upon knowledge of how the angular deviation of the line-of-site from the normal to the airfoil surface (a function of the airfoil profile) and knowledge of how the emissivity of the airfoil surface deviated with this angle. The first was obtained from analysis of the airfoil profile. The second was based on experimental measurements. An exaggerated airfoil profile is shown in Figure 41. The thickness of the NACA-0024 airfoil can be described by a polynomial function of distance from the leading edge (Airfoil Tools, 2022). The theoretical chord length of the CHP airfoil was 0.0504 m (2 in.), but the actual profile length was truncated at 0.0437 m (1.72-in.). The tangent to the airfoil surface at any location along the airfoil can be calculated by the derivative of the polynomial function, $\frac{dy}{dx}$. The slope of the normal to the airfoil surface was given by $-\frac{dy}{dx}^{-1}$. The angle between the line-of-site and the normal was $\theta = \tan^{-1}(-\frac{dy}{dx})$. In analyzing images of the airfoil, i was equal to the number of pixels from the leading edge of the airfoil. The ratio of i to the airfoil thickness, in pixels, provided x relative to the truncated chord length, and the product of that ratio and (1.72/2.00) was x/c, from which θ was computed. θ did not vary widely for this profile shape except near the leading edge. In general, the variation in θ was within +/- 10 degrees over 90% of the chord length (Figure 42).

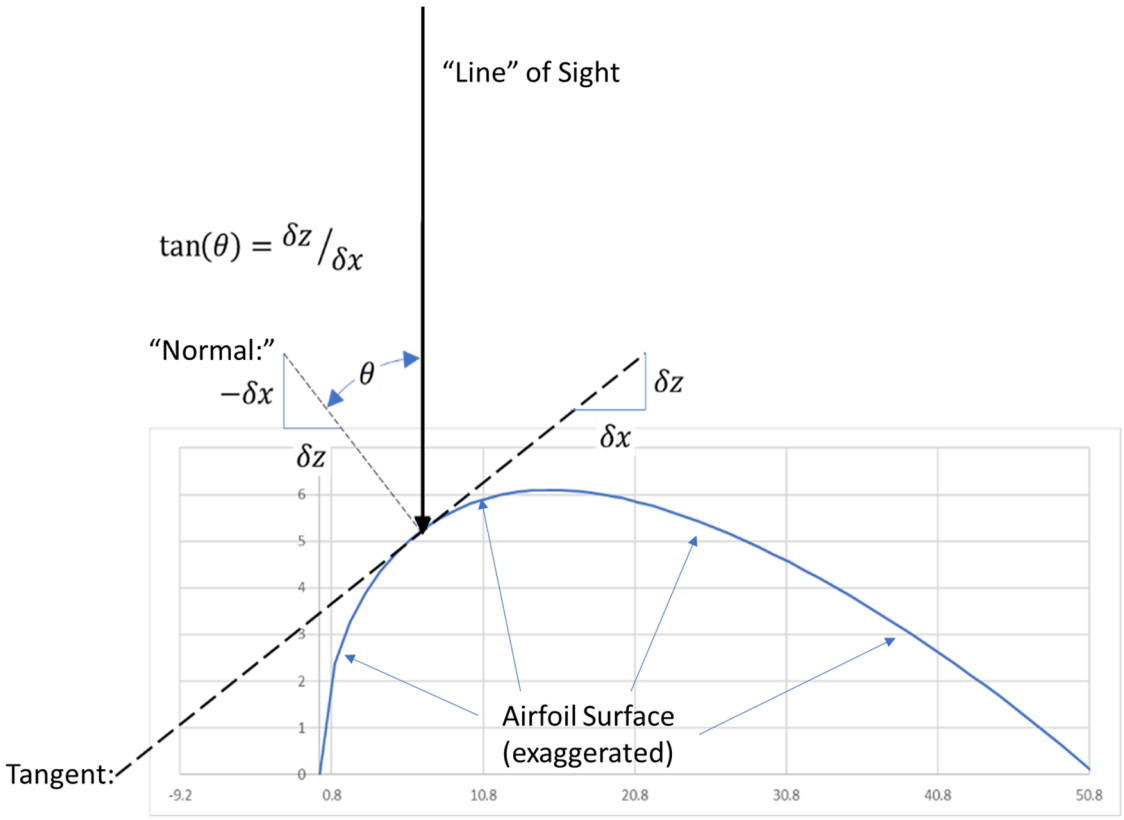

Figure 41: Schematic of an airfoil profile vs. position (x) along the chord and showing an example of the normal to the airfoil surface and the camera line-of-sight.

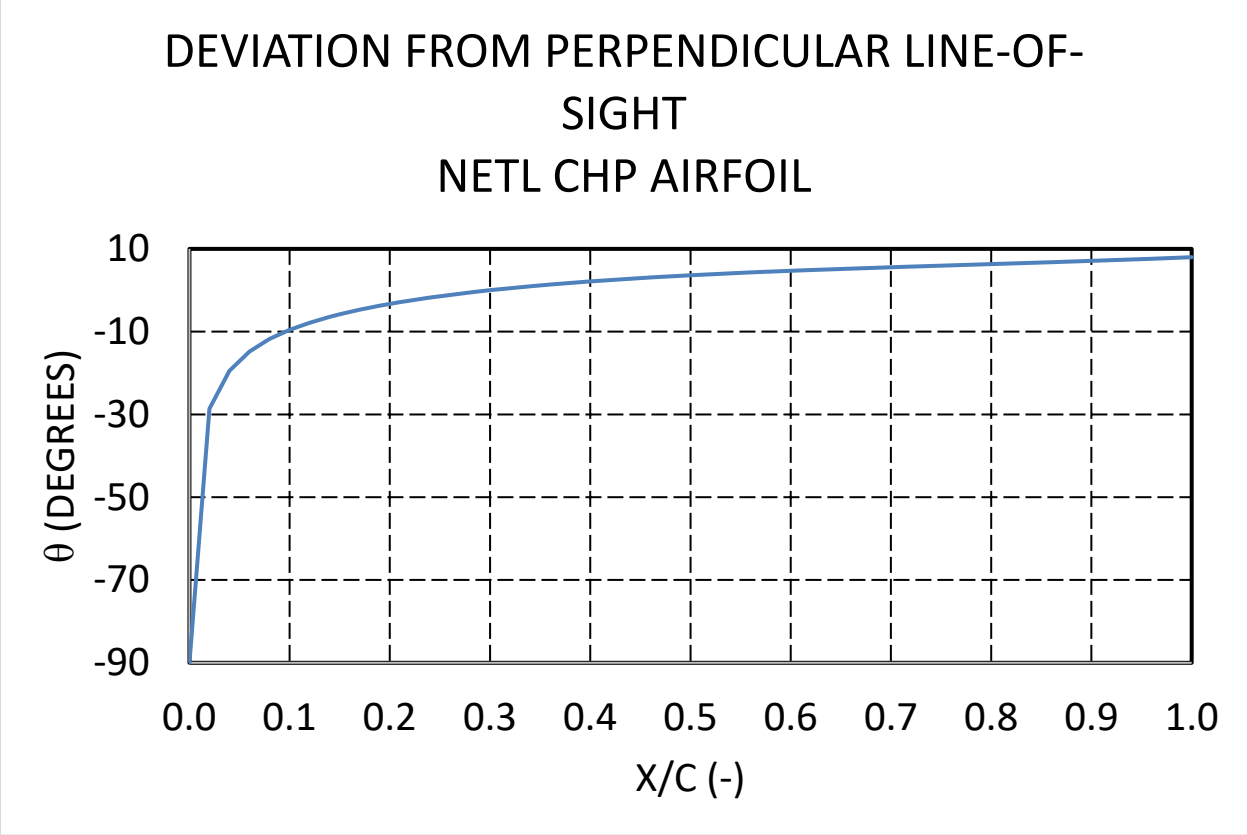

Figure 42: Deviation of the camera line-of-site vs. the normal to the airfoil surface as a function of the ratio of distance from the leading-edge to the chord length (x/c).

The emissivity of a surface was estimated from the ratio of the measured IR intensity of a flat sample surface with that of a blackbody at the same temperature. This ratio, however, was affected by variations in reflected ambient IR levels, signal offsets, etc. Instead, the IR intensity was measured over a wide-range of measured temperatures (using an intrinsic thermal junction as in the in situ experiments) and analyzed to determine emissivity. A flat coupon was fabricated with an intrinsic thermocouple junction and painted with the same high-emissivity coating. The coupon was heated by placing it on a laboratory hot plate. The dataset consists of n pairs of measured temperature and K_{cam}. The "model" for these measurements is

$$K_{cam_i} = \varepsilon K_{bb}(T_i) + (1-\varepsilon)K_{bb}(T_{amb}) + K_0' \tag{36}$$

A plot of K_{cam_i} vs $K_{bb}(T_i)$ would be linear with a slope of ε and an intercept of $(1-\varepsilon)K_{bb}(T_{amb}) + K_0'$. Simple linear regression was used to find the slope ε. To find ε as a function of angle, the IR camera was mounted on a rotatable arm to vary the viewing angle with respect to the normal direction. A number of emissivity measurement experiments were conducted over a range of viewing angles. The results are shown in Figure 43. In practice, a quadratic regression equation was applied to estimate emissivity as a function of angle, θ:

$$\hat{\varepsilon}(\theta) = 0.78879 + 0.0001313210\theta - 3.27148 \cdot 10^{-5}\theta^2 \quad (37)$$

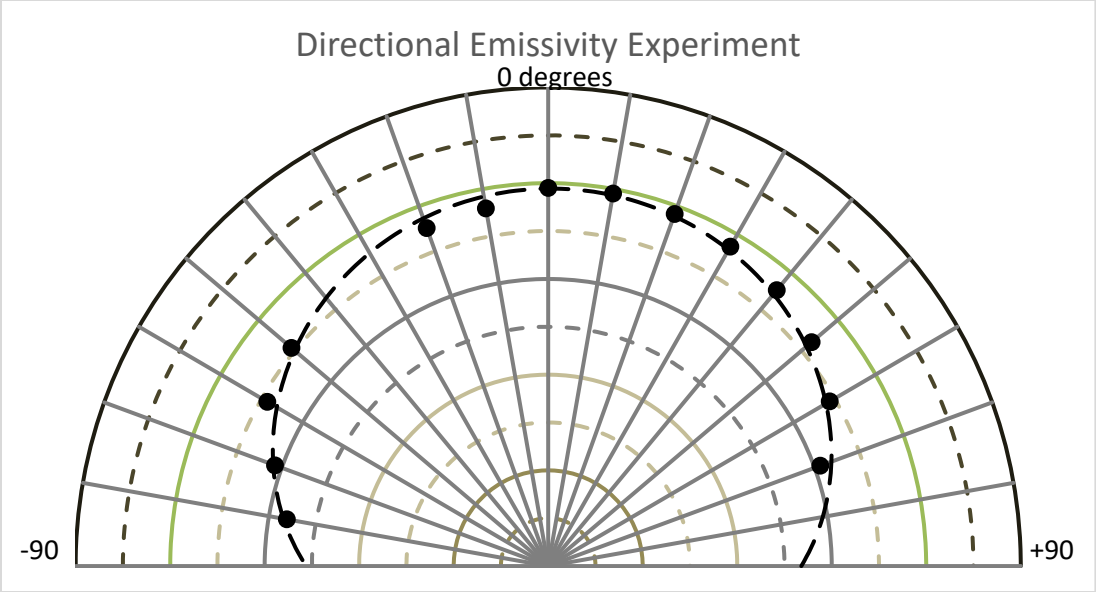

Figure 43: Polar plot showing emissivity of Krylon High Heat Max paint as a function of the "viewing angle" (0 degrees = line-of-sight is perpendicular to the test coupon).

4.3.2 Image Analysis and Post-Processing

AM airfoils were tested sequentially in the NETL CAT Rig over a period of time extending from June 2021 through April 2022. A test run typically consisted of subjecting an airfoil to a series of cooling flow rates. At each steady-state test condition (i.e., coolant flow rate), IR images of the airfoil were collected over several camera integration times (typically 2, 4, and 8 msec). At each integration time, a series of 100 infrared images were saved, and another 100 images were saved with the lens cap installed. A typical test run over the course of a day would produce 12 test conditions; three integration times at each test condition; two target objects (airfoil vs. cap) at each integration time; and 100 images at each integration time. In other words, approximately 7,200 images were collected per test-day. The steps involved in post-processing these images were as follows:

- Export the raw count intensity image files from FLIR ATS format to TIFF format using the FLIR Research IR Software.
- Reduce the 100 replicate images in each file to a single "average" image using an ImageJ macro script.
- Load the average images for a given day into a single TIFF stack in ImageJ.
- Subtract the lens cap images from their corresponding airfoil images (ImageJ).

- Segregate the resulting airfoil images into separate stacks according to their integration times.
- Select a particular stack (integration time) for subsequent processing.
- Adjust image "registration" if necessary. Sometimes the camera and/or CAT rig may shift slightly during a test. This step realigns the images (manually with ImageJ tools) as needed. Also rotate the images to obtain the desired orientation. In some instances, the camera and airfoil may not be "square" to each other. Those differences are corrected in this step also.
- Identify the coordinates (pixels) of the upper left corner of the airfoil image, image width, and image height. These vary slightly from run to run due to daily installation of the camera and disturbances to the camera supports between runs.
- Perform a series of calculations leading to estimated emissivity as a function of image column (x).
- Create image files for x/c, $(x/c)^2$, $(x/c)^3$, and $(x/c)^{-0.5}$.
- Use the (x/c) files to compute a file for dz/dx.
- Compute a file for θ.
- Compute estimated emissivity as a function of θ. For non-airfoil portions of the image, emissivity is set to 0.7888. For airfoil portions, it is calculated from θ according to Equation 37.
- Apply the blackbody calibration coefficient estimates and the in-situ calibration coefficient estimates to estimate temperature for every pixel in the image, first by computing K* (Equation 34) and then by calculating T* (Equation 32).

At this point, T* has been calculated. Images can be further processed, as needed, to create images of airfoil surface temperature, cooling effectiveness, etc., or compute statistics such as the average airfoil surface temperature.

4.4 EXTERNAL SURFACE ROUGHNESS

AM surfaces contain partially-sintered particles that subsequently produce surface roughness. There are many factors that can affect the surface roughness in AM parts and controlling surface roughness was outside the scope of the present study.

The approach taken to address the surface roughness effects was to characterize the surface roughness on each airfoil using a portable Mitutoyo SJ210 surface roughness instrument. For each airfoil, roughness measurements were taken in five different span-wise regions and five different chord-wise regions. Since the surfaces of these airfoils had to be painted with a high-emissivity paint before testing, the measured Ra (centerline average roughness) values before, and after, painting have been presented in Table 12. The values listed in Table 12 represent the averages from five different scan regions.

The data in Table 12 below show the following. First, there was no statistical difference between the span-wise and chord-wise scan directions. This is expected because the external airfoil surface was oriented perpendicular to the build direction, and these surfaces should be uniform.

Secondly, there was a significant difference between the NETL double-wall airfoil surface finish and the baseline designs. This variation was due to different companies that manufactured these airfoils. The manufacturer of the NETL double-wall design polished the as-fabricated part before shipment. Finally, the surface roughness was significantly reduced by the painting process and airfoil-to-airfoil variations after painting were within 1 micron.

Table 12: Measured Surface Roughness (Ra) for AM Airfoils Before/After Painting (mean ± 2 standard deviations)

Airfoil Internal Cooling Design		Ra As Received (microns)	Ra After Painting (microns)
Baseline vane	Span-wise	5.0 ± 0.6	1.4 ± 0.3
	Chord-wise	5.7 ± 1.7	1.5 ± 0.4
Baseline blade	Span-wise	3.6 ± 0.8	0.8 ± 0.15
	Chord-wise	3.8 ± 0.6	1.0 ± 0.2
NETL double -wall	Span-wise	1.1 ± 0.2	1.0 ± 0.3
	Chord-wise	1.1 ± 0.15	0.7 ± 0.3

Bons (2010) has presented a thorough review of surface roughness effects in gas turbines. As described by Bons, there are numerous approaches to convert measured surface roughness parameters to equivalent sand grain roughness. In a previous study (Searle et al., 2021), friction factors and surface roughness for AM surfaces oriented perpendicular to the build direction were measured. Four different correlations for converting Ra to equivalent sand grain roughness were investigated and compared to measured friction factors. The correlation by Kilpatrick and Kim (2018) as shown in Equation 38 was selected as the best fit to experimental data in that previous study. This correlation was very similar to the Schaffler (1980) correlation for forged and machined blades (Equation 39).

As described by Bons (2010), the flow regime can be estimated using a non-dimensional roughness parameter, $k^+ = k_s u_\tau / \nu$. If this k+ roughness parameter is less than 5, then the flow can be treated as aerodynamically smooth. The shear velocity, u_τ, was calculated from the boundary layer code. The kinematic viscosity, ν, was calculated at the wall conditions, and the equivalent sand grain roughness correlation was calculated using both correlations.

$$k_s = 8\,Ra \tag{38}$$

$$k_s = 8.9\,Ra \tag{39}$$

The average surface roughness after painting was 1.1 micron, and the variation of k+ is shown in Figure 44 44. In summary, painting the airfoils with high-emissivity paint reduced the surface

roughness to the point that the external flow regime could be considered aerodynamically smooth for the test conditions discussed in this paper.

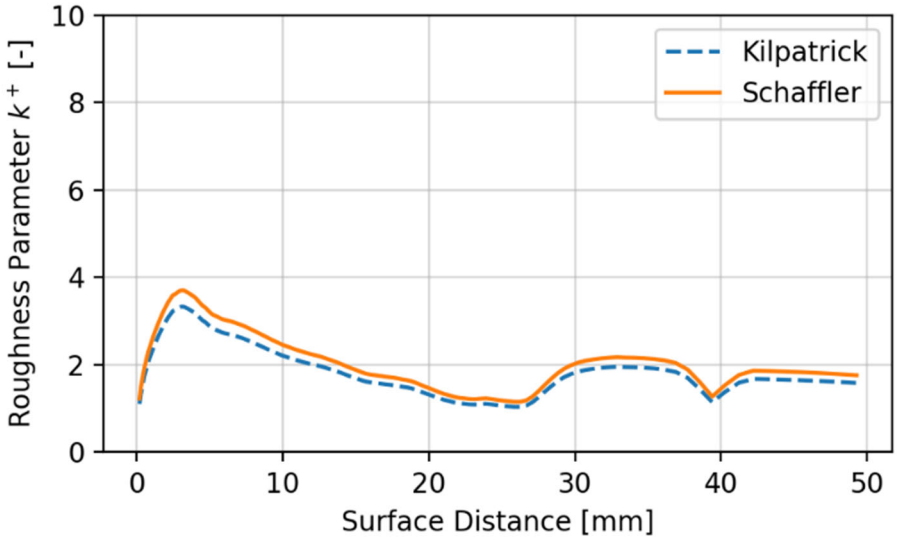

Figure 44: k+ for AM airfoils (after painting).

4.5 ATTEMPTS TO MEASURE INTERNAL COOLING EFFICIENCY

In its simplest form (Equation 40), internal cooling efficiency is defined as the ratio of coolant temperature increase as it flows through the internal cooling passages, and the maximum cooling potential (i.e., metal temperature minus coolant inlet temperature). To the authors' knowledge, experimentally-measured internal cooling efficiencies for an integrated airfoil cooling design have not been published previously, however, as described in Section 2.4, this cooling performance parameter can have a significant impact on the overall performance for small (5–10 MW) gas turbine CHP plants.

$$\eta_c = \frac{T_{c,out} - T_{c,in}}{T_m - T_{c,in}} \tag{40}$$

In this project, experimental measurements were planned for each of the parameters needed to compute internal cooling efficiency (Equation 40). For the metal temperature, the IR estimates of airfoil surface temperature were available, and the initial plan involved using the average measured wall temperature for T_m. For the coolant inlet temperature, the thermocouple temperature measurement of the air in the coolant plenum, near the base of the airfoil, was used. The coolant outlet temperature was difficult to measure particularly for small physical features like the coolant exit slots. The thermal gradients were also large, so the measurements were sensitive to probe alignment. The challenges with measuring coolant outlet temperature may explain the lack of published internal cooling efficiency measurements.

4.5.1 Measurements of Mass Weighted Average Coolant Outlet Temperature

Several of the airfoil designs, including both baseline designs, vented the spent coolant through multiple slots in the trailing edge. To measure the coolant outlet temperature, the approach involved measuring the temperature and velocity profiles at the coolant exit plane. This involved translating a total pressure probe and two Type-K thermocouples along the coolant exit plane (Figure 45). A 1-mm diameter boundary layer probe was used to measure the total pressure, and the static pressure was measured at the wall of the test section (same axial plane as the velocity probe). Two 0.8-mm diameter Type-K thermocouples were attached to the velocity probe to gather temperature data along the coolant exit plane. These thermocouples were oriented parallel to the velocity probe at elevations of 3 mm and 6 mm above the velocity probe. The translation stage was programmed to collect data at 80 locations over a span of roughly 53 mm. At each location, the translation stage stops to collect pressure and temperature data for 11 seconds before moving to the next location. Approximately 10 samples were averaged at each probe location to produce plots like those shown in Figure 46. The general idea was to collect these temperature and pressure measurements, determine the mass flow rate and temperature of each coolant jet, and then combine the jet data to obtain a single average coolant outlet temperature.

The velocities were calculated using isentropic compressible flow relations (Equation 41). The measured pressure ratio was used to solve for the Mach number (M), then the jet velocity was computed as the product of M times c, where c was the speed of sound at the jet temperature and test section pressure. The jet Mach numbers were typically in the 0.2–0.4 range, which was sufficiently high to justify use of the compressible flow relation.

$$\frac{P_{tot}}{P_0} = \left(1 + \frac{\gamma - 1}{2} M^2\right)^{\frac{\gamma}{\gamma - 1}} \tag{41}$$

where

$P_{tot} = P_0 + \Delta P$ is the stagnation pressure (Pa),

P_0 is the static pressure (Pa),

ΔP is the pitot differential pressure (probe minus static),

M is the Mach number of the stream, and

$\gamma = {C_p}/{C_v} \approx 1.39$ for air in this temperature range.

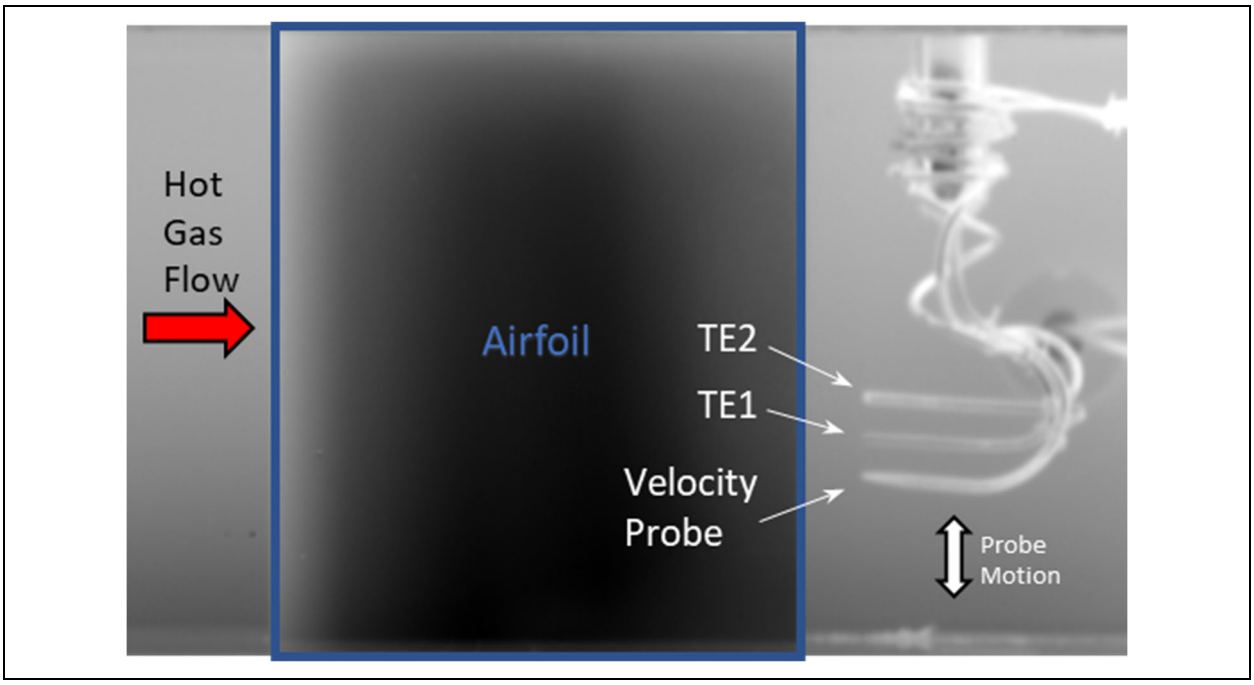

Figure 45: IR image showing an airfoil, a traversing pitot tube for measurement of coolant outlet velocities, and thermocouples (TCs) for measurement of coolant outlet temperatures.

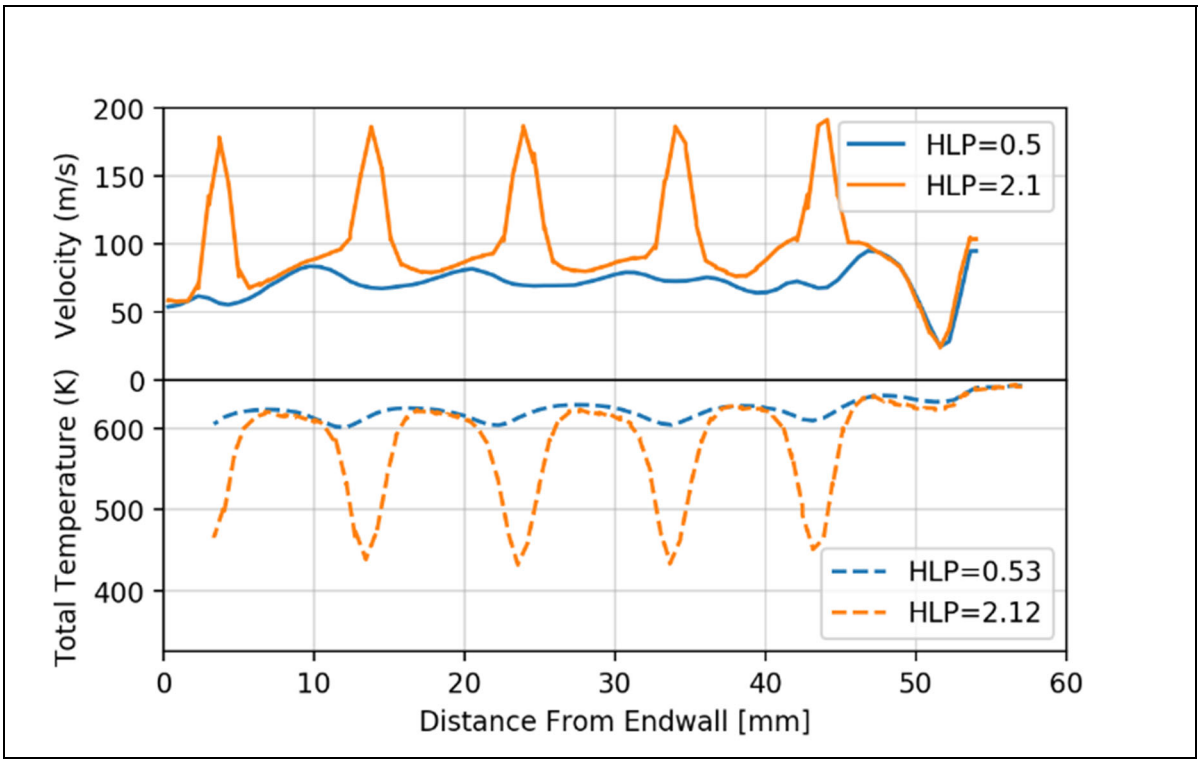

Figure 46: Baseline vane coolant exit profiles (velocity and total temperature).

The jet density was computed from the measured jet temperature (minimum) and static pressure, and the product of density, velocity, and slot area was used to compute a mass flow for each individual jet. An example calculation is shown in Table 13. The mass flows were then summed across the individual jets and the total calculated mass flow distribution at the outlet was compared to the measured coolant inlet flow (Figure 47). For one of the airfoils (the baseline blade design), the computed coolant exit flow was within a fraction of a percent of the measured coolant flow rate. However, for the baseline vane design data, the measured flow at the outlet was only 80% of the computed coolant flow. There was some evidence to suggest that the coolant jets exiting the baseline vane were deflected at the lower flow conditions (see Figure 46). If the directions of the coolant exit jets were changing as the coolant flow was varied, then this approach would not provide an accurate measurement of the mass flow rate of each jet. The stagnation pressure probe measurement technique was sensitive to flow incidence angle. The probe position was aligned at ambient temperature conditions with the underlying assumption that the flow incidence would not change with variations in coolant mass flow rate and operating temperature.

The mass closure for the baseline blade was acceptable, so the weighted average coolant exit temperature was calculated as:

$$T_{c.out} = \frac{\sum_{i=1}^{n_{jets}} \dot{m}_i c_{p_i} T_{jet_i}}{\sum_{i=1}^{n_{jets}} \dot{m}_i c_{p_i}} \tag{42}$$

where:

$T_{c.out}$ is the average coolant exit temperature (K),

$\dot{m}_i$ is the calculated mass flow rate of the ith coolant jet (kg/sec),

c_{p_i} is the specific heat of the ith coolant jet (kJ/kg K), and

T_{jet_i} is the measured jet temperature (K).

An argument could be made that the thermocouple probes used to measure the jet temperature were registering the stagnation temperature as opposed to the static temperature of these streams, or perhaps a recovery temperature (somewhere between the static and stagnation temperatures). If this assertion were true, then the density used to compute the jet mass flow rates would be too low and the temperatures used to compute T_{avg} would be too high. The adiabatic ratio of stagnation temperature to static temperature is given by Equation 43:

$$\frac{T_{stagnation}}{T_{static}} = 1 + \frac{\gamma - 1}{2} M^2 \tag{43}$$

For the range of temperatures in the sample calculations, this ratio averages approximately 3.85%. For the majority of the total jet mass flows, an increase in mass flow due to a reduction in the measured temperature (and subsequent increase in gas density) further exasperates the mass balance error. Therefore, corrections for the stagnation temperature, or recovery temperature corrections, were not applied to this dataset.

Table 13: Sample Calculations Involving Coolant Exit Velocity and Temperature

Parameter	Jet 1	Jet 2	Jet 3	Jet 4	Jet 5	Total	Average
Jet Height (m)	0.0047	0.0047	0.0047	0.0047	0.0047		
Jet Width (m)	0.0013	0.0013	0.0013	0.0013	0.0013		
Jet Area (m^2)	5.97E-06	5.97E-06	5.97E-06	5.97E-06	5.97E-06		
Jet Temp (K)	472	420	415	419	435	2,161	432
Jet Density (kg/m^3)	0.786	0.883	0.894	0.886	0.854		
Max Probe dP (Pa)	13,927	15,099	15,237	15,322	16,258		
c_p (J/kg K)	1,028	1,028	1,028	1,028	1,028		1,028
c (m/sec)	436	411	409	410	418		
Total Coolant Flow (kg/sec)						0.0038537	
P_0 Static Pressure (MPa)	0.106525	0.106525	0.106525	0.106525	0.106525		
Max Probe dP (Pa)	13,927	15,099	15,327	15,322	16,258		
P_{tot} (MPa)	0.120452	0.121624	0.121852	0.121847	0.122783		
P_{tot}/P_0 (-)	1.13074	1.14174	1.14388	1.14383	1.15262		
Incompressible Flow:							
Jet Velocity (m/sec)	188	185	185	186	195		
Jet Mach #	0.43	0.45	0.45	0.45	0.47		
Jet Mass Flow (kg/sec)	0.000883	0.000974	0.000985	0.000983	0.000994	0.004821	
% Total Mass Flow	22.9%	25.3%	25.6%	25.5%	25.8%	125.1%	
mdot c_p T (W)	428.3	420.9	420.1	423.1	444.1	2,136	
mdot c_p (W/K)	0.907	1.001	1.012	1.011	1.022	4.954	
Average Coolant Out. T (K)							431
Compressible Flow:							
Jet Velocity (m/sec)	184	181	180	182	190		
Jet Mach #	0.423	0.439	0.441	0.442	0.455		
Jet Mass Flow (kg/sec)	0.000864	0.000952	0.000962	0.000960	0.000970	0.004708	
% Total Mass Flow	22.4%	24.7%	25.0%	24.9%	25.2%		
mdot c_p T (W)	419.1	411.1	410.2	413.2	433.0	2,087	
mdot c_p (W/K)	0.888	0.978	0.989	0.987	0.996	4.84	
Average Coolant Out. T (K)							431
Average Metal Temperature (K)							**456**
Coolant Inlet Temperature (K)							**327**
Internal Cooling Efficiency (-)							**81%**

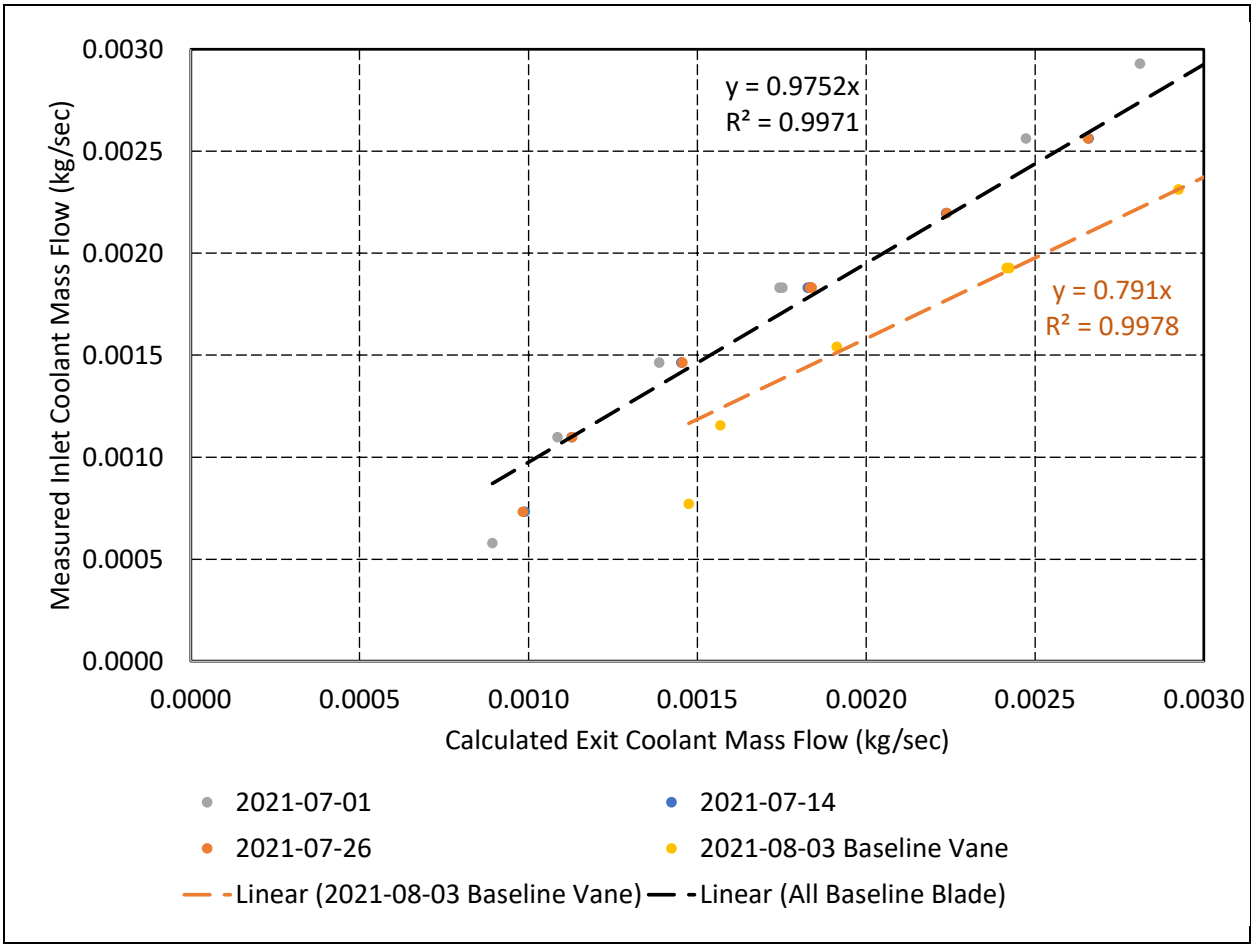

Figure 47: Measured coolant flow vs. that computed from coolant exit jet calculation.

The weighted average coolant exit temperature, $T_{c.out}$, demonstrates certain behaviors that were expected. For example, $T_{c.out}$ decreased as the coolant flow rate increased (Figure 48). Most of the test results for the two baseline airfoils fell on a single line, except that of the test performed on 7/1/2021. Since this was the first test using the translation stage, velocity, and temperature probe setup, the probe thermocouples on that test date were not properly aligned with the airfoil trailing edge. As a result, the temperature probes were measuring a larger proportion of the hot mainstream temperature on 7/1/2021.

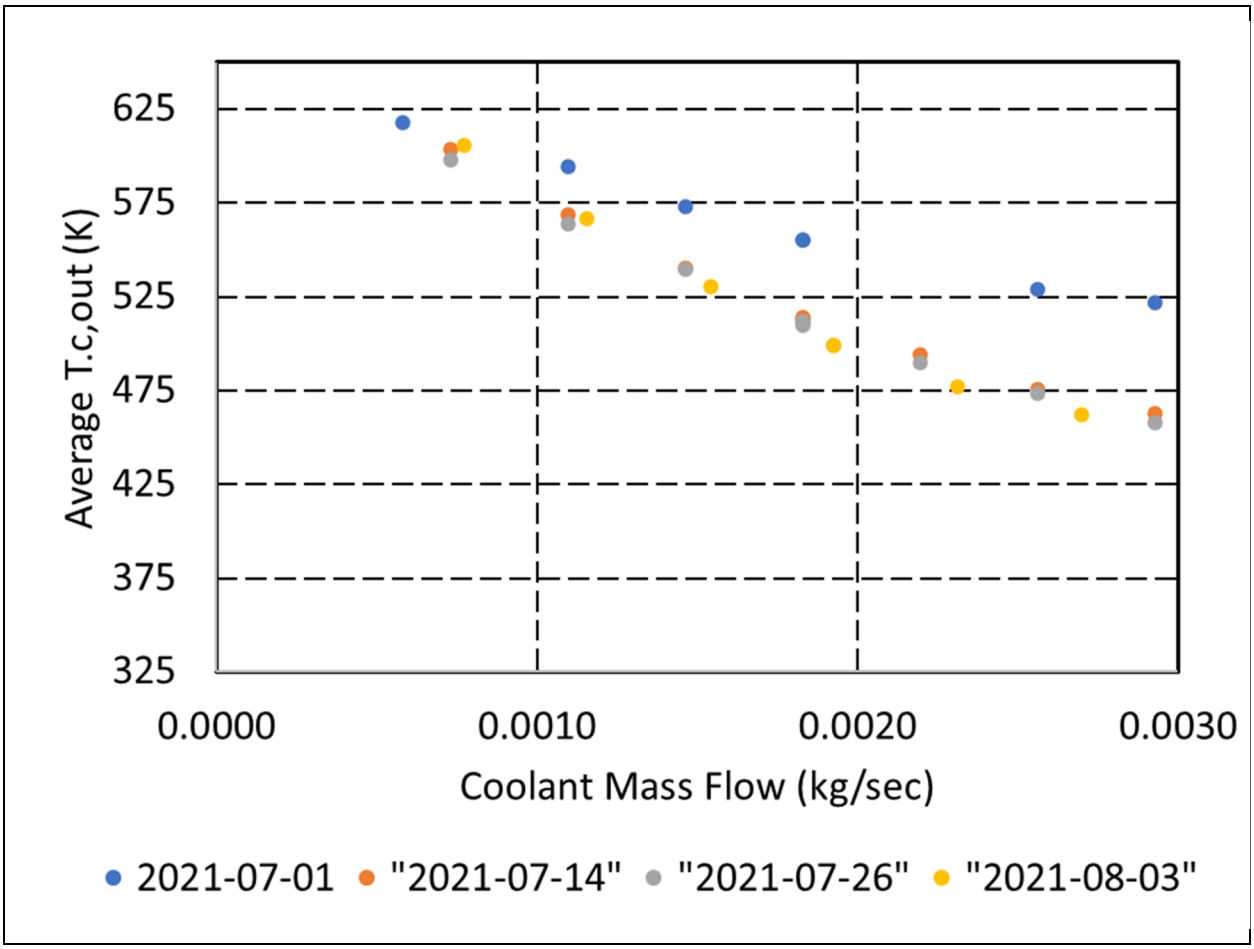

Figure 48: Measured variation in weighted average coolant exit temperature as a function of coolant flow rate.

4.5.2 Summary of Internal Cooling Efficiency Measurements

In Table 13, the calculated internal cooling efficiency, η_c, was 0.81. This value seems higher than expected based on NETL's Gas Turbine Handbook (Cunha, 2006). Furthermore, an even larger problem emerges when the entire dataset was considered. The average airfoil surface temperature which was used in the calculation of internal cooling efficiency was significantly higher than the measured coolant outlet temperatures, particularly for the lower coolant flows (see Figure 49). This resulted in $\eta_c \gg 1.0$ for many data points.

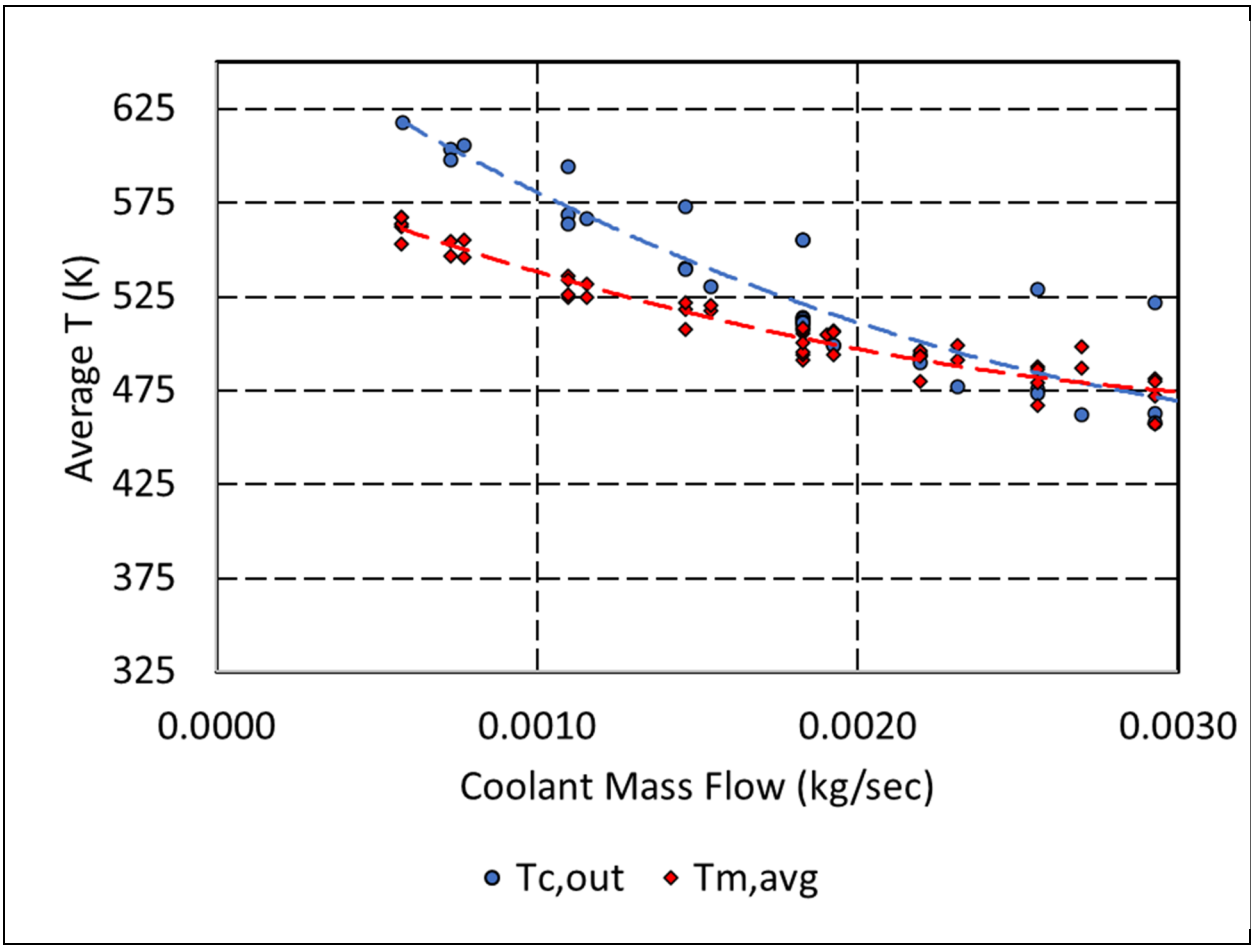

Figure 49: Average airfoil wall temperature and average coolant outlet temperatures as a function of coolant flow rate.

Upon further investigation, one of the underlying assumptions in the definition of internal cooling efficiency (i.e., Equation 40) was an infinite thermal conductivity (Holland and Thake, 1980). This assumption also implies a constant wall temperature over the surface of the airfoil. In this experiment, the airfoil surface temperature was not uniform. Furthermore, the amount of heat transferred to the coolant based on the measured coolant outlet temperature was significantly larger than the amount of heat theoretically transferred from the hot gas to the airfoil surface. In some cases, the increase in coolant temperature was 1.7 times larger than expected.

$$Q = \frac{\left(T_{\infty} - T_{m,avg}\right)}{R_{hot}} = \dot{m}c_p\left(T_{c,out} - T_{c,in}\right) \tag{44}$$

$$\left(T_{c,out} - T_{c,in}\right) = \frac{\left(T_{\infty} - T_{m,avg}\right)}{\dot{m}c_p R_{hot}} = \frac{\left(T_{\infty} - T_{m,avg}\right)}{HLP} \tag{45}$$

Since the measured coolant outlet temperatures were too large to be realistic, an alternative method of quantifying internal cooling efficiency was needed. After examining some simplified non-uniform wall temperature models that were previously developed at NETL for a different study, a modified relation for the internal cooling efficiency was derived. This modified relation agreed to within 5% of an alternative form of the internal cooling efficiency parameter that has been widely published, as shown in Equation 46. The NETL team decided to use the widely published internal cooling efficiency relation (Equation 46) for reporting internal cooling efficiencies, instead of using the average wall temperature and an average coolant outlet temperature (Equation 40). It is important to note that the overall cooling effectiveness term in Equation 46, ϕ_{avg}, was the average overall cooling effectiveness as defined in Equation 11 of this section, and HLP was the HLP as described in Equation 12 of this section.

$$\eta_c = \frac{\phi_{avg}}{HLP \cdot \left(1 - \phi_{avg}\right)} \tag{46}$$

For the remainder of this report, the internal cooling efficiency will be calculated using the relation listed in Equation 46, instead of Equation 40. Figure 50 shows the internal cooling efficiency calculated based on Equation 46. The results shown in Figure 50 have not been corrected for variations in the background radiation. This correction, which accounts for day-to-day variations including the test cell ambient conditions, will be described in more detail in the following section.

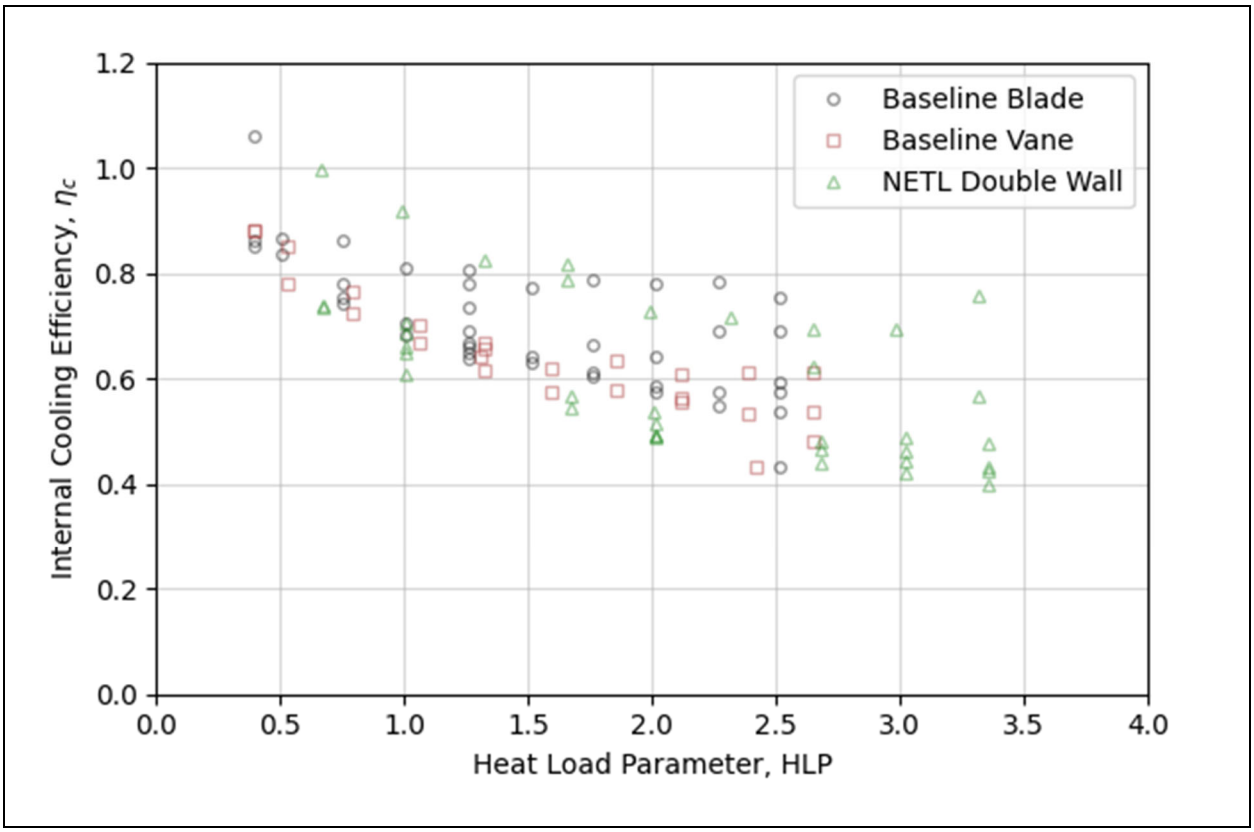

Figure 50: Internal convective cooling efficiency calculated using the raw average cooling effectiveness as described in Equation 46.

4.6 DATA ANALYSIS METHODS

4.6.1 Correction for Background IR Variations

The cooling response of various airfoil designs were tested over a period of 9 months (Figure 50). Certain airfoil designs were tested on multiple occasions. The average airfoil surface temperature, as computed from the IR images, varied from roughly 420 to 580 K. A large part of this variation was due to intentional variations in coolant flow rate and the different internal cooling designs. The remaining variation could have been due to any number of uncontrolled factors such as ambient temperature, humidity, changes in the black lining of the test section walls due to aging and oxidation of the paint, intentional and unintentional changes in the windows from test to test, changes in fitting the external insulation, etc. A major assumption in the IR analysis method discussed previously was that all these "other" factors remain constant during a test run and from test to test, so there is no significant impact on the IR images that were collected over all the days of testing.

One method of investigating this consistency is to examine the IR signal from the test section wall, which should hypothetically remain constant. The IR images of the airfoils included the test section wall "behind" the airfoil. A spot was selected upstream of the airfoil near the mid-point of the airfoil span. The IR signal was averaged over this spot and the average was then converted to an "effective" temperature. This temperature was deemed an "effective" temperature because

the "spot" was not located in the same focal plane as the airfoil, and because the in-situ calibration results did not necessarily apply to this spot on the opposite test section wall. This effective temperature was not expected to be an accurate indication of the wall temperature, but it was a convenient conversion of the raw IR signal to an approximate temperature and a useful proxy to represent test-to-test variations. These effective wall temperatures were also included in Figure 51. They were not constant and varied from 534 to 600 K. On run dates when the effective wall temperature was lower than average, the airfoil surface temperatures also appear to be lower than average. Therefore, a correlation between the airfoil surface temperature and the effective wall temperature was investigated.

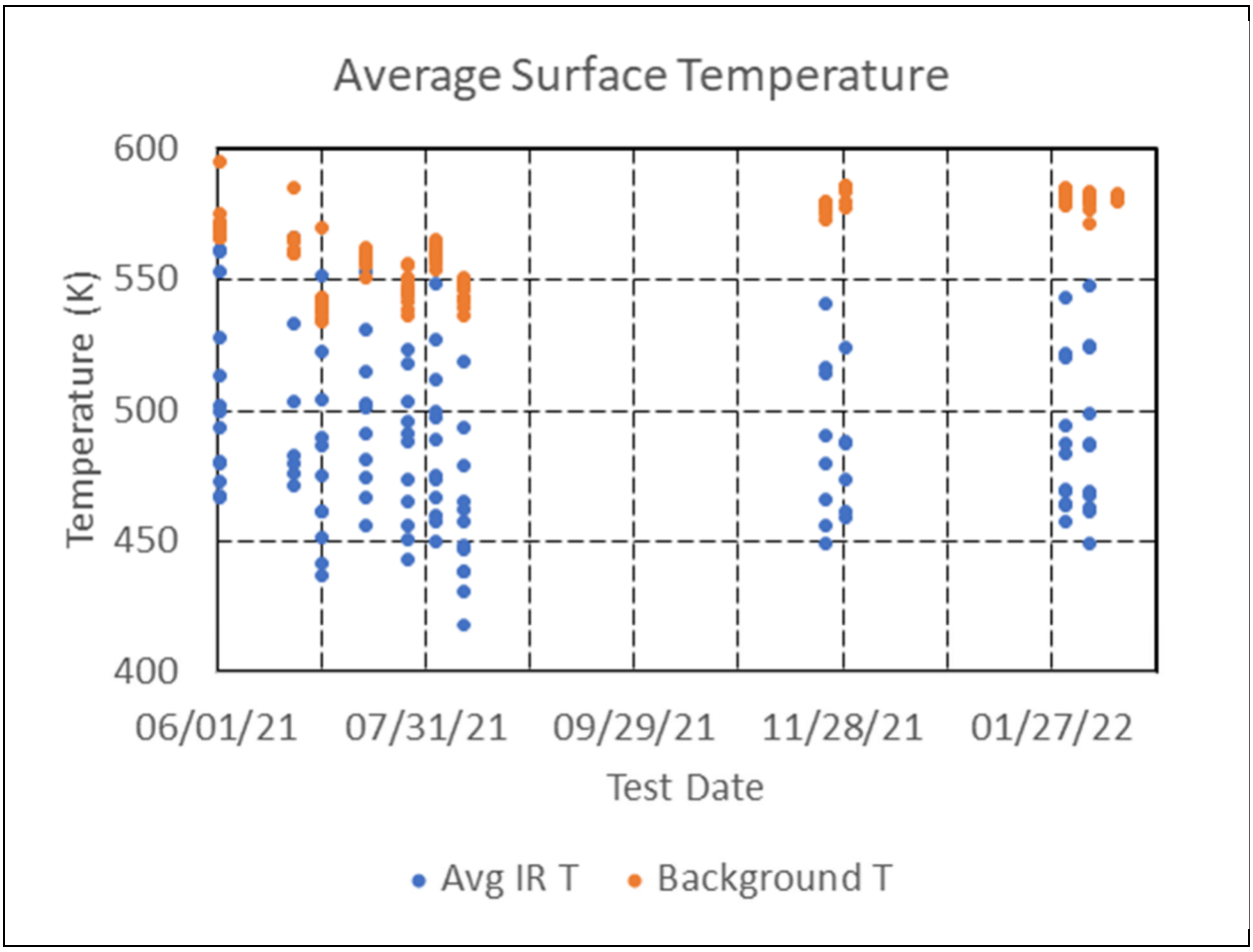

Figure 51: Variations in background temperature as a function of test date.

A more quantitative analysis of the average IR temperature of the airfoil surface demonstrated the relationship with background temperature more clearly. Experience with cooled flat plate and cooled airfoil surfaces, plus other simple modeling efforts, suggested that the average temperature over the whole surface (or any other cooled surface) varied linearly with the log of the HLP. A demonstration of this linear relationship has been shown in Figure 52 for the baseline blade design. A general regression-style quantitative model for this relationship can be written as:

$$T_{i,j,k} = \beta_{0,i} + \beta_{1,i} \cdot \ln\left(HLP_{i,j,k}\right) + e_{i,j,k} \quad (47)$$

where

$T_{i,j,k}$ is the Average Surface Temperature of the ith airfoil design at the jth HLP and the kth replicate,

$\beta_{0,i}$ is the intercept for the ith airfoil design,

$\beta_{1,i}$ is the slope for the ith airfoil design,

$HLP_{i,j,k}$ is the HLP value for the ith airfoil design at the jth HLP and the kth replicate, and

$e_{i,j,k}$ is the "residual" or deviation from the line for the ith airfoil design at the jth HLP and the kth replicate.

The slope and intercept terms ($\beta_{0,i}$ and $\beta_{1,i}$) were estimated via standard regression analysis. The regression residuals (an estimate of $e_{i,j,k}$) were plotted vs. background effective temperature in Figure 53. These results confirmed a correlation with background temperature, however, the residuals were also correlated with the background "effective" temperature. The positive residuals were associated with larger background temperatures and vice versa. This suggests that the "model" may be more precise if background temperature was included, as shown in the following model (Equation 48).

$$T_{i,j,k} = \beta_{0,i} + \beta_{1,i} \cdot \ln\left(HLP_{i,j,k}\right) + \beta_2 \cdot T_{b,i,j,k} + e_{i,j,k} \quad (48)$$

where:

β_2 is the slope for background temperature and

$T_{b,i,j,k}$ is the background temperature for the ith airfoil design at the jth HLP and the kth replicate.

The extra slope term, β_2, can be estimated by repeating the previous regression and including background temperature as another independent variable. The results can be applied to address the question of what the airfoil surface temperature would have been if the background surface temperature had been held constant at a certain value. This question was relevant to addressing an unbiased comparison among the various airfoil designs.

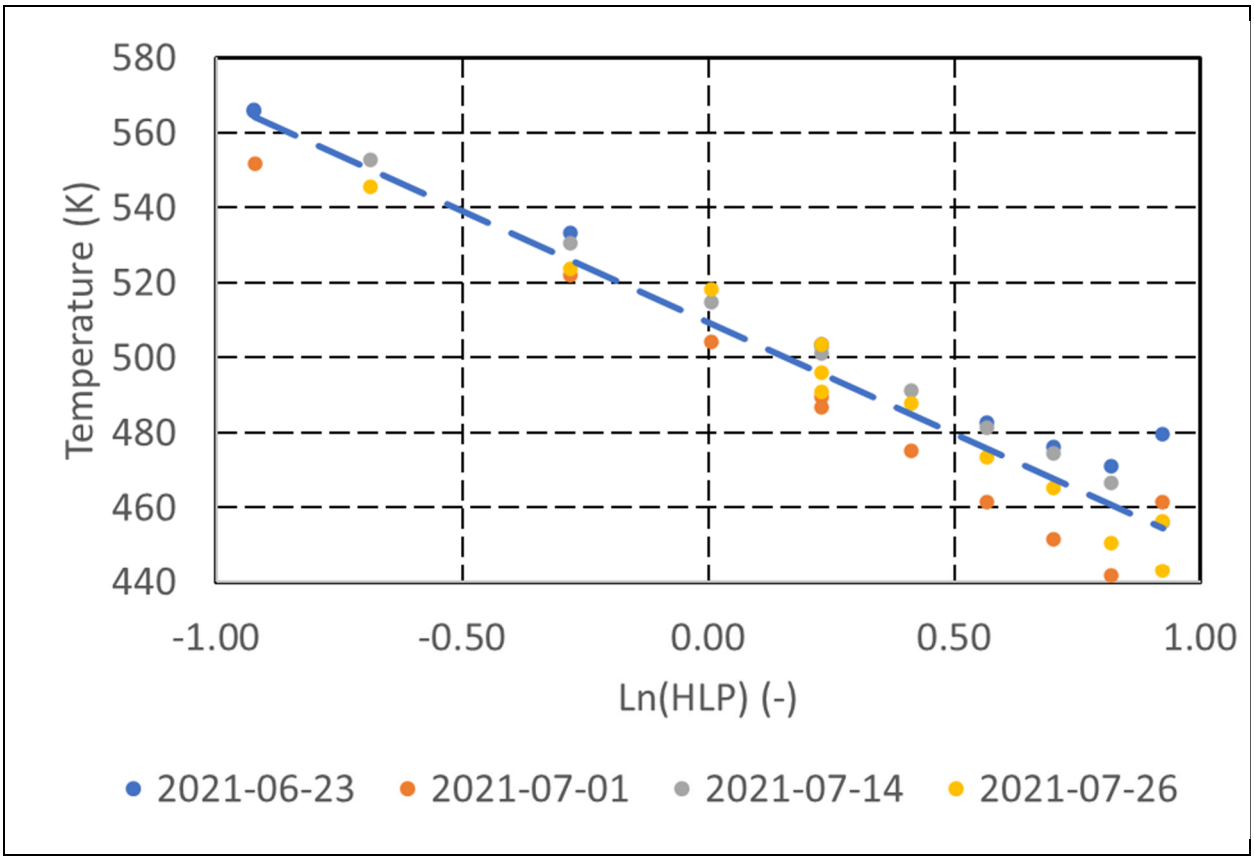

Figure 52: Average airfoil surface temperature as a logarithmic function of the HLP for the baseline blade design

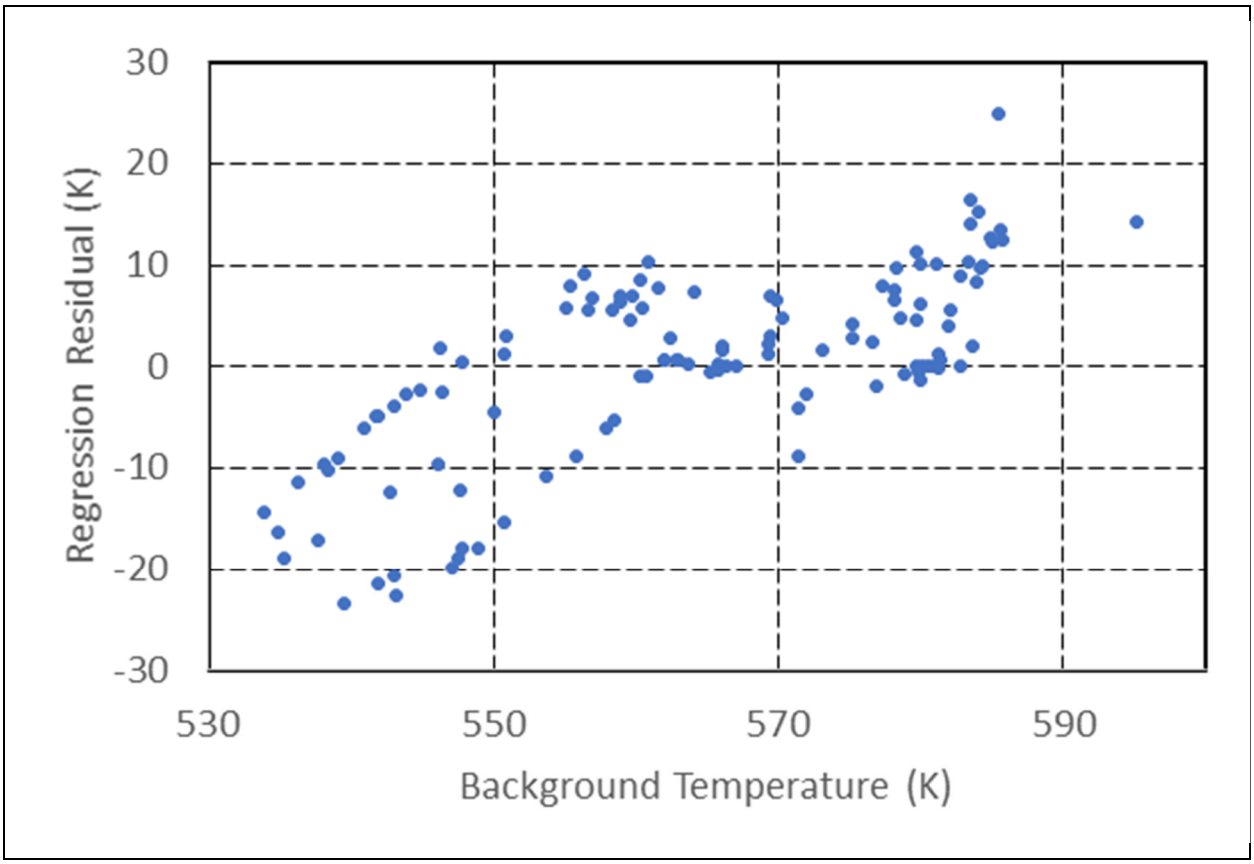

Figure 53: Regression residual plotted against the background "effective" temperature.

Consider the impact of subtracting $\beta_2 \cdot (T_{b,i,j,k} - T_{b0})$ from $T_{i,j,k}$, where T_{b0} represents the value at which the background temperature "should" have been (e.g., the average background temperature). Applying this subtraction to the regression model yields (Equation 49):

$$\begin{aligned} T_{i,j,k} - \beta_2 (T_{b,i,j,k} - T_{b0}) \\ = \beta_{0,i} + \beta_{1,i} \cdot \ln(HLP_{i,j,k}) + \beta_2 \cdot T_{b,i,j,k} + e_{i,j,k} \\ - \beta_2 (T_{b,i,j,k} - T_{b0}) \end{aligned} \quad (49)$$

$$T_{i,j,k} - \beta_2 (T_{b,i,j,k} - T_{b0}) = \beta_{0,i} + \beta_{1,i} \cdot \ln(HLP_{i,j,k}) + \beta_2 T_{b0} + e_{i,j,k} \quad (50)$$

Note that the contribution of background temperature to the quantity $T_{i,j,k} - \beta_2 \cdot (T_{b,i,j,k} - T_{b0})$ is a constant. Therefore, subtraction of $\beta_2 (T_{b,i,j,k} - T_{b0})$ adjusts the measured IR temperature to an approximation of what it would have been if the background temperature had been held constant at T_{b0}. This forms the basis of the adjustment that was applied to the measured IR images in this report to account for day-to-day variations in the background surrounding wall temperatures. The multiple regression needed to estimate β_2 for this correction is akin to a

statistical method known as analysis of covariance. The result of this correction for the baseline airfoil design can been seen in Figure 54. By comparing Figure 54 to the regression in Figure 52, a clear improvement in the regression is seen when the regression model is included the β_2 term. The reduction in scatter is apparent.

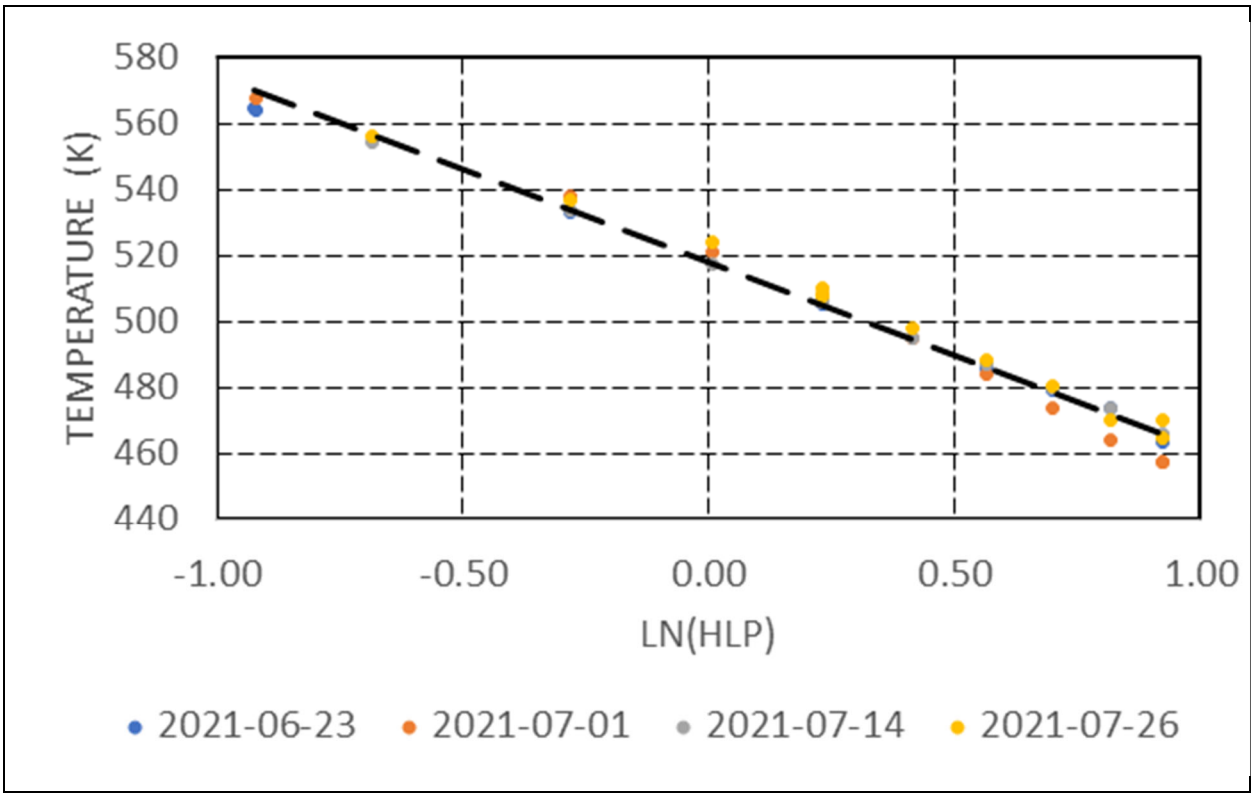

Figure 54: Average temperatures of baseline blade corrected for background radiation (includes β_2 term in the regression model).

4.6.2 Summary of Analysis of Covariance

The correction for a constant background temperature was made to the average airfoil surface temperature and to the 99th percentile surface temperature for every data point covering all the various airfoil geometries. The resulting dataset was too large to include in this report, but the R-squared value for both multiple regressions exceeded 99%. Residual standard errors were less than 3 K for both cases and this was consistent with the uncertainties in the temperature measurements. Average cooling effectiveness and internal convective cooling efficiencies were computed from the adjusted average surface temperatures. To illustrate the effect of this correction, both the corrected and uncorrected internal convective cooling efficiency data have been plotted in Figure 55 below . The corrections for day-to-day variations in background temperature significantly reduced the scatter in the experimental measurements.

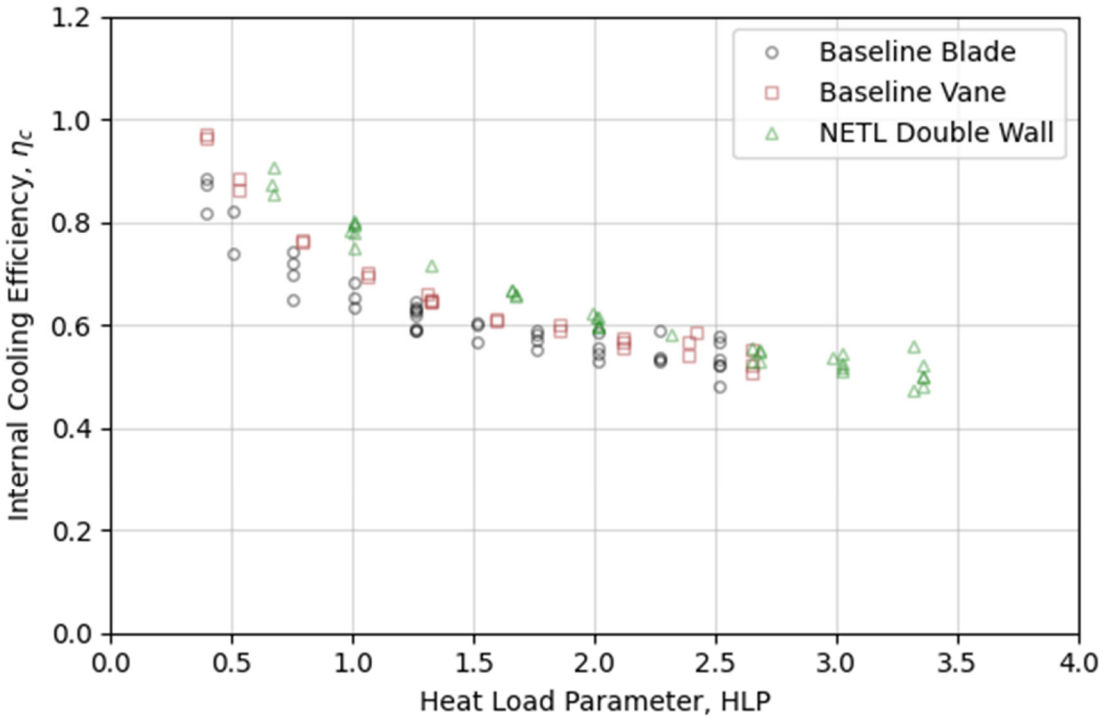

(a) Corrected Using Analysis of Covariance

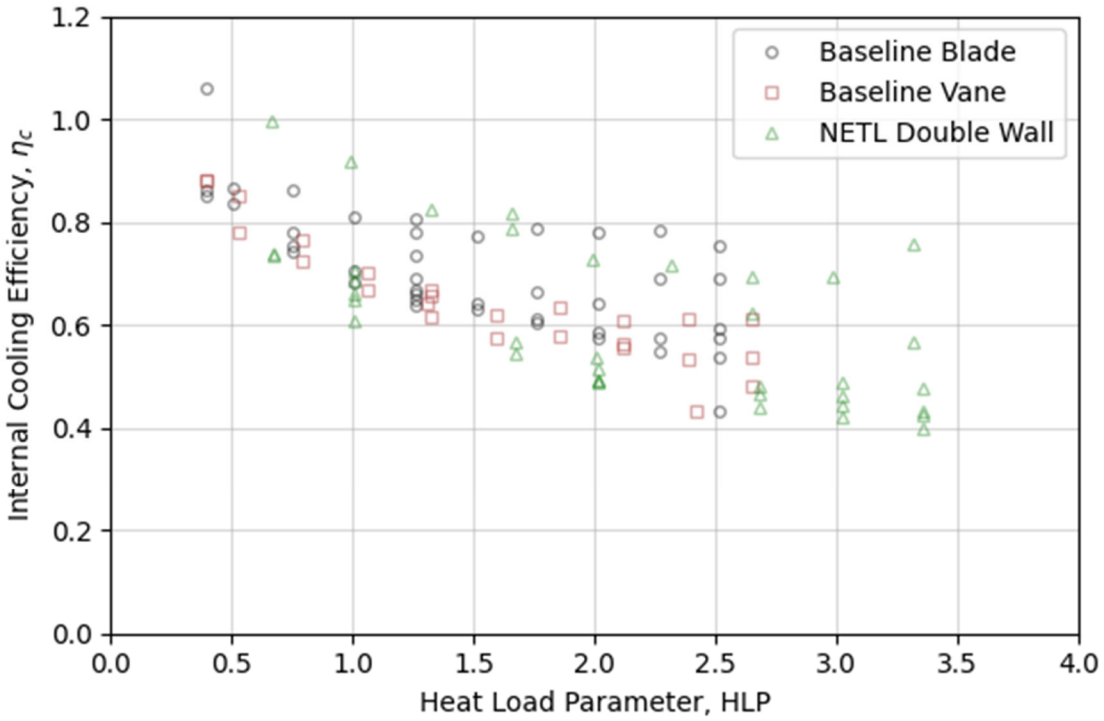

(b) Uncorrected Data

Figure 55: Internal convective cooling efficiency (a) with and (b) without corrections using an analysis of covariance.

5. RESULTS AND DISCUSSION

5.1 SURFACE TEMPERATURE CONTOURS

Figure 56 shows the surface temperature distribution for each of the internally cooled airfoil designs at two different cooling air flowrates (i.e., HLP=1 and HLP=2). One replication has been shown at each condition. The microchannel design has not been included in Figure 56 because the pressure drop through this airfoil design was too high to achieve these cooling air flow rates.

All the designs are cooler in the mid-chord region where the heat load is lower, and hotter near the leading edge and the trailing edge. For the baseline vane, localized cold spots were observed in the mid-chord region. These localized cooler regions were caused by the internal impingement jet cooling. These temperature gradients have the potential to introduce thermal stresses for rotor blades. As previously described in Section 3.9, the incremental impingement double-wall design also used internal impingement jet cooling, but the cold spots were not observed in the incremental impingement design. One possible explanation for this difference involved the thermal conductivity path provided by the pedestal array, but other factors could have also caused these differences.

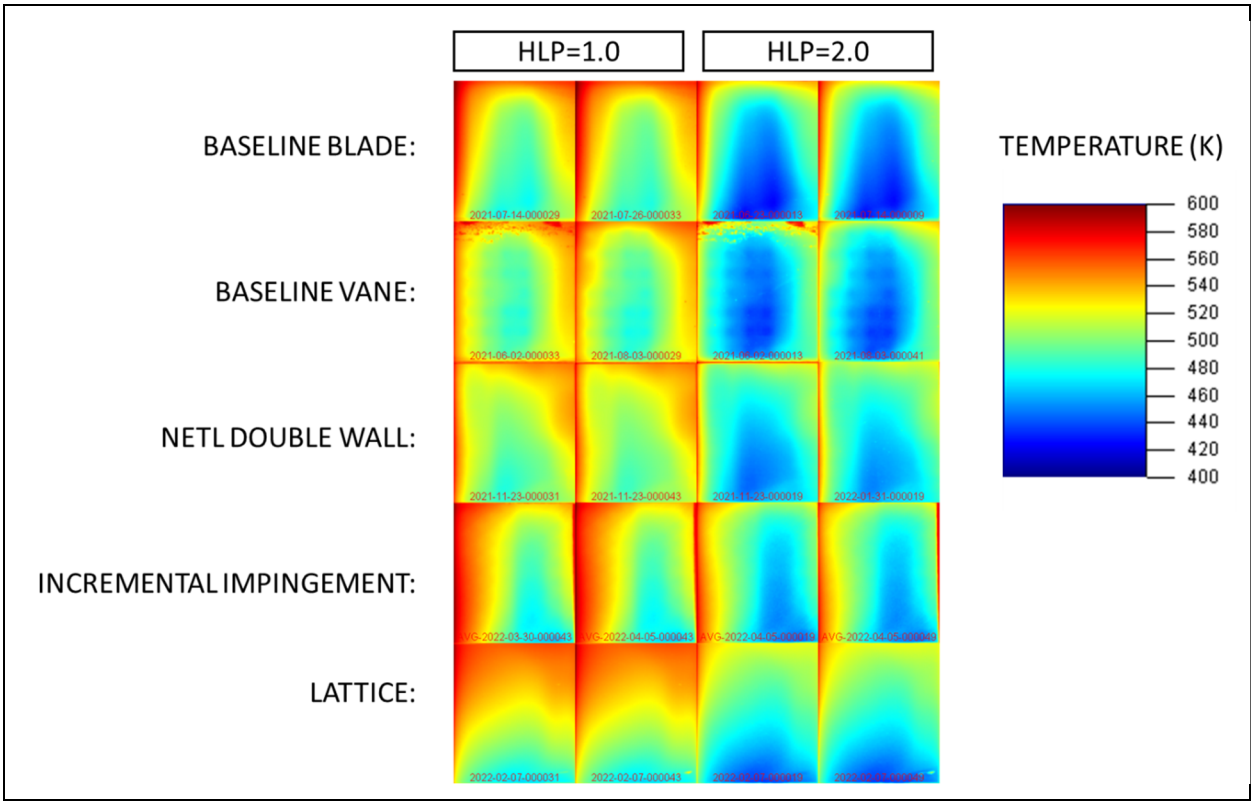

Figure 56: IR surface temperature contours for each airfoil cooling design at cooling flows equivalent to HLP=1 and HLP=2. Note one replication has been shown for each condition.

Figure 57 below shows regionally averaged surface temperature for each of the different internally cooled airfoil designs. The largest variations were observed in the leading-edge region.

For a given cooling air flow, or HLP, the NETL double-wall design consistently performed better than the other designs in the leading edge. The lattice design also performed very well on an average temperature basis. Both of these designs had a significant amount of internal surface area that provided conductive cooling paths, like classical heat transfer fins. The incremental impingement design also had a significant amount of surface area provided by the pedestal array. However, the incremental impingement design did not provide effective cooling for the leading edge, and the temperatures were much hotter than expected for this design. Post-test inspection of the incremental impingement design revealed some internal cooling air leakage between the leading edge coolant plenum and the trailing edge coolant supply plenum. The cooling air flow for the leading edge was also restricted by the relatively small cross-sectional area in the coolant ejection slot at the tip. This internal leakage issue impacted the cooling performance and this design should be revisited in future efforts.

The incremental impingement airfoil design was modified to: 1) increase the area of the coolant ejection slot, 2) allow AM powder clean-out passages that extend through the base of the airfoil, and 3) allow more effective sealing between the coolant supply plenums. This revised incremental impingement cooling design was not fabricated and tested prior to this report. Therefore, only the results for the first-generation incremental impingement design have been discussed in this report.

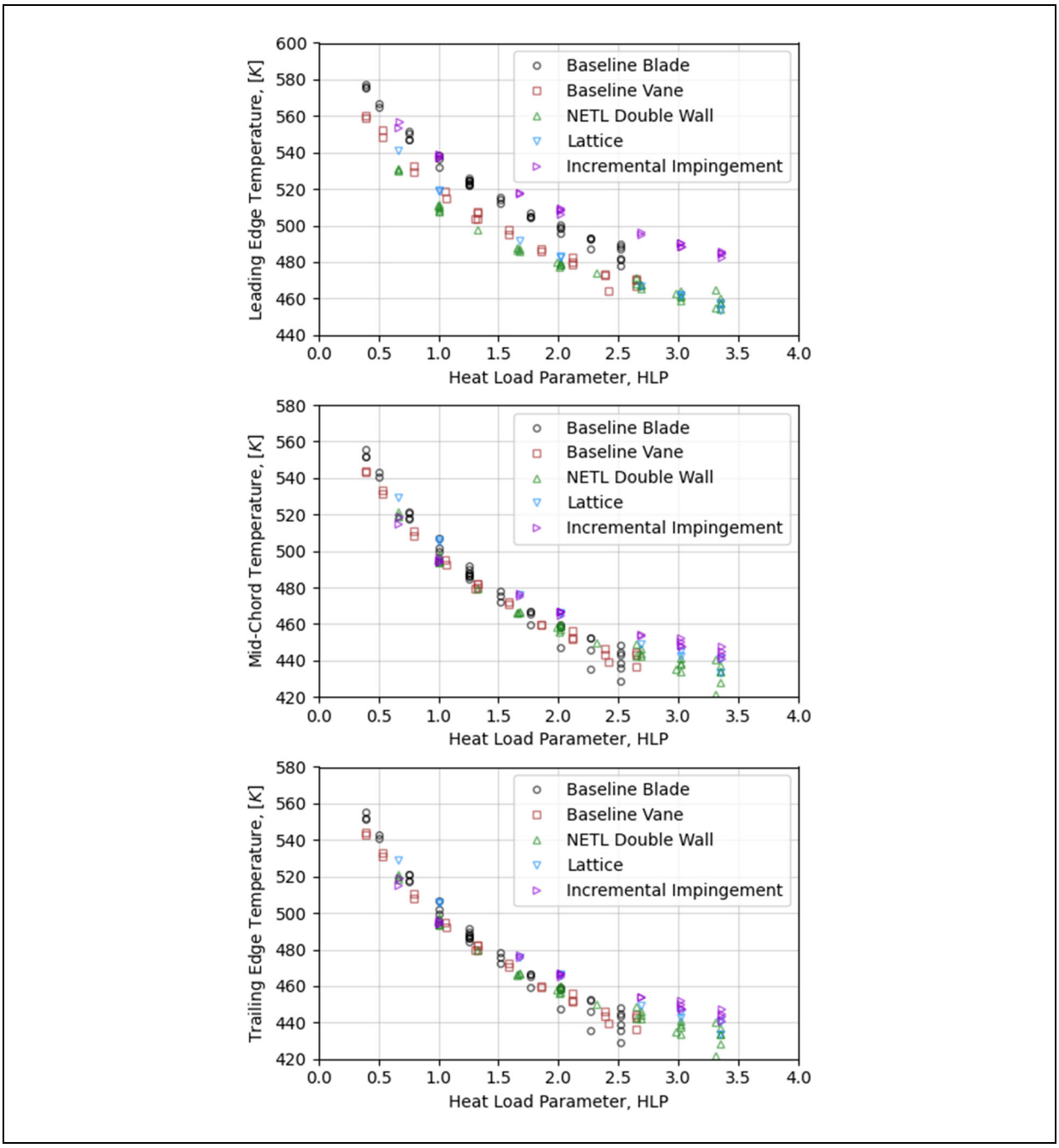

Figure 57: Average surface temperatures measured in the leading edge, mid-chord region, and trailing edge region for each test condition and cooling configuration.

5.2 COOLING TECHNOLOGY CURVES

As previously described in Section 4.1, cooling technology curves have been widely used in the literature to describe conceptual cooling concepts. The term "cooling technology curve" has been used to describe the relationship between an overall cooling effectiveness parameter, ϕ, and a non-dimensional cooling flow rate, or HLP. To the authors' knowledge, no prior efforts have presented experimentally measured cooling technology curves for an entire airfoil cooling architecture. In this section, results from experimental measurements for both the overall cooling effectiveness, ϕ, and the internal cooling efficiency, η_c, as a function of HLP will be presented.

5.2.1 Analysis of Overall Cooling Effectiveness, ϕ

The overall cooling effectiveness, as defined in Equation 11, is a key performance index of the cooling design. It is also a non-dimensional wall temperature, so the overall cooling effectiveness can vary between zero and one. In this section, two different variations of Equation 11 have been used. The first variation was the conventional approach in which the external wall temperature was used in Equation 11. If the average wall temperature was used, the quantity was denoted as the average overall cooling effectiveness, ϕ_{Avg}. In the second variation, the 99th percentile external wall temperature was calculated for each test condition and cooling design. This cooling effectiveness value was denoted ϕ_{99}. This ϕ_{99} value was interpreted as the cooling effectiveness at which 99% of the airfoil surface had a local cooling effectiveness that was higher than ϕ_{99}. This second variation produces a more conservative curve that could be more useful than ϕ_{Avg}, from a design perspective.

Figure 58 shows the cooling technology curves for four different cooling designs. The symbols in this figure represent the measured experimental data for several different days of testing. The lines represent curve fits to the experimental data. The non-shaded (white) region in this figure represents cooling performance that is lower than the current state-of-the-art (i.e., $\phi < 0.28$). The shaded (blue) region between 0.28 and 0.37 represents cooling performance that is better than the minimum requirement for the current state-of-the-art, but less than the goal for this project. The shaded (orange) region above 0.37 represents the advanced goal for this project. The basis for these cooling performance targets was described in Section 3.3, and Table 14 summarizes these cooling performance targets.

The trendlines through the experimental data points ϕ_{Avg} and ϕ_{99} represent linear regressions with respect to the natural log of the HLP. Each of these regression lines were represented by a slope and intercept as shown in Equation 51 and 52. The regression coefficients for these performance curves have been listed in Table 15.

$$\widehat{\phi_{avg}} = \beta_{0,avg} + \beta_{1,avg}\, Ln(HLP) \tag{51}$$

$$\widehat{\phi_{99}} = \beta_0 + \beta_1\, Ln(HLP) \tag{52}$$

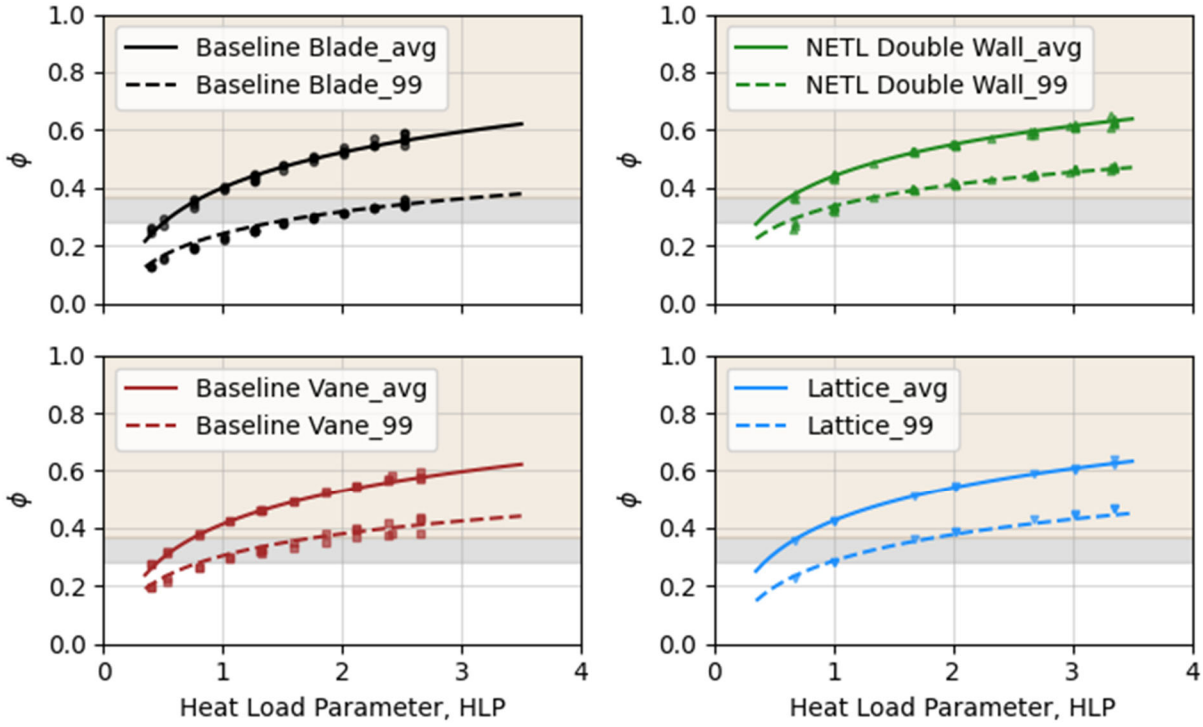

Figure 58: Experimentally measured cooling technology curves (ϕ_{Avg} and ϕ_{99}) for the baseline blade, baseline vane, NETL double-wall, and lattice designs.

Table 14: Baseline and Advanced Turbine Cooling Conditions

Parameter	Baseline Conditions		Advanced Conditions	
	Engine	Test Rig	Engine	Test Rig
Hot gas temperature (K)	1,366	650	1,466	650
Coolant inlet temperature (K)	685	325	685	325
Maximum metal temperature (K)	1,178	560	1,178	530
Minimum cooling effectiveness, $\phi_{\min}$ (-)	0.28	0.28	0.37	0.37

Table 15: Regression Coefficients for Cooling Technology Curves for each Airfoil Cooling Design and Minimum HLP

Cooling Design	ϕ_{Avg}		ϕ_{99}		Minimum HLP	
	$\beta_{0,avg}$	$\beta_{1,avg}$	β_0	β_1	Baseline	Advanced
Baseline blade	0.400	0.176	0.241	0.110	1.38	3.22
Baseline vane	0.413	0.167	0.304	0.109	0.77	1.81
NETL double-wall	0.440	0.158	0.336	0.107	0.57	1.36
Lattice	0.425	0.166	0.286	0.131	0.93	1.89
Incremental impingement	0.428	0.137	0.250	0.115	1.26	2.83

5.2.2 Analysis of Minimum Cooling Flow Requirement (HLP_{min})

One method to rank these different designs is to define a minimum cooling flow requirement, or minimum HLP. The minimum cooling flow requirement can be determined using the cooling technology curves described in the previous section (i.e., $\phi_{99}\ vs.\ HLP$) and the overall cooling effectiveness targets described in Table 14. Consider the cooling technology curves for the baseline blade shown in the Figure 59 below . The intersection of the current state-of-the-art cooling target, $\phi_{base} = 0.28$, and the regression line for ϕ_{99} occurred at an HLP of approximately 1.4. This intersection represented the minimum cooling mass flow rate at which 99% of the blade surface was at or below the maximum working temperature. To achieve the more advanced goal of increasing the turbine-inlet-temperature by 100 K while maintaining the limit on blade surface temperature, the cooling effectiveness target in this example needs to increase to $\phi_{adv} = 0.37$. Extending the regression line for ϕ_{99} until this curve intersects the advanced cooling target ($\phi_{adv} = 0.37$), this airfoil cooling design could operate at the advanced cooling target by increasing the non-dimensional coolant flow rate, or HLP, to a value of 3.1. In other words, to increase the hot gas path temperature by 100 K and still maintain 99% of the airfoil surface at or below the maximum wall temperature, the coolant flow rate for the baseline blade would need to increase by a factor of 2.2 (i.e., $^{3.1}/_{1.4}$). Depending on the cooling design that is used, these minimum cooling flow requirements can change.

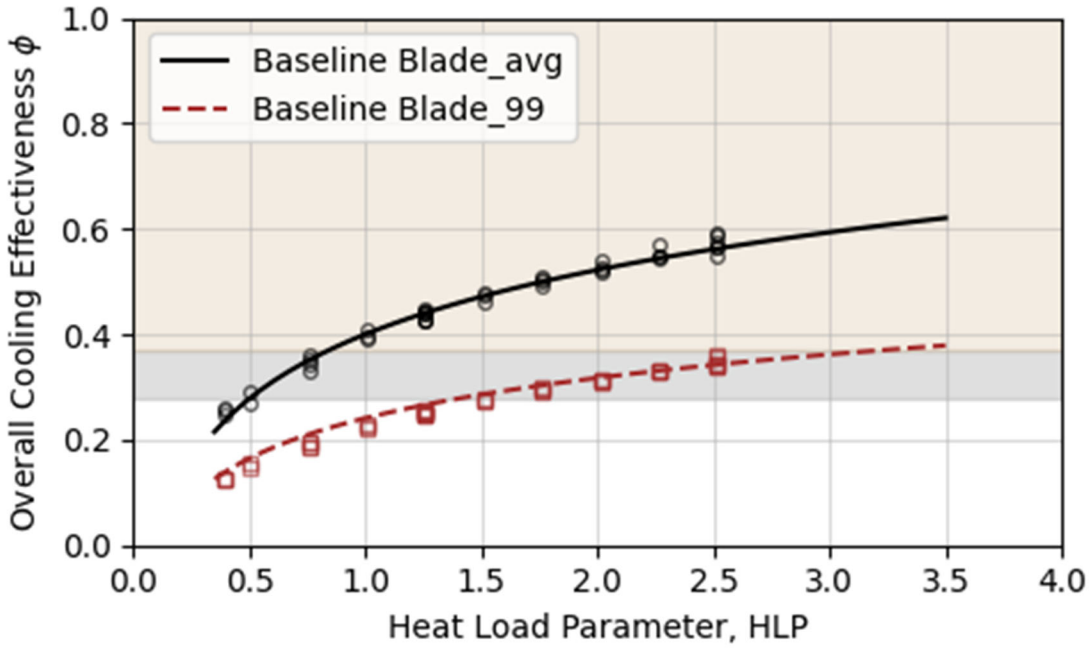

Figure 59: Technology curve used for finding minimum HLP for the baseline blade (ϕ_{Avg} and ϕ_{99}).

In Table 15 above, the minimum non-dimensional cooling flow, or HLP, has been listed for the baseline and the advanced cooling targets for each cooling design. For the baseline cooling performance objective, the baseline blade required the most cooling flow and the NETL double-wall design required the least amount of cooling flow. At the advanced cooling performance objective, this relative ranking is the same. These results also suggest that the NETL double-wall design could achieve the advanced cooling performance metric with the same cooling air flow that the baseline blade requires for the current state-of-the-art. This is a significant improvement.

In order to provide a better comparison between the different cooling designs, Figure 60 below shows all of the cooling technology curves on the same plot. In Figure 60a, the 99th percentile cooling effectiveness curves have been used to identify the minimum HLP values listed in the table above. By comparing the baseline blade (black) line and the NETL double-wall (green) curves, the relative difference in cooling effectiveness for a constant HLP was approximately 0.1, or approximately 100 K at engine conditions.

In Figure 60b, the average overall cooling effectiveness values were very similar and some differences can be observed when the curves were compared at low HLP and high HLP. For example, the incremental impingement design seems to perform better than the other designs at the lower HLP, but was less effective relative to the other designs at the higher HLP conditions. These averaged overall cooling effectiveness curves were used to calculate internal cooling efficiency curves which will be described in the next section.

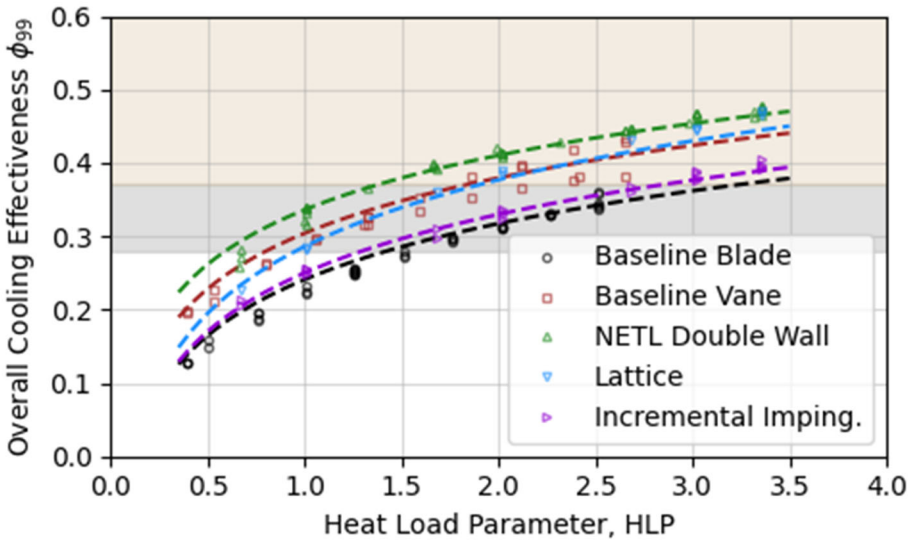

(a)

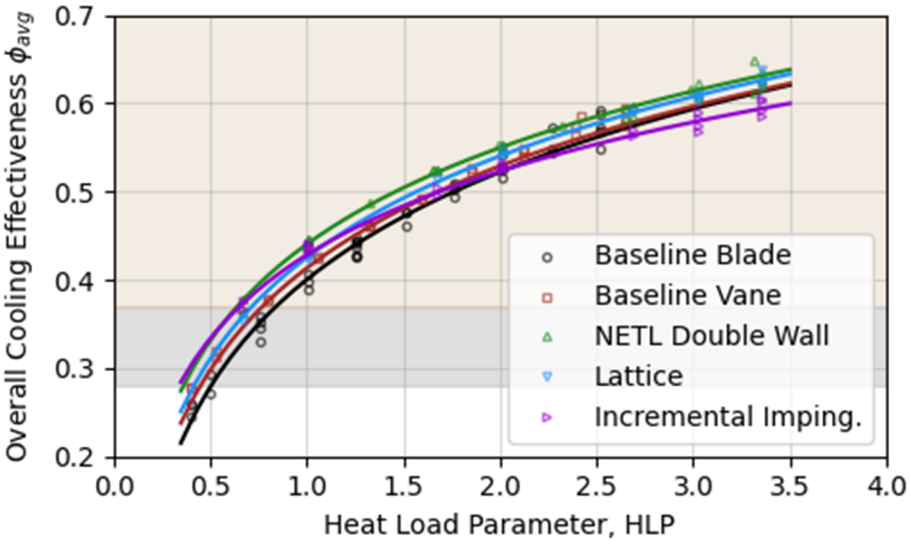

(b)

Figure 60: Plots of ϕ_{99} and ϕ_{avg} vs. HLP for each airfoil considered: (a) 99th percentile for overall cooling effectiveness, and (b) shows the average overall cooling effectiveness.

5.3 INTERNAL CONVECTIVE COOLING EFFICIENCY CURVES, η_c

As described in Section 4.1, the internal convective cooling efficiency, η_c, can be calculated from the average cooling effectiveness and the measured HLP (see Equation 14). In Table 15 in Section 5.2, the minimum HLP for each internal cooling design was determined for the baseline and the advanced cooling effectiveness targets. Table 16 below lists these minimum HLP conditions and the corresponding average overall cooling effectiveness. Table 16 also lists the corresponding internal convective cooling efficiency at this minimum HLP.

Table 16: Convective Internal Cooling Efficiency Values for each Airfoil Cooling Design Considered and both Baseline $\phi_{base} = 0.28$ and Advanced Cooling $\phi_{adv} = 0.37$ Targets.

Cooling Design	Minimum HLP		Cooling Effectiveness ϕ_{Avg}		Internal Cooling Efficiency η_c	
	Baseline	Advanced	Baseline	Advanced	Baseline	Advanced
Baseline blade	1.38	3.22	0.46	0.61	0.61	0.48
Baseline vane	0.77	1.81	0.37	0.51	0.76	0.58
NETL double-wall	0.57	1.36	0.35	0.49	0.95	0.70
Lattice	0.93	1.89	0.41	0.53	0.76	0.60
Incremental impingement	1.26	2.83	0.46	0.57	0.67	0.47

When comparing the performance of an advanced cooling design with that of a baseline design, it is not sufficient that the advanced design be capable of operating at the advanced conditions. It must also be capable of achieving the advanced operating conditions at an internal cooling efficiency that is equal, or greater than, the baseline. For example, for the baseline blade, the corresponding internal convective cooling efficiency, η_c, would decrease from 0.61 to 0.48 to accommodate the advanced cooling design target (i.e., 100 K above the baseline). This increase in coolant flow would be accompanied by loss of turbine efficiency as described in Section 2.4. On the other hand, for the NETL double-wall design, the internal convective cooling efficiency would decrease from 0.95 to 0.70 to accommodate the higher turbine inlet temperature. Based on these test results, the NETL double-wall design could achieve the advanced overall cooling effectiveness target at roughly the same coolant flow rate and also achieve an internal cooling efficiency that is almost 10 percentage points higher than the baseline blade at the current state-of-the-art.

Figure 61 below shows the measured internal cooling efficiency curves for each of the airfoil cooling designs considered in this study. The incremental impingement design, the NETL double-wall and the lattice designs had the highest internal convective cooling efficiencies at the lowest cooling flow (low HLP). At the higher HLP (higher cooling air flow), all the designs have an internal cooling efficiency in the 0.40–0.50 range. The previous section described how the minimum HLP was different for each design. The minimum HLP is dependent on the 99th percentile cooling effectiveness curve, $\boldsymbol{\phi_{99}}$, and the overall cooling effectiveness target (i.e., baseline or advanced). These performance values were listed in Table 15 and Table 16. At the advanced cooling design target, the highest internal cooling efficiency was 0.70 (NETL double-wall) and the lowest was 0.47 (incremental impingement design). As previously described in Section 5.1, some internal leakage was present in the incremental impingement design. This airfoil has been redesigned, but data for this second generation incremental impingement airfoil was not available at the time of this final report.

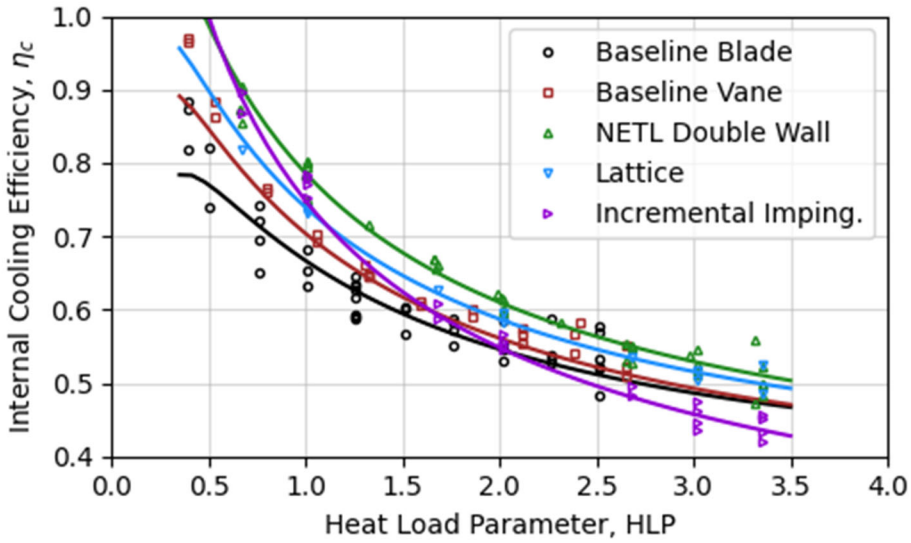

Figure 61: Internal convective cooling efficiency curves vs. HLP for each of the different airfoil cooling designs.

6. SUMMARY AND CONCLUSIONS

This report describes an effort to use AM technologies and advanced airfoil cooling designs to increase the turbine inlet temperature by 100 °C for small gas turbines typically used in CHP systems. At the beginning of this effort, baseline performance data for small (5–10 MW) gas turbines was not available, and the potential benefits of cooling system improvements for small gas turbines were not quantified in the literature.

The findings and conclusions from this study are outlined below:

- A public baseline engine model for a small (5–10MW) gas turbine combined with a steam heat recovery steam generator with and without a bottoming steam turbine was developed and disseminated (see Section 2.1 and Uysal et al., 2021).
    - Increasing the turbine inlet temperature by 100 °C with no improvement in cooling technology could increase the gas turbine efficiency by 1 percentage point relative to a 33% baseline.
    - If the internal cooling efficiency is increased from 0.62 (baseline) to 0.7 and the firing temperature is increased by 100 °C,
        - The efficiency could be increased by 2 percentage points relative to a 33% baseline;
        - The power output could be increased by more than 20%; and
        - The steam capacity could be increased by more than 10%.
- A market and benefits analysis of increasing the firing temperature and increasing the cooling technology in a small (5–10 MW) gas turbine CHP system had the potential to reduce the pay-back period by roughly 1 year and reduce the cost of electricity by 7% (see Section 2.2).
- A unique test protocol was also developed and demonstrated for comparing these baseline cooling designs to other advanced concepts for an entire airfoil (see Section 2.4 and Straub et al., 2021).
- Baseline cooling designs were developed for the first stage vane and the first stage blade in a small (5–10 MW) gas turbine application (see Section 3, and Straub et al., 2021).
- Internally cooled airfoils were designed and additively manufactured using powder bed fusion technologies (see Section 3.4–3.9, and Straub et al., 2022).
- The study provided an opportunity to develop a detailed IR radiation imaging model for an airfoil surface and an approach to account for variations in the background temperature. Details of the approach have been included in Section 4.3.
- Testing was performed in the CAT rig at NETL. The heated wind tunnel test facility with independent cooling plenum enabled the airfoils to be tested at a hot gas path temperature of 650 K. Five airfoil designs (two baseline and three advanced) were integrated in a NACA-0024 profile (a public, symmetric shape) and additively manufactured. For each design, the overall cooling effectiveness across the airfoil surface was measured using IR imaging and correlation approach at varying HLP conditions. The findings from this experimental study can be summarized as follows:

- Both baseline blade and vane designs were tested. The advanced designs were compared to the baseline blade results as well as the baseline and advanced cooling targets.
- The NETL double-wall design had the highest performance overall (using 42% of the coolant required by the baseline blade at the advanced overall effectiveness target) and provided uniform cooling across the blade.
- The lattice design followed in performance, however, it is not recommended for further study because of strong temperature non-uniformity from base to tip resulting from the rise in coolant temperature as the coolant navigates the channels of the lattice.
- The incremental impingement design had the lowest performance of the three advanced designs and this was attributed to internal leakage between the coolant supply plenums. This airfoil has been redesigned and performance characteristics will be reported in a future work.
- Design for AM created some constraints on airfoil design which are relevant to the success of the airfoil concepts, such as the design to facilitate powder removal, definition of printable feature sizes, and preventing unallowable overhangs.

Future work should focus on increasing the technology readiness of the proposed airfoil cooling designs. A potential pathway for follow-on work would involve integrating these cooling concepts into a more realistic airfoil profile and testing these concepts at higher Reynold's Number conditions. The testing completed under this effort considered a symmetric airfoil (NACA-0024) profile at Reynold's Numbers (based on chord length) of 90,000. Future work should focus on Reynold's Numbers in the 900,000 to 1,500,000 range. A study of rotational effects on these advanced designs would also be recommended, since many of the advanced designs have potential cooling advantages over the baseline blade design in a rotating environment.

7. REFERENCES

ABB. ABB Velocity. 2020. https://new.abb.com/enterprise-software/energy-portfolio-management/market-intelligence-services/velocity-suite.

Airfoil Tools. www.airfoiltools.com/airfoil/naca4digit (accessed Oct 28, 2022).

Ames, F. E.; Nordquist, C. A.; Klennert, L. A. *Endwall Heat Transfer Measurements in a Staggered Pin Fin Array with an Adiabatic Pin*; ASME Paper GT2007-27432; 2007; pp. 423–432.

Appleyard, D. MGT Power Generation Packages Commissioned in China. *Gas Turbine World* **2019,** 18–21.

Aschenbruck, E.; Cagna, M.; Langusch, V.; Orth, U.; Spiegel, A.; Wiedermann, A.; Wiers, S.-H. *MAN's New Gas Turbines For Mechanical Drive and Power Generation Applications*; Proceedings from the ASME Turbo Expo 2013; *Turbo Expo: Power for Land, Sea, and Air,* 2013.

Bergholz, R. F. *Preliminary Design Optimization of Impingement Cooled Turbine Airfoils*; In ASME Paper GT2008-50704, Berlin, Germany, 2008; pp. 1–15.

Bons, J. P. A Review of Surface Roughness Effects in Gas Turbines. *Journal of Turbomachinery* **2010,** *132,* 1–16. https://doi.org/10.1115/1.3066315

Bunker, R. S. Cooling Design Analysis. In *The Gas Turbine Handbook*; National Energy Technology Laboratory (NETL), Pittsburgh, PA, Morgantown, WV, 2006; pp. 295–308.

Bunker, R. S. *Evolution of Turbine Cooling*; In ASME Paper GT2017-63025, 2017; pp. 1–26. https://doi.org/10.1115/GT2017-63205.

Bunker, R. S. *Gas Turbine Cooling: Moving from Macro to Micro Cooling*; In ASME Paper GT2013-94277, 2013; pp. 1–17.

Bunker, R. S. *Latticework (Vortex) Cooling Effectiveness Part 1: Stationary Channel Experiments*; ASME Paper GT2004-54157; ASME, Vienna, Austria, 2004a; pp. 1–10.

Bunker, R. S.; Bailey, J. C.; Lee, C.; Stevens, C. W. *In-Wall Network (Mesh) Cooling Augmentation of Gas Turbine Airfoils*; ASME Paper GT2004-54260; Vienna, Austria, 2004b; pp. 1–12.

Busche, M. L.; Moualeu, L. P.; Tang, C.; Ames, F. E. Heat Transfer and Pressure Drop Measurements in High Solidity Pin Fin Cooling Arrays with Incremental Replenishment. *J. Turbomach.* **2013,** *135*, 041011-1-9.

Camci, C.; Arts, T. An Experimental Convective Heat Transfer Investigation around a Film-Cooled Gas Turbine Blade. *J. Turbomach.* **1990,** *112*, 497–503.

Carcasci, C.; Facchini, B.; Pievaroli, M.; Tarchi, L.; Ceccherini, A; Innocenti, L. Heat Transfer and Pressure Loss Measurements of Matrix Cooling Geometries for Gas Turbine Airfoils. *Journal of Turbomachinery* **2014,** *136*. https://doi.org/10.1115/1.4028237

Chupp, R. E.; Helms, H. E.; McFadden, P. W. Evaluation of Internal Heat-Transfer Coefficients for Impingement-Cooled Turbine Airfoils. *Journal of Aircraft* **1969,** *6*, 203–8.

Chyu, M. K.; Hsing, Y. C.; Shih, T I.-P.; Natarajan, V. Heat Transfer Contributions of Pins and Endwall in Pin-Fin Arrays: Effects of Thermal Boundary Condition Modeling. *Journal of Turbomachinery* **1999,** *121*, 257–63.

Cunha, F. J. Heat Transfer Analysis - Introduction. In *The Gas Turbine Handbook*, National Energy Technology Laboratory (NETL), Pittsburgh, PA, Morgantown, WV, 2006; pp. 389–411.

DOE. U.S. DOE Combined Heat and Power Installation Database. U.S. Department of Energy, 2020. https://doe.icfwebservices.com/chpdb/.

Downs, J. P.; Landis, K. K. *Turbine Cooling Systems Design: Past, Present and Future*; In ASME Paper GT2009-59991; 2009.

Du, W.; Luo, L.; Jiao, Y.; Wang, S.; Li, X.; Sunden, B. Heat Transfer in the Trailing Region of Gas Turbines – A State-of-the-Art Review. *Appl. Therm. Eng.* **2021,** *199*, 117614. https://doi.org/10.1016/j.applthermaleng.2021.117614.

Dyson, T. E.; McClintic, J. W.; Bogard, D. G.; Bradshaw, S. D. *Adiabatic and Overall Effectiveness for a Fully Cooled Turbine Vane*; ASME Paper GT2013-94928; 2013; pp. 1–12.

Florschuetz, L. W.; Metzger, D. E.; Truman, C. R. *Jet With Array Impingement Crossflow - Correlation of Streamwise Resolved Flow and Heat Transfer Distributions Jet Array Impingement With Crossflow - Correlation of Streamwise Resolved Flow and Heat Transfer Distributions*; Lewis Research Center, NASA, 1981a.

Florschuetz, L. W.; Truman, C. R.; Metzger, D. E. Streamwise Flow and Heat Transfer Distributions for Jet Array Impingement With Crossflow. *J. Heat Transf.* **1981b,** *103*, 337–342.

Gardner, W. B. *Energy Efficient Engine, High-Pressure Turbine Cooling Model Technology Report*; 1981.

GM. Allison Industrial Gas Turbines Operations, 501K/570K Brochure. General Motors Corporation, 1983. 501-brochure.pdf (intpower.com)

GTW. *2019 GTW Handbook;* Gas Turbine World. 2019; pp. 47–56.

Halila, E. E.; Lenahan, D. T.; Thomas, T. T. *Energy Efficient Engine: High Pressure Turbine Test Hardware Detailed Design Report*; NASA CR-167955; 1982.

Hampson, A.; Tidball, R.; Fucci, M.; Weston, R. *Combined Heat and Power (CHP) Technical Potential in the United States*; U.S. Department of Energy, 2016.

Han, J. C.; Dutta, S.; Ekkad, S. *Gas Turbine Heat Transfer and Cooling Technology*; 2nd ed.; CRC press, 2013. https://doi.org/https://doi.org/10.1201/b13616.

Han, J. C.; Ou, S.; Park, J. S.; Lei, C. K. Augmented Heat Transfer in Rectangular Channels of Narrow Aspect Ratios with Rib Turbulators. *International Journal of Heat and Mass Transfer* **1989,** *32*, 1619–30. https://doi.org/https://doi.org/10.1016/0017-9310(89)90044-6.

Han, J. C.; Park, J. S. Developing Heat Transfer in Rectangular Channels with Rib Turbulators. *International Journal of Heat and Mass Transfer* **1988,** *31*, 183–95. https://doi.org/https://doi.org/10.1016/0017-9310(88)90235-9.

Han, J. C.; Wright, L. M. Enhanced Internal Cooling of Turbine Blades and Vanes. In *The Gas Turbine Handbook,* 2007; pp. 321–52.

Holland, M. J.; Thake, T. F. Rotor Blade Cooling in High Pressure Turbines. *Journal of Aircraft* **1980,** *17*, 412–18. https://doi.org/10.2514/3.44668.

Hylton, L. D.; Mihelc, M. S.; Turner, E. R.; Nealy, D. A.; York, R. E. *Analytical and Experimental Evaluation of the Heat Transfer Distribution Over the Surfaces of Turbine Vanes*; 1983.

Hylton, L. D.; Nirmalan, V.; Sultanian, B. K.; Kaufman, R. M. *The Effects of Leading Edge and Downstream Turbine Vane Heat Transfer*; NASA CR-182133; 1988; pp. 1–172.

ICF International, Inc. *Combined Heat And Power: Policy Analysis And 2011 – 2030 Market Assessment*; California Energy Commission, 2012. https://www.cityofdavis.org/home/showdocument?id=4317 (accessed Aug. 2020).

Jaswal, I.; Ames, F. E. Heat Transfer and Pressure Drop Measurements in Constant and Converging Section Pin and Diamond Pedestal Arrays. *Journal of Thermal Science and Engineering Applications* **2009,** *1,* 11006-1-11006–7. https://doi.org/10.1115/1.3159498.

Kays, W. M. STAN7, A Finite Difference Boundary Layer Code. 1987.

Kilpatrick, E.; Kim, S. Roughness Effects on Flow and Heat Transfer in a Ribbed Duct Considering Additive Manufacturing. In Proceedings of GPPS Forum 18; 2018; pp. 10–12.

Körner, C.; Ramsperger, M.; Meid, C.; Bürger, D.; Wollgramm, P.; Bartsch, M.; Eggeler, G. Microstructure and Mechanical Properties of CMSX-4 Single Crystals Prepared by Additive Manufacturing. *Metall. Mater. Trans. A Phys. Metall. Mater. Sci.* **2018,** *49*, 3781–3792.

Laskowski, G. M., Tolpadi, A. K., and Ostrowski, M. C., 2007, "Heat Transfer Predictions of Film Cooled Stationary Turbine Airfoils," ASME Paper GT2007-27497.

Luan, Y.; Bu, S.; Sun, H.; Sun, T. Numerical Investigation on Flow and Heat Transfer in Matrix Cooling Channels for Turbine Blades. Proceedings of the ASME Turbo Expo, 2018; pp. 1–12.

Market Research Future. *U.S. Combined Heat and Power (CHP) Market Research Report - Forecast to 2025*; Market Research Future, 2019.

Martin, E. L.; Wright, L. M.; Crites, D.C. Impingement Heat Transfer Enhancement on a Cylindrical, Leading Edge Model With Varying Jet Temperatures. *Journal of Turbomachinery* **2013,** *135*, 31021. https://doi.org/10.1115/1.4007529.

Metzger, D. E.; Shepard, W. B.; Haley, S. W. *Row Resolved Heat Transfer Variations in Pin-Fin Arrays Including Effects of Non-Uniform Arrays and Flow Convergence*; In ASME Paper 86-GT-132, 1986. https://doi.org/10.1115/86-gt-132.

Nakamata, C.; Mimura, F.; Matsushita, M.; Yamane, T.; Fukuyama, Y.; Yoshida, T. *Local Cooling Effectiveness Distribution of an Integrated Impingement and Pin Fin Cooling Configuration*; In ASME Paper GT2007-27020, 4 PART A:23–34; 2007. https://doi.org/10.1115/GT2007-27020.

Prajapati, A. N.; Tariq, A. Detailed Heat Transfer Characteristics of Matrix Cooling Channels with Rib Angle 35° Using Liquid Crystal Thermography. ASME 2019 Gas Turbine India Conference, GTINDIA 2019, American Society of Mechanical Engineers (ASME), 2019.

Ramesh, S.; Robey, E.; Lawson, S. A.; Straub, D.; Black, J. Design Flow Field, and Heat Transfer Characterization of Conjugate Aero-Thermal Test Facility at NETL. Proceedings from the ASME Turbo Expo 2021; *Turbo Expo: Power for Land, Sea, and Air* **2021,** *10*; ASME Paper GT2020-15644. https://doi.org/10.1115/GT2020-15644.

Saha, K.; Acharya, S.; Nakamata, C. Heat Transfer Enhancement and Thermal Performance of Lattice Structures for Internal Cooling of Airfoil Trailing Edges. *J. Therm. Sci. Eng. Appl.* **2013,** *5*. https://doi.org/10.1115/1.4007277.

Schaffler, A. Experimental and Analytical Investigation of the Effects of Reynolds Number and Blade Surface Roughness on Multistage Axial Flow Compressors. *Journal of Engineering for Power* **1980,** *102*, 5–12.

Searle, M.; Roy, A.; Black, J.; Straub, D.; Ramesh, S. Investigating Gas Turbine Internal Cooling Using Supercritical CO_2 at High Reynolds Numbers for Direct Fired Cycle Applications. *Journal of Turbomachinery* **2021,** 1–15.

Selig, M. UIUC Airfoil Coordinates Database, 2021. https://m-selig.ae.illinois.edu/ads/coord_database.html.

Stimpson, C. K.; Snyder, J. C.; Thole, K. A.; Mongillo, D. Effectiveness Measurements of Additively Manufactured Film Cooling Holes. *J. Turbomach.* **2018,** *140*, 1–11.

Straub, D.; Ramesh, S.; Searle, M.; Roy, A.; Black, J. Baseline Airfoil Cooling Designs for A 5-10 MW Combined Heat And Power Turbine Application. Presented at the ASME Turbo Expo 2021; *Turbo Expo: Power for Land, Sea, and Air* **2021;** GT2021-59114.

Straub, D.; Sridharan, R.; Searle, M.; Robey, E.; Floyd, T.; Roy, A.; Ames, F. Performance of Additively Manufactured Internally Cooled Airfoils for Small Industrial Gas Turbines. Presented at the ASME Turbo Expo 2022; GT2022-83333.

Teraji, D. *TaurusTM 65 Gas Turbine Product*; ASME Paper GT2006-90099; 2006; pp. 597–601.

Theis, J.; Hoesly, R.; Myles, P.; Iyengar, A. *Combined Heat and Power Markets Study*; DOE/NETL-2020/2625; U.S. Department of Energy, National Energy Technology Laboratory, 2020.

Thulin, D.; Howe, D. C.; Singer, I. D. *Energy Efficient Engine High-Pressure Turbine Detailed Design Report*; NASA CR-165608; 1982.

Uysal, S.; Struab, D.; Black, J. Impact on Cycle Efficiency of Small Combined Heat and Power Plants From Increasing Firing Temperature Enabled by Additive Manufacturing of Turbine Blades and Vanes. Proceedings from the ASME Turbo Expo 2021; *Turbo Expo: Power for Land, Sea, and Air* **2021;** GT2021-58718.

Wright, L. M.; Han, J. C. Heat Transfer Enhancement for Turbine Blade Internal Cooling. *J. Enhanc. Heat Transf.* **2014,** *21*, 111–140.

Brian Anderson
Director
National Energy Technology Laboratory
U.S. Department of Energy

John Wimer
Acting Chief Research Officer
Science & Technology Strategic Plans
& Programs
National Energy Technology Laboratory
U.S. Department of Energy

Bryan Morreale
Associate Laboratory Director for
Research & Innovation
Research & Innovation Center
National Energy Technology Laboratory
U.S. Department of Energy